2019

Multiple Feedback Mechanisms Fine-Tune Rho Signaling To Regulate Morphogenetic Outcomes

Katy Lauren Ong
University of Pennsylvania, ongkaty1@gmail.com

Multiple Feedback Mechanisms Fine-Tune Rho Signaling To Regulate Morphogenetic Outcomes

Abstract
Rho signaling is a conserved mechanism for generating forces through activation of contractile actomyosin. How this pathway is tuned to produce different morphologies of cells and tissues is poorly understood. In the Drosophila embryonic epithelium, I investigated how Rho signaling controls force asymmetries to drive morphogenesis. Specifically, I studied a distinctive morphogenetic process termed "alignment". This process of coordinated cell shape changes results in a unique cell geometry of rectilinear cells connected by aligned cell-cell contacts. I found that this rearrangement is initialized by contractility of actomyosin cables that elevate the local tension along aligning interfaces. Curiously, I find that hours after establishing the alignment, this cell geometry is stabilized independent of actomyosin at the end of embryogenesis. This suggests that there are alternate mechanical bases for maintaining the aligned cell geometry in the steady state.

My data show that polarization of two branches of Rho signaling, Rho Kinase (ROK) and Diaphanous (Dia), is responsible for the formation of these cables. Constitutive activation of these Rho effectors causes aligning cells to instead invaginate. This observation suggests that moderation of Rho signaling is essential to producing the aligned geometry. Therefore, I tested for feedback interactions in the pathway that could fine-tune Rho signaling. I discovered that F-actin exerts negative feedback on multiple nodes in the pathway. In contrast, Myo-II does not feedback to the Rho pathway. However, inhibiting ROK caused an upregulation in Rho activity. This shows that ROK has a Myo-II independent function in regulating the Rho pathway. Taken together, this work suggests that multiple feedback mechanisms factor into the regulation of Rho signaling, which may account for the versatility of Rho in diverse morphogenetic processes.

Preliminarily, I also find a requirement for a regulator of Rac-Arp 2/3-mediated actin polymerization, pointing towards cooperation and crosstalk between branched actin and linear actin promoting pathways. This may allow for a balance of different mechanical forces that can generate the aligned geometry.

This thesis work lays down a foundation for understanding how the activity of contractile actomyosin and small GTPase signaling be modified to suit numerous morphogenetic processes.

Degree Type
Dissertation

Degree Name
Doctor of Philosophy (PhD)

Graduate Group
Cell & Molecular Biology

First Advisor
Stephen DiNardo

MULTIPLE FEEDBACK MECHANISMS FINE-TUNE RHO SIGNALING TO REGULATE MORPHOGENETIC OUTCOMES

Katy Lauren Ong

A DISSERTATION

in

Cell and Molecular Biology

Presented to the Faculties of the University of Pennsylvania

in

Partial Fulfillment of the Requirements for the

Degree of Doctor of Philosophy

2019

Supervisor of Dissertation

_____

Stephen DiNardo, Ph.D., Professor of Cell and Developmental Biology

Graduate Group Chairperson

_____

Daniel S. Kesler, Ph.D., Associate Professor of Cell and Developmental Biology

Dissertation Committee

Erika Holzbaur, Ph.D., William Maul Measey Professor in Physiology

Erfei Bi, Ph.D., Professor of Cell and Developmental Biology

Tatyana Svitkina, Ph.D., Professor of Biology

Michael Granato, Ph.D., Professor of Cell and Developmental Biology

MULTIPLE FEEDBACK MECHANISMS FINE-TUNE RHO SIGNALING TO REGULATE

MORPHOGENETIC OUTCOMES

Acknowledgements

I would first like to thank my advisor, Steve DiNardo. Steve is an excellent example of a kind, caring, and patient mentor. He is a brilliant and thoughtful scientist from whom I have learned a great deal. His dedication to academic rigor and freedom allowed this project to evolve and mature. I hope one day to emulate his ability to put together a nurturing and dynamic research group.

I would also like to thank the faculty members on my thesis committee: Erika Holzbaur, Michael Granato, Erfei Bi and Tatyana Svitkina. I feel extremely lucky to have had such a supportive committee. Every meeting with them was incredibly engaging and constructive. Our scientific conversations have been critical to my development as a young scientist.

I want to especially thank Bi and Tanya as co-mentors of one of my rotations. I am so grateful for the extra time they took to advise me through an extremely rewarding project on Septins. It was a pleasure to work with them on such a beautiful study.

I would also like to thank members of the DiNardo lab, past (Kynan Lawlor, Kari Lenhart, Dan Ly, Justin Siu, Lindsey Wingert, Qi Zheng, Laura Bowers) and present (Lauren Anllo, Laura Hyder, Sara Roberson) for creating an extremely positive and friendly lab environment.

In terms of support outside of the lab, if it were not for also my parents always believing in my goals and abilities, I would not be where I am today. Their support has been integral to the completion of my doctoral work. I would also like to thank my boyfriend, Gregg Inokuma, for always being in my corner through the entirety of my graduate studies.

Finally, I would like to thank my cats, Mimi and Copacabana, for jumping on my keyboard during the writing of this thesis and creating many typos.

ABSTRACT

MULTIPLE FEEDBACK MECHANISMS FINE-TUNE RHO SIGNALING TO REGULATE MORPHOGENETIC OUTCOMES

Katy Lauren Ong

Stephen DiNardo

Rho signaling is a conserved mechanism for generating forces through activation of contractile actomyosin. How this pathway is tuned to produce different morphologies of cells and tissues is poorly understood. In the *Drosophila* embryonic epithelium, I investigated how Rho signaling controls force asymmetries to drive morphogenesis. Specifically, I studied a distinctive morphogenetic process termed “alignment”. This process of coordinated cell shape changes results in a unique cell geometry of rectilinear cells connected by aligned cell-cell contacts. I found that this rearrangement is initialized by contractility of actomyosin cables that elevate the local tension along aligning interfaces. Curiously, I find that hours after establishing the alignment, this cell geometry is stabilized independent of actomyosin at the end of embryogenesis. This suggests that there are alternate mechanical bases for maintaining the aligned cell geometry in the steady state.

My data show that polarization of two branches of Rho signaling, Rho Kinase (ROK) and Diaphanous (Dia), is responsible for the formation of these cables. Constitutive activation of these Rho effectors causes aligning cells to instead invaginate. This observation suggests that moderation of Rho signaling is essential to producing the aligned geometry. Therefore, I tested for feedback interactions in the pathway that could fine-tune Rho signaling. I discovered that F-actin exerts negative feedback on multiple nodes in the pathway. In contrast, Myo-II does not feedback to the Rho pathway. However, inhibiting ROK caused an upregulation in Rho activity. This shows that ROK

has a Myo-II independent function in regulating the Rho pathway. Taken together, this work suggests that multiple feedback mechanisms factor into the regulation of Rho signaling, which may account for the versatility of Rho in diverse morphogenetic processes.

Preliminarily, I also find a requirement for a regulator of Rac-Arp 2/3-mediated actin polymerization, pointing towards cooperation and crosstalk between branched actin and linear actin promoting pathways. This may allow for a balance of different mechanical forces that can generate the aligned geometry.

This thesis work lays down a foundation for understanding how the activity of contractile actomyosin and small GTPase signaling be modified to suit numerous morphogenetic processes.

TABLE OF CONTENTS

ACKNOWLEDGMENT III

ABSTRACT IV

LIST OF FIGURES VIII

CHAPTER 1: GENERAL INTRODUCTION 1

Forces of morphogenesis 2

Actomyosin contractility in morphogenesis 3

Supracellular actomyosin cables 4

Polarity mechanisms in morphogenesis 6

Rho small GTPase signaling 7

Cell Alignment 8

The mechanical basis of alignment 9

Polarity signals that guide alignment 9

Diversification of actomyosin cable function 10

CHAPTER 2: MATERIALS AND METHODS 17

Fly Stocks and Husbandry 18

Immunofluorescence 18

Live Imaging 20

Laser Ablation 21

Drug Injections 21

DeGradFP-mediated Knockdown 22

Constitutive Activation of ROK and Dia 23

Quantification and Statistical Analysis 23

CHAPTER 3: THE MECHANICAL BASIS OF CELL ALIGNMENT 31

Introduction 32

Results 32

Discussion 37

CHAPTER 4: PLANAR POLARIZED RHO SIGNALING IS ESSENTIAL FOR ALIGNMENT 47

Introduction 48

Results 48

Discussion 52

CHAPTER 5: MULTIPLE FEEDBACK MECHANISMS FINE-TUNE RHO SIGNALING TO REGULATE MORPHOGENETIC OUTCOMES 65

Introduction 66

Results 67

Discussion 73

CHAPTER 6: A POTENTIAL ROLE FOR RAC-ARP2/3 SIGNALING IN ALIGNMENT 93

Introduction 95

Results 90

Discussion 98

CHAPTER 7: GENERAL DISCUSSION 107

Broader impacts for morphogenesis 108

Achieving further insight into the cell mechanics of alignment 109

Higher order polarity signals of alignment 112

The challenges of functional screens in the embryo 113

Amplification and robustness of signaling information 114

APPENDIX 117

BIBLIOGRAPHY 118

List of Figures

CHAPTER 1

Figure 1.1: Cell mechanics and morphogenesis

Figure 1.2: Diverse function of actomyosin supracellular cables

Figure 1.3: Cell Alignment in the *Drosophila* embryo

CHAPTER 2

Table 2.1: Fly Stock and Reagent Sources

CHAPTER 3

Figure 3.1: Alignment is driven by coordinated cell shape changes rather than junction remodeling.

Figure 3.2: Contractile force is upregulated along aligning junctions.

Figure 3.3: Actomyosin cables create force asymmetry to drive alignment

Figure 3.4: Alignment requires that contractile force be contributed from both sides of the interface

Figure 3.5: The aligned geometry is stabilized independent of actomyosin contractility later in development

CHAPTER 4

Figure 4.1: Rho signaling is planar polarized to aligning junctions

Figure 4.2: Rho and ROK are required for alignment

Figure 4.3: Diaphanous is the only formin required for alignment.

Figure 4.4: Rho effectors are required for actomyosin planar polarity.

Figure 4.5: Phosphorylation is not sufficient for Myosin activity or polarity.

Figure 4.6: Par3 is not required for alignment.

Figure 4.7: Model of Rho pathway function in alignment

CHAPTER 5

Figure 5.1: Overactivation of Rho signaling causes ectopic furrowing at aligning interfaces

Figure 5.2: Overactivation of Rho signaling changes the morphological outcome from alignment to apical constriction.

Figure 5.3: Ectopic furrow formation is associated with increased actin polymerization, not Myo-II recruitment.

Figure 5.4: F-actin negatively feeds back to Rho.

Figure 5.5: F-actin exerts additional feedback on the Dia branch of the Rho pathway.

Figure 5.6: F-actin and Myosin positively regulate one another within contractile cables.

Figure 5.7: Independent of actomyosin contractility, ROK regulates the Rho pathway.

Figure 5.8: Model of Rho pathway interactions that mediate polarization of actomyosin assembly and cortical tension during alignment.

CHAPTER 6

Figure 6.1: Dynamic protrusions indicate potential Arp2/3 activity in actomyosin cables

Figure 6.2: Arp2/3 associated factors are localized to aligning junctions

Figure 6.3: The Mbc/Elmo complex may function in alignment

Figure 6.4: Crosstalk between small GTPase pathways may allow for modification of morphogenesis

CHAPTER 1: General Introduction

Tissue function frequently relies on the underlying shapes and organization of its constituent cells. Diverse processes are responsible for coordinating the morphology and arrangement of cells into complex geometries. Failure of these morphogenetic processes can lead to developmental defects and cancer[1,2]. Therefore, investigation of the molecular basis of tissue morphogenesis is the key to significant insights into human health and disease.

Theoretically and *in silico*, simple epithelia can be physically conceptualized as two-dimensional, single-layered foams[3,4]. The contacts at which bubbles touch one another are always spaced 120º from one another (Fig. 1.1A). These contacts are equi-length across the foam and interconnect at three-way vertices, giving the whole arrangement the appearance of a honeycomb (Fig. 1.1A). This packing allows for the most even distribution of surface tension around the bubbles and is, thus, the lowest energy configuration[4]. Likewise, it is believed that the lowest energy state for a simple epithelium is a hexagonal arrangement of cell-cell contacts that are again separated by 120º (Fig. 1.1A).

This simple geometry of cells is not observed often in real tissues. This is because tissues commonly require more complex shapes and arrangements of cells in order to perform their physiological tasks. The formation and maintenance of complex geometries in the steady-state requires mechanical forces.

Two key pursuits in the field are understanding the molecular machinery that create these forces and the polarity mechanisms that wield them to drive diverse morphological changes.

Forces of Morphogenesis

The mechanical forces that generate high-energy geometries can come from many sources. They can be extrinsic in nature, meaning that they come from outside of

the cells that are undergoing morphogenesis. Examples include forces due to movements by adjacent tissues or remodeling of the extracellular matrix [5,6]. Forces can also be generated intrinsically, meaning that cells internally produce mechanical force in order to change their shape within the tissue[5,7,8]. This thesis work will focus on morphogenesis driven by intrinsic forces.

Additionally, there are different types of mechanical force that cells can apply at cell-cell contacts during tissue morphogenesis[9,10]. Contractile force can be applied along the axis of the contact inwards toward the middle, promoting compression and shortening of the contact (Fig. 1.1C). Compression forces orthogonal to cell contacts generally strengthen adhesions and promote contact elongation (Fig. 1.1C). Finally, shear stresses are applied along opposing vectors parallel with the junction (Fig. 1.1C). Shear stresses are difficult to measure *in vivo* and even harder to attribute a morphogenetic function to, but they can be produced intracellular by the cytoskeleton and are hypothesized to weaken cell-cell contacts[11]. Additionally, they may deform the contact in other ways. Different combinations of deploying these three types of mechanical force allow for a variety of cell geometries to persist in steady state.

Actomyosin contractility in morphogenesis

Intrinsically-produced forces rely on intracellular molecular machines. One broadly conserved machine is the actin and myosin cytoskeleton[12]. This machinery is commonly referred to as “actomyosin” because of the two core components: filamentous actin (F-actin) and non-muscle myosin II motors (Myo-II). Activated Myo-II complexes co-assemble into bi-polar “mini-filaments” that can bind and walk along F-actin. The binding of multiple motor heads in the mini-filaments to multiple actin filaments coupled to the movement of those motors mediates the contraction of the entire filamentous

network[7,12]. With proper physical coupling, this network can apply contractile force to membranes in order to drive cell shape changes.

This strategy is used to induce various morphological changes in cells: apical constriction, cell intercalation, cell migration, and many others[5,12]. There are some factors that are known to dictate the activity of actomyosin networks. Examples include the organization of filaments within these network, the actin-binding proteins that associate with and crosslink filaments in the network, the linkers between actomyosin and the membrane, and the dynamics of actin polymerization and depolymerization[5,12–14]. Despite the large body of work that describes these examples, we still do not have a complete picture of how cells are able to diversify the functionality of actomyosin networks to achieve different shapes and geometries.

Supracellular Actomyosin Cables

Another important factor that determines the function of actomyosin is the manner by which it is spatially distributed within cells and across tissues. Subcellular structures that control the morphogenesis of individual cells are much better understood than the assemblies that cooperate during multicellular morphogenetic programs. Understanding the actomyosin structures that produce forces and participate in tissue morphogenesis are therefore a very active field of research.

One such organization of actomyosin is the so-called actomyosin supracellular cable[15]. These structures are actually multiple assemblies of F-actin and Myo-II located at contiguous cell junctions across multiple cells. While technically a collection of subcellular structures, each contractile subunit is interconnected with the whole via physical linkage at cell-cell adhesions. This allows for cooperation between the contractile subunits and for the so-called cables to function as a cohesive structure. Mechanically, these cables increase the local cortical tension along the junctions that

they occupy [16–20]. This creates force asymmetry in the tissue in order to drive morphology changes (Fig. 1.2A-F). Functionally, they are utilized in many processes in both vertebrates and invertebrates and can produce different morphological changes in tissues[15]. During wound healing, a cable forms at the edge of the wound margin to promote its closure (Fig. 1.2A) [21–24]. In the development of tube structures such as that in the kidney, cables form at junctions perpendicular to the tube axis to induce junction shrinking (Fig. 1.2B) [25]. This decreases the diameter of the tube (Fig. 1.2C) [25]. Additionally, actomyosin cables mediate closure of the neural tube in mammals[26,27]. By purportedly contracting along the interior of the nascent tube, these cables promote curving of the tissue and eventual sealing of the tube (Fig. 1.2C) [26,27].

In *Drosophila*, the study of two more examples of actomyosin cable activity has revealed a great deal of molecular insight into their mechanism of action: rosette formation during convergent extension and mechanical boundary formation in larval tissues[28,29].

During convergent extension in the early *Drosophila* embryo, select junctions along the dorsal-ventral axis upregulate actin and myosin, forming actomyosin cables[28,30]. These cables increase the cortical tension along those junctions, creating force asymmetry within the tissue (Fig. 1.2D,G) [18,19]. This induces the junctions to shrink (Fig. 1.2D). The morphological consequences are a cluster of cells joining together transiently at a point, resembling a rosette [19,28](Fig. 1.2D). This allows for the compaction of the tissue along the dorsal-ventral axis. Subsequently, new junctions form in the middle of the rosette along the anterior-posterior axis, causing the tissue to elongate in this new direction[28,31].

Actomyosin cables also participate in the mechanical segregation of cells at tissue boundaries[16,17,29,32,33]. These tissue boundaries separate compartments of

cells with different gene expression profiles. The underlying mechanism is not fully understood, but the activity of the actomyosin cables prevent cells from crossing over the boundary, thereby maintaining the cellular identity of the adjacent compartments [16,17,29,32]. As with convergent extension, cables elevate the cortical tension along the junctions of cells making up the boundary. Indeed, laser ablation measurements show that the degree of force asymmetry at mechanical boundaries is comparable to that along junctions that shrink during convergent extension[16–19,32]. However, the morphological results from this force asymmetry at tissue boundaries are quite different from that observed during convergent extension. Instead, the junctions along the boundary shorten somewhat but never shrink completely (Fig. 1.2E, G vs H) [16,17]. The junctions also align slightly to give the boundary a smooth morphology (Fig. 1.2E, H) [16,17].

Both convergent extension and mechanical boundary formation appear to rely on similar actomyosin supracellular structures that impart a comparable contractile force asymmetry within the tissue. There is an open question as to what molecularly and mechanically distinguishes these two morphogenetic events. This question gets at a larger gap of knowledge in the field; we know little about how actomyosin structures are regulated to serve different functions.

Polarity mechanisms in morphogenesis

In order to complete their jobs, the subunits of actomyosin cables need to be properly positioned in the cell and oriented within the tissue. This requires polarity molecules that can spatially instruct the recruitment of actomyosin assembly.

There are a variety of polarity factors that control each spatial dimension of the cell. There are factors that stratify the apical-basal axis of the cell (Fig. 1.1B). This is critical to properly positioning cell junctions, the membrane anchor points for the

cytoskeleton. Adherens junctions, positioned just below the apical surface, are composed of E-cadherin complexes that mechanically link the membrane to the actin cytoskeleton. Other cell-cell junction types can also be relevant to epithelial morphogenesis. In my study, I primarily focus on cell shape changes that occur at the level of adherens junctions, as this is where actomyosin is most active in my system. Therefore, I use the terms “cell-cell contact” or “contact” interchangeably with “junction”.

Planar polarity factors function in the plane orthogonal to the apical basal axis (Fig. 1.1B). These signals position structures, such as actomyosin cables, with respect to neighboring cells[34].

The full array of polarity factors the participate in morphogenesis has yet to be identified. Furthermore, of those that are known, it is still poorly understood how they orchestrate downstream events to drive complex morphological changes.

Rho small GTPase signaling

The Rho family of small GTPases are master polarity regulators of the actin cytoskeleton[35–37]. The members of this family are associated with different cellular functions of actin[37]. Generally speaking, Rho (the namesake member of the family) is linked with promoting contractile actomyosin assembly[35,37]. There are multiple Rho homologs in the human genome, but Rho1 is the sole homolog in *Drosophila* and hereafter will be referred to simply as Rho[38]. While Rho targets many downstream effectors, this thesis will focus on two key players in promoting contractile actomyosin assemblies: Rho Kinase (ROK) and Diaphanous (Dia).

ROK has a number of phosphorylation targets, the most well-known of which is the regulatory Myosin Light Chain (MLC)[39]. This phosphorylation event is essential to alleviating MLC from its autoinhibited state [40]. After this step, Myo-II hexamers can assemble into active mini-filaments. Dia is the sole Diaphanous family formin in

Drosophila[41]. It promotes actin filament nucleation and elongation, most notably within linear arrangements of actin [41].

The function and regulation of the Rho pathway within classic subcellular contractile structures like stress fibers has been intensely studied[35]. Rho function is required for the morphogenesis of many tissues, but its mechanism of action is much less well understood in these various contexts [42–44].

Out of many types of structures, Rho can promote the assembly of actomyosin supracellular cables[15]. Active GTP-bound Rho and its effectors enrich along junctions targeted for shrinking during convergent extension (Fig. 1.2D,G) [42,45,46]. There is also significant evidence that planar polarization of Rho signaling also guides the assembly of actomyosin cables at mechanical tissue boundaries (Fig. 1.2E,H) [33,47,48].

Yet again, it is unclear how or if Rho function is altered to regulate these two very different morphogenetic events.

Cell Alignment

During my doctoral research, I studied a distinctive morphological process that in many ways resembles both convergent extension and mechanical boundary formation, but yields a unique tissue geometry. Specifically, I researched a developmental event in the *Drosophila* embryonic epithelium that our lab has termed “alignment”[49]. This process occurs in the anterior region of each abdominal segment during mid-embryogenesis. In terms of embryonic developmental stages, this spans the end of Stage 12 and the beginning of Stage 13[49,50]. In each segment, alignment occurs at two interfaces of cell-cell contacts along the dorsal-ventral axis (Fig. 1.3A magenta)[49,51].

Before alignment, the cells exhibit irregular packing where the angles separating cell-cell contacts average close to 120º. This is characteristic of a simple epithelium in a low-energy state[52,53]. Over time, the two interfaces straighten significantly relative to non-aligning regions of the epithelium (Fig. 1.3B, magenta vs orange). Quantitatively, this means that angles between contacts approach 180º, which is a high-energy configuration. By comparison, cells in the adjacent regions maintain an angle distribution that is closer in average to 120º (Fig. 1.3B orange).

Several hours after alignment has completed, the cells adjacent to and in between the two interfaces give rise to protrusions called denticles (Fig. 1.3C). The denticles are neatly arranged in straight rows along the dorsal-ventral axis. These denticles allow for proper traction while larvae crawl[54]. This is in part a function of the aligned cellular geometry. Hence, the collective cell changes that occur earlier in development are significant to the physiological function of this epithelium.

The mechanical basis of alignment

As in convergent extension and mechanical boundaries, actomyosin cables are also involved in alignment[49,50]. Cables are localized along the aligning junctions, spanning the length of the interfaces (Fig. 1.2F, I) [49]. Embryos depleted of Myo-II activity exhibit alignment defects[49], suggesting a requirement for actomyosin contractility and possibly asymmetric force production. As described in Chapter 3, I would go on to test this hypothesis extensively during my thesis work and show that it is indeed the case that cortical tension is selectively upregulated along aligning junctions.

Polarity signals that guide alignment

The polarity mechanisms that regulate actomyosin assembly during alignment were also unknown prior to the beginning of my doctoral candidacy. Given the likely

function for contractile actomyosin in alignment, Rho signaling was an obvious candidate. Upon investigating the function of Rho during alignment, I would find that there is a requirement for planar polarization of Rho and its effectors to aligning junctions. This strongly resembles what is known about convergent extension and mechanical boundary formation. These findings are documented in Chapter 4.

Diversification of actomyosin cable function

The first half of my thesis work revealed these essential insights into alignment. However, I was left with no answer to the more important question: what allows for differentiation of morphological outcomes of Rho signaling and actomyosin contractility? The resultant cell geometry from alignment is unique compared to the rosettes formed during convergent extension and the smooth interfaces that arise at mechanical boundaries (Fig. 1.2G-I). Rather than shrinking or shortening as observed in these other examples, the junctions within aligning interfaces actually elongate against the direction of contractile force (Fig. 1.2F, I). This is counter-intuitive. In fact, in most simulations of force balance at junctions, contractile force is the primary factor in driving junction shrinkage, while adhesive force is modeled to promote junction lengthening (Fig. 1.1C) [5,53,55].

In terms of cytoskeletal organization, tensile force distribution and polarity signaling, there is little that differentiates alignment from convergent extension or mechanical boundary formation.

The question of what accounts for the unique cell geometry observed in alignment can be broken down into two parts. First, what in terms of signaling is different about alignment relative to convergent extension and mechanical boundary formation? Is Rho signaling molecularly repurposed in some manner to produce these different cell arrangements? In an attempt to answer this question, I overactivated the

Rho pathway and observed an interesting effect on alignment. The activity of the actomyosin cables was modified by this manipulation, causing an aberrant change in tissue morphology. Essentially, changing the activity levels of Rho and its effectors switched the morphological outcome, specifically from alignment to furrowing. As detailed in Chapter 5, this led to the pursuit of mechanisms that could fine-tune Rho activity, leading to the identification of multiple feedback interactions within the pathway.

Second, what is different about actomyosin activity during alignment versus other morphogenetic processes? What permits cell junctions to lengthen along the same axis that contractile force is upregulated? I hypothesize that actin remodeling factors modify the structure of cables in order to promote this unique cell morphological change. In Chapter 6, I begin to characterize the structure and dynamics of actin within supracellular cables at higher temporal and spatial resolution than has been previously done. Additionally, I screened numerous actin-associated proteins, looking for factors that are present or enriched at aligning interfaces. My observations cumulatively suggest that Arp2/3 activity is present in actomyosin cables. In contrast to Dia, Arp2/3 promotes actin nucleation along the length of existing actin filaments in order to create branch points[56,57]. Branched actin networks can produce pushing forces at membranes that may allow for resistance to contractile forces[14,58–60]. Arp2/3-activity is typically controlled by relatives of Rho, Rac or Cdc42[35,37]. Preliminarily, I find a requirement for a Rac activator for alignment, further supporting the hypothesis that Arp2/3-mediated actin polymerization may mechanically contribute to the activity of actomyosin cables. Additionally, these initial observations may point to a role for Rac-Arp2/3 signaling that can crosstalk with the Rho pathway in order to balance linear and branched actin remodeling.

As I have described previously, actomyosin cables have extremely diverse functions and are a broadly conserved mechanism for inducing morphology changes

(Fig. 1.2A-F)[15]. Between processes and even within different phases of a single morphogenetic event, there is likely a need for changes in activity and the mechanical properties of cables. My work lays a foundation for further explore the molecular mechanisms that allow for such fine-tuning, which will be broadly applicable to many morphogenetic events and tissue types.

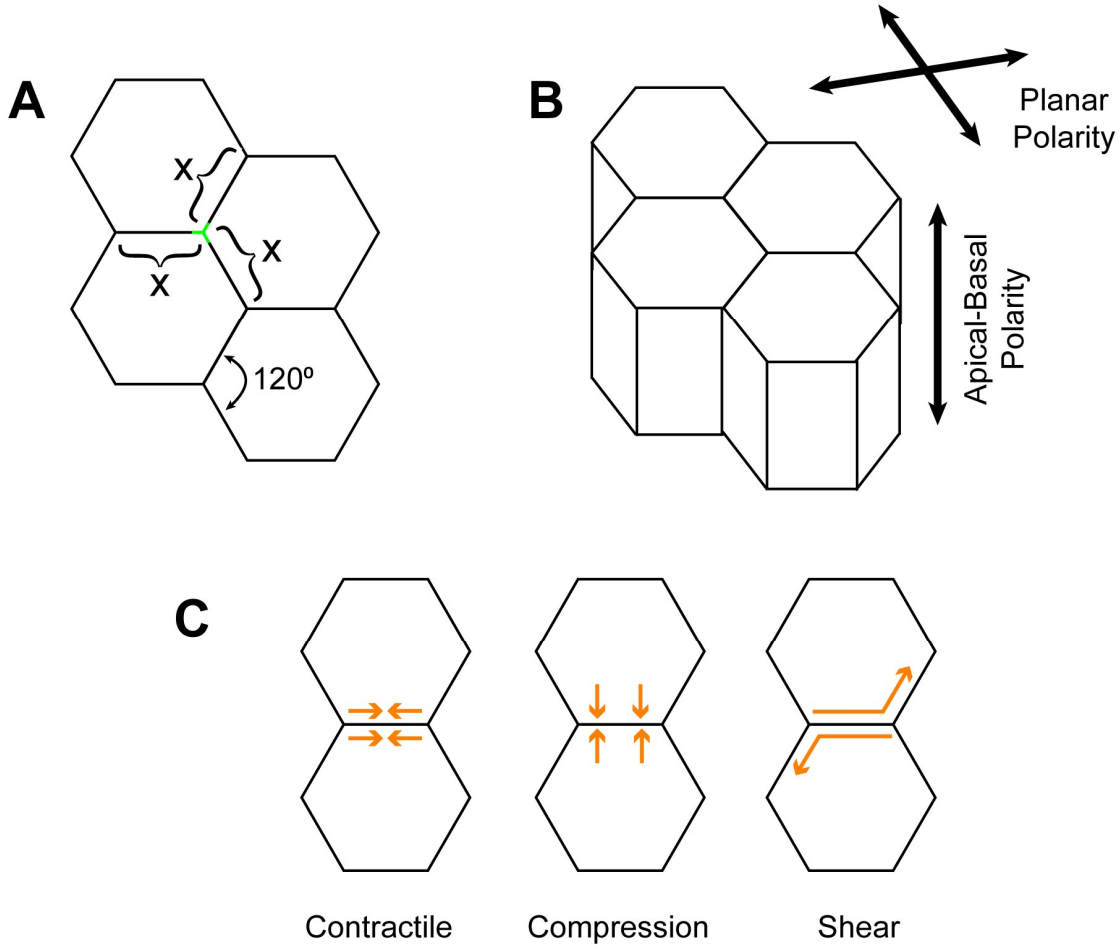

Figure 1.1: Cell mechanics and morphogenesis

(A) Schematic of the apical surface of a simple epithelium in its theoretical low-energy state. Cell-cell contacts are equilength (represented by value "X") and separated by 120º angles. These contacts meet at 3-way vertices (green), giving the epithelium a hexagonal packing.

(B) The axes along which molecules can be polarized and morphogenesis can occur in a theoretical epithelium.

(C) Types of intracellular forces (orange arrows). Contractile forces promote compression oriented along cell-cell contacts. Compression forces push on cell-cell contacts to promote adhesion and junction lengthening. Shear forces may weaken adhesion or deform cell contacts.

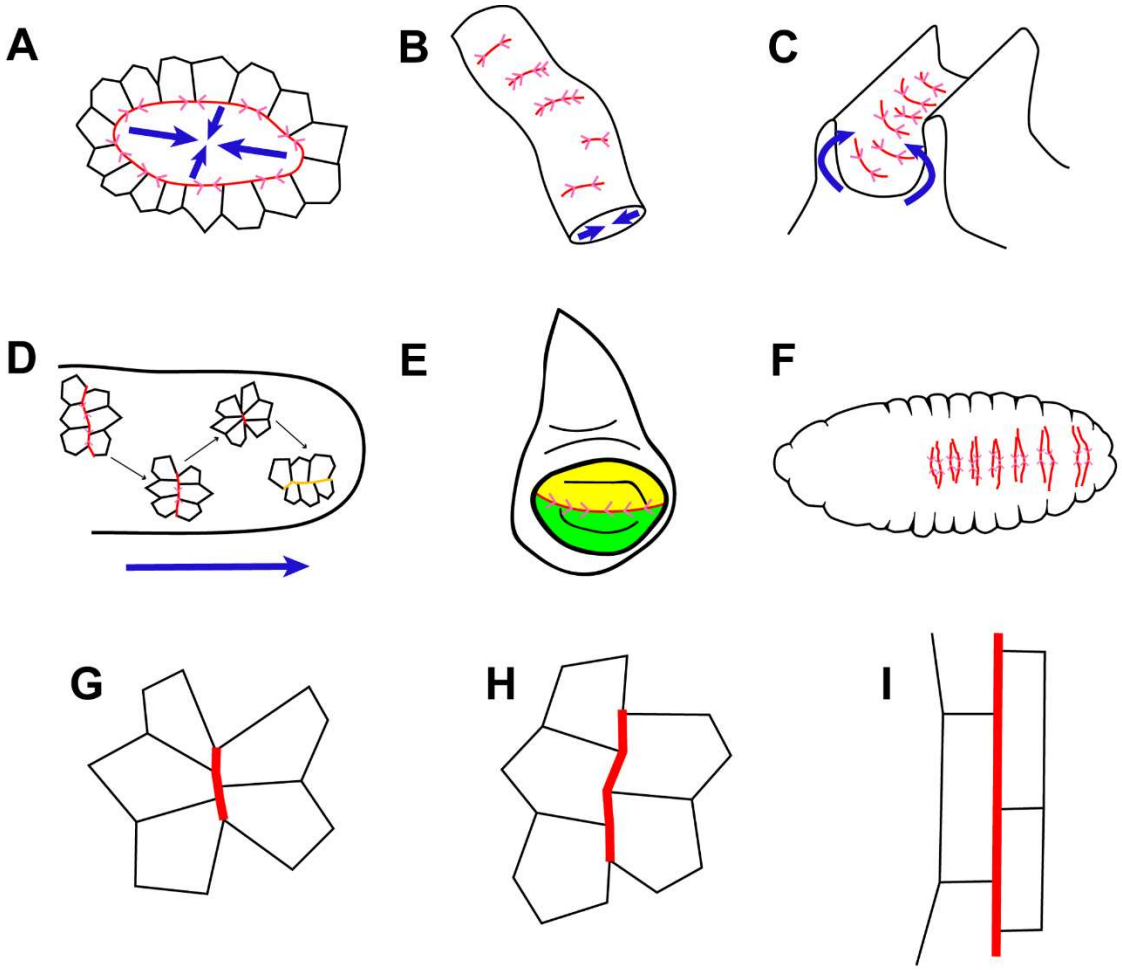

Figure 1.2: Diverse function of actomyosin supracellular cables

(A-F) Examples of actomyosin cable function in morphogenesis. (A) Actomyosin cables at wound margins encourage the closure of wounds. (B) Cables can decrease the diameter of tubulated epithelia through contraction. (C) Contraction of cables in the interior of the nascent neural tube allows it to curve and seal. (D-F) Specific examples of actomyosin cable function in *Drosophila* tissues. (D) During convergent extension in the early *Drosophila* embryo, cables are biased along the dorsal-ventral axis to shrink cell junctions, transiently forming rosettes and compacting the tissue. New junctions grow in the middle of these rosettes in the opposite direction, allowing for elongation of the tissue. (E) Cables at gene expression boundaries in developing *Drosophila* tissues prevent the intermixing of cells at the boundary, allowing for maintenance of separate compartments with different cellular identities. (F) Actomyosin cables align interfaces that correspond with the denticle fields in mid-embryogenesis. Red lines show the location of actomyosin cables. Pink arrows show the direction of contractile force from those cables. Blue shows the larger morphogenetic movements of the tissue due to the actomyosin cable activity.

(Figure 1.2 Continued)

(G-I) High resolution schematics of how actomyosin cables and Rho signaling polarity can produce diverse cell geometries. Schematics show the distribution of actomyosin and Rho activity (both represented by red) during (G) convergent extension (H) mechanical boundary formation and (I) alignment.

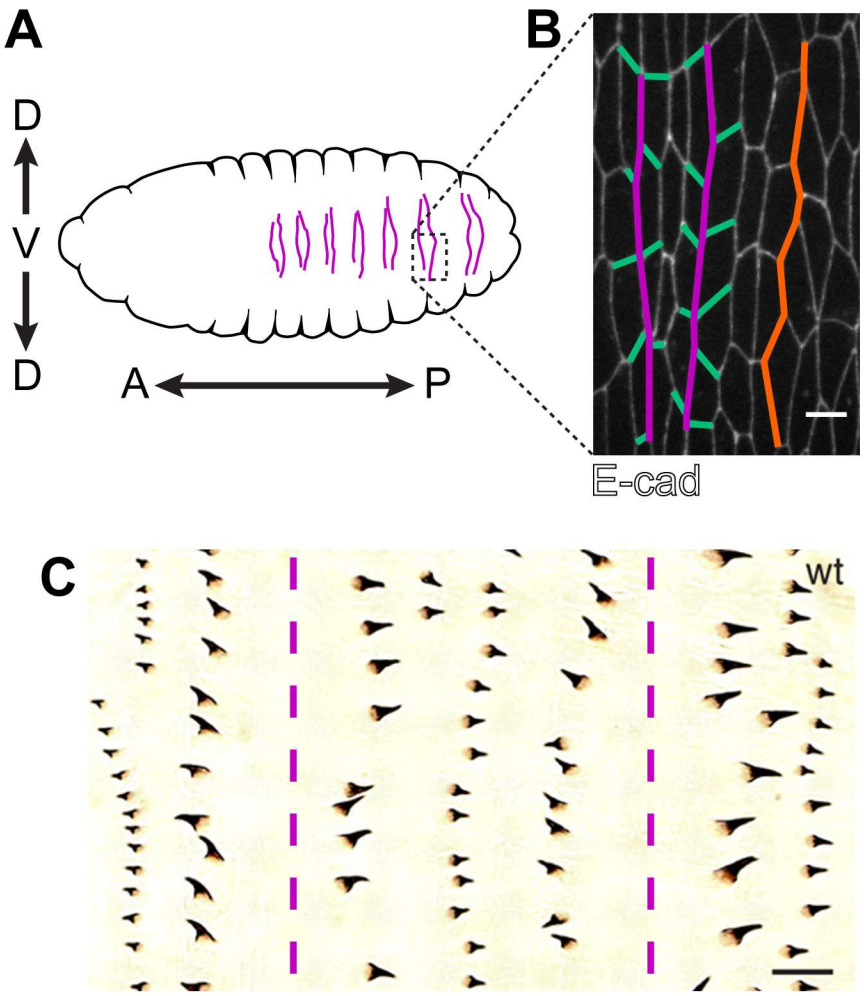

Figure 1.3: Cell Alignment in the *Drosophila* embryo

(A) A schematic of the ventral face after alignment. Arrows indicate anterior-posterior and dorsal-ventral axes. In each abdominal segment, the two aligning interfaces are indicated in purple.

(B) The junctions within aligning interfaces (purple) straight out along the dorsal-ventral axis. This is specific to these two interfaces within each abdominal segment and is not observed in the non-aligning (orange) regions. Intersecting orthogonal junctions (green) sometimes form four-way vertices. Cell junctions marked with E-cad::GFP.

(C) Actin-based structures called “denticles” form aligned rows along aligning interfaces. Brightfield image of denticles in one abdominal segment of a late stage embryo, after alignment has completed. Reproduced from *Donoughe and DiNardo 2011*. Dashed magenta lines show position of aligned interfaces.

Scale bar = 4μm in (B). Scale bar = 10μm in (C).

CHAPTER 2: Materials and Methods

Fly Stocks and Husbandry

Flies were raised on standard cornmeal medium at 25°C. For knockdown of Pav with RNAi, the cross was kept at 28°C to boost GAL4-mediated expression of the short hairpin RNA. Embryos were collected on apple juice agar plates supplemented with a dab of fresh yeast paste. After allowing adult flies to lay fertilized eggs for approximately 12 hours, the embryos were transferred to a nylon mesh strainer by rinsing with de-ionized water and using a paintbrush. Embryos were de-chorionated with 50% bleach for no longer than 5 minutes, and then processed as described in subsections below.

Immunofluorescence

For Dia staining, embryos were processed with a heat fixing protocol[61]. This begins with immersion of dechorionated embryos 3mL of boiling E-Wash buffer (0.3% Triton-X, 0.4% NaCl) in a glass vial. The vial is then quickly filled with ice cold E-wash buffer (approximately 17mL), capped and submerged in ice. The embryos are washed once with Phosphate Buffered Saline (PBS, 7mM Na-HPO_4, 3mM Na-HPO_4, 150mM NaCl) before being devitellinized with a 2:1 methanol:heptane mixture with vigorous shaking for 30 seconds. Devitellinized embryos were washed three times with 100% methanol and stored at 4ºC for at least two days prior to beginning the immunofluorescent staining.

For phalloidin staining, embryos were fixed in a glass vial at 23ºC in a 1:1 mixture of 40% para-formaldehyde (PFA):heptane for 12 minutes while on a rocker[62]. The PFA was removed and replaced with PBS solution. Embryos were transferred onto double sided tape adhered to a glass dish and covered with a small volume of PBS. Embryos were manually removed from the vitelline membrane using a tungsten needle. Embryos were transferred to PBS-TX solution before proceeding immediately with immunofluorescent staining.

For all other stains, embryos were fixed in a glass vial at 23ºC in a 1:1 mixture of 4% PFA in PBS:heptane for 20min while on a rocker [63]. The PFA was removed and replaced with an equal volume of 90% Methanol, 50mM EGTA. The vial was vigorously shaken for 30 seconds to devitellinize the embryos. The heptane was removed and devitellinized embryos were washed with 100% methanol three times. Embryos were transferred to 100% ethanol for storage or to PBS-TX for immediate immunofluorescent staining.

For the remainder of the immunofluorescent staining protocol, all incubations occurred on a rocker. Embryos were incubated in PBS-TX (0.1% Triton-X in PBS) for 10min at 23ºC. Embryos were incubated in block solution (1% NDS, 1% NGS, 0.1% Triton-X in PBS) for 1hr at 23ºC. Embryos were incubated in primary antibody diluted in block overnight at 4ºC. Antibodies were used at the following concentrations: pTyr (1:1000), Dia (1:500), GFP (Chicken 1:2000 and/or Rabbit 1:1000), RFP (1:500). Embryos were washed three times with PBS-TX with the last wash lasting at least 1hr at 23ºC. They were then incubated in an approximate mix of secondary antibodies conjugated to 488 or 647 Alexafluors or Cy3. All secondary antibodies were diluted in block solution at a concentration of approximately 2µg/mL. After a 1hr incubation at 23ºC, embryos were washed as described above with PBS-TX.

For F-actin imaging, embryos were incubated in approximately 0.05µM Rhodamine-Phalloidin or 0.1µM 647 Alexafluor-Phalloidin diluted in PBS-TX for 20min at 23ºC. Embryos were then washed with PBS-TX as previously described.

For Hoechst staining, embryos were incubated in about 1µg/mL dilution in PBS-TX for five minutes at 23ºC. This was followed by four washes of PBS-TX without rocking.

Embryos were transferred to a 2% n-propyl gallate:80% glycerol solution prior to being mounted on glass slides, covered with 23X30 glass coverslips and sealed with clear nail polish.

Fixed and stained embryos were imaged on one of two systems. First, an Axioplan Zeiss widefield microscope equipped with either a 40X 0.75 N.A. water immersion objective or a 20X 0.75 N.A. dry objective using AxioVision software. For imaging with the 40X objective, a structured illumination system (Zeiss Apotome) was used in order to remove out of focus information. The second system used was an IX7 Olympus spinning disk confocal microscope equipped with an 100X oil immersion 1.4 N.A. objective. Images were acquired with a Hamamatsu Photonics electron multiplying charge-coupled device camera (EMCCD, model C9100-13) controlled using Metamorph software. Z-stacks were acquired with a 0.5μm step size.

Live Imaging

Embryos were sorted and oriented on an agar plate using a tungsten needle. A weak adhesive was made from dissolving double-sided tape in heptane ("heptane-glue"). Embryos were transferred to a strip of dried heptane-glue on a glass slide such that the dorsal side made contact with the glue. Embryos were covered with approximately 3uL of 27 weight Halocarbon oil. Two 18x18 coverslips were glued on either side of the embryos to create spacers. A 23x30mm coverslip was glued to the spacers to cover the embryos[43].

Time lapse imaging was performed on either a Leica DM16000 B spinning disk confocal with a 63X 1.2 N.A water immersion objective or an IX7 Olmpus spinning disk confocal microscope with a 60X 1.2 N.A. water immersion objective. Images were acquired with an EMCCD camera (Andor iXon 3 897E or Hamamatsu photonics, model

C9100-13) controlled by Metamorph software. Z-stacks were acquired with a 0.5μm step size and a time interval of either 2.5, 5 or 10min.

Laser Ablation

Embryos were mounted as described above. Fluorescently-labelled E-cadherin was used to visualize cell junctions. Either MLC::mCherry or Engrailed-GAL4 > NLS::mCherry was used as a marker to identify the position of aligning interfaces. Embryos were imaged using the IX7 Olympus spinning disk with a 100X 1.4 N.A. objective (see above). A Micropoint nitrogen-pumped laser with a 405nm dye cell was used for laser ablation. The ablation laser was controlled using Andor IQ3 software that interfaced with Metamorph. A single timepoint, two-color z-stack image was taken initially to allow for unambiguous, post-acquisition identification of the ablated junction. Then, a single z-plane, single color time lapse was initiated to image E-cadherin with an interval of 0.25 seconds for a total of 75 seconds. Within the first 10 seconds of the time lapse, a single point ROI was placed on the target junction and a single pulse of the laser was fired. The remaining approximately 60 seconds of the time lapse captured the subsequent retraction of the adjacent membranes around the ablation site.

Drug Injections

For drug injection experiments, embryos were mounted as described for Live Imaging but with their ventral side adhered to a heptane glue strip on a 23X30 coverslip. Embryos were covered with 700 weight Halocarbon oil. The coverslip was glued to a transparent plastic frame that fit into our microscope specimen holder. Imaging pre- and post-injection was performed on the Leica DM16000 B spinning disk system with a 63X 1.2 N.A. objective (see above). A micromanipulator was mounted onto the sample holder stage using an optical post apparatus (Thor labs). A single timepoint, z-stack

image with a step size of 0.5µm was taken of each embryo prior to injection. Femtotip needles (Eppendorf Cat no. 930000043) were backfilled with drug or control vehicle solution using capillary loading tips before being installed onto the micromanipulator. A time lapse, z-stack series was immediately acquired after injections were complete (between 5 and 15 minutes from the start of injecting the first embryo).

Drugs were diluted as follows: Cyto D -- 5mM in 1:1 DMSO:MilliQ-filtered water; Lat B 5ug/uL -- in 100% DMSO, SMIFH2 -- 20ug/uL in 100% DMSO, Y-27632 -- 10-20mM in MilliQ-filtered water, H-1152 – 10mM in MilliQ-filtered water. Alignment and fluorescent protein localization was analyzed prior to injection and at the following time points after the beginning of injection: Cyto D -- 10minutes; Lat B -- 10-20min, SMIFH2 – 90min; Y-27632/H-1152 – 10min. As a negative control, embryos of the same genotype were injected with solvent to rule out any defects caused by injection or exposure to the vehicle.

Cyto D binds to the barbed ends of actin filaments to block the addition of monomers[64,65]. It can also induce actin dimers, which causes ATP hydrolysis, depleting the pool of actin monomers competent for incorporation into filaments. Effectively, this has been reported to induce actin depolymerization in some physiological contexts[66] while only blocking polymerization in others[67].

Lat B binds to actin monomers, sequestering them from filaments to block polymerization and promote depolymerization[68].

DeGradFP-mediated Knockdown

We used the UAS-driven DeGradFP construct [69]. The construct contains a GFP-recognizing nanobody fused to an F-box domain. This allows for recruitment of GFP-labelled substrates to the E2 ligase complex for eventual ubiquitin-mediated degradation. Males expressing both Engrailed-GAL4 and UAS-DeGradFP were crossed

to females that had a null MLC allele, sqh^{AX3}, on their X chromosome and a transgene expressing GFP-labelled MLC. Embryos that inherited a Y chromosome from the male only expressed MLC::GFP and were therefore functionally MLC-depleted in the GAL4 expressing regions. Embryos that inherited the X chromosome from the male were used as controls as they received a wild-type, untagged allele of MLC that rescued cells from DeGradFP knockdown. In both deGradFP knockdown and control embryos, the anterior aligning interface was analyzed in each abdominal segment.

Constitutive Activation of ROK and Dia

The UAS-ROK-CA expresses ROK that is missing the C-terminus responsible for auto-inhibition[70]. The UAS-Dia-CA expresses Dia that has truncations at both the N and C-termini, leading to deletion of the GTP-ase interacting and autoinhibitory domains, respectively[71].

Quantification and Statistical Analysis

The degree of alignment was determined by measuring the angles between adjacent cell contacts using the angle tool in ImageJ. The angles of a single interface were averaged and normalized to a range of 120 to 180 to give a percent alignment. Angles of 180º are by definition 100% aligned and 120º is defined as 0% aligned.

Fluorescence measurements along cell junctions were manually measured using the segmented line tool in Fiji with the width set to 3 pixels. To test for differences in fluorescence intensity between aligning and orthogonal junctions (e.g. Fig. 3.1), measurements were taken of each aligning and orthogonal junction in a given interface. An ROI covering a small area off of the embryo sample was measured for background fluorescence. This average background fluorescence was subtracted from all junctional measurements to correct for background. The corrected mean gray values (MGV) were

averaged for both types of junction. The two averages were treated as a paired sample for each interface and were compared using a Wilcoxon Rank test to determine statistical significance (e.g. Fig. 3.1A-C). For comparing the fluorescence intensity between aligning and orthogonal junctions, the average mean gray value was compared between that of aligning junctions and orthogonal junctions within the same interface. A Wilcoxon Rank test was used to determine whether there was a significance difference in fluorescence levels between aligning and orthogonal junctions, with the measurements for each interface being treated as a paired sample.

For comparing the average fluorescence between embryos processed with immunofluorescent staining, we accounted for variability in staining by normalizing the mean gray value at the experimentally perturbed interface to that of the unaffected interface (in other words, the signal at control or MLC depleted interfaces was normalized to the regions indicated in with white arrowheads, as in Fig. 5.5C and Fig. 5.6C). For all other experiments, the mean gray value was used to compare fluorescence intensity at aligning interfaces between different embryos.

To measure planar polarity, the mean gray values of aligning junctions and orthogonal junctions were averaged, respectively. The ratio between these averages was then used to represent planar polarity. A value greater than 1 indicates relative enrichment along aligning junctions with respect to orthogonal junctions.

Measurements of fluorescence intensity, planar polarity and alignment were compared between sample groups of different genotypes or before and after drug treatment using non-parametric statistical tests. In most cases, an unpaired Mann-Whitney test was performed. In cases of drug treatment where the same cells could be precisely tracked and analyzed before and after drug exposure, a paired, Wilcoxon Rank test was performed (as in Fig. 5.4E, F).

For analysis of cell morphology during furrow ingression, each cell flanking the interface was manually traced using the polygon tool in Fiji to create an ROI. Apical surface area (μm^2), major axis length and minor axis length were extracted from the ROI. Cell anisotropy was calculated as a ratio between the major and minor axes. Furrow depth was determined by counting the number of Z-slices between the top and bottom of the furrow at each time point. The average apical surface area, average cell anisotropy, and furrow depth were plotted for each time point. These parameters were compared between a Dia-CA expressing segment and an adjacent, non-expressing control segment for the same embryo over the same time points. The anterior-most interface was analyzed in each case, as Eve-GAL4 is expressed more strongly in the cells along the anterior interface compared to the posterior interface.

Maximum velocity as inferred from laser ablation experiments was used as a metric of cortical tension. The length of the ablated junction was manually measured by drawing a line with the line tool in Fiji. This measurement was taken prior to ablation and every 5 seconds after ablation up to a total of 60 seconds. Maximum velocity was calculated from these measurements.

For comparing cell junction remodeling events to the degree of alignment, embryos expressing E-cad::GFP and MLC::mCherry were live-imaged as described above at a time interval of 2.5 minutes. The duration of the live imaging included before, during and after completion of alignment. Interfaces were manually tracked using Fiji software. Alignment and the number of 3-way and 4-way vertices were measured for each time point. A 4-way vertex is formed when a junction between two three-way vertices is remodeled away (Fig. 3.1). Therefore, the number of cell junction shrinking events was represented by the fraction of 4-way vertices present in the interface. For each time point and each of three interfaces analyzed, the percent alignment was plotted against the percent 4-way vertices. A Pearson correlation test was used to assess the

relationship between these two metrics, and a linear regression was fitted to the data (Figure S1C).

Errors bars for all graphs represent Standard Deviation. All statistical tests and curve fitting were executed with Graphpad Prism software.

Table 2.1: Fly Stock and Reagent Sources

RESOURCE OR REAGENT	SOURCE	LOCATION	IDENTIFIER
Antibodies			
Mouse anti-phospho-Tyrosine (pTyr)	Millipore	Burlington, MA, USA	4G10 - Cat#05-321
Rabbit anti-Dia	Steven Wasserman	San Diego, CA, USA	[72]
Rabbit anti-RFP	Abcam	Cambridge, United Kingdom	Cat# 62341
Chicken anti-GFP	Aves Labs	Tigard, OR, USA	GFP-2010
Mouse anti-Scar	Developmental Studies Hybridoma Bank	Iowa City, IA, USA	P1C1
Rabbit anti-GFP	Invitrogen	Carlsbad, CA, USA	A-11122
Alexafluor Secondary Antibodies (488, 647)	Molecular Probes	Carlsbad, CA, USA	N/A
Cy3 Affinipure Secondary Antibodies	Jackson Immunoresearch Laboratories	West Grove, PA, USA	N/A
Chemicals			
Para-formaldehyde (PFA) 16%	Electron Microscopy Sciences	Hatfield, PA, USA	15710
PFA 40%	Electron Microscopy Sciences	Hatfield, PA, USA	15715-S
Rhodamine-conjugated Phalloidin	Invitrogen	Carlsbad, CA, USA	R415
Alexafluor 647-conjugated Phalloidin	Invitrogen	Carlsbad, CA, USA	A-22287
27 Weight halocarbon oil	Halocarbon Products Corp	River Edge, NJ, USA	9002-23-9
700 Weight halocarbon oil	Sigma Aldrich	St. Louis, MO, USA	H8898-100mL
Y-27632 dihydrochloride (ROK inhibitor)	Sigma Aldrich	St. Louis, MO, USA	Y0503
Latrunclin B	EMD Millipore	Burlington, MA, USA	428020-1MG
Cytochalasin D	Santa Cruz	Santa Cruz, CA, USA	201442
SMIFH2 Formin inhibitor	Sigma Aldrich	St. Louis, MO, USA	S4826-5MG
Propyl-gallate	Sigma Aldrich	St. Louis, MO, USA	P3130
Normal Donkey Serum (NDS)	Jackson Immunoresearch Laboratories	West Grove, PA, USA	017-000-121
Normal Goat Serum (NGS)	Jackson Immunoresearch Laboratories	West Grove, PA, USA	005-000-121
Hoescht	Sigma Aldrich	St. Louis, MO, USA	14530
Experimental Models			
w^{1118}	Bloomington Drosophila Stock Center (BDSC)	Marseille, France;	BL#3605

		Bloomington, IN, USA	
Ubi::Ani-RBD-GFP; sqh-Moe-ABD::mCherry	Made with Ubi-Ani-RBD::GFP (gift from Thomas Lecuit) and sqh-Moe-ABD::mCherry (BDSC)	Marseille, France; Bloomington, IN, USA	[45] and BL#35521
Ubi::Ani-RBD-GFP; Ubi-Par3::mCherry	Made from Ubi-Ani-RBD-GFP (gift from Thomas Lecuit) and Ubi-Par3::mCherry (gift from Yohannes Bellaiche)	Marseille, France; Paris, France	[45,73]
sqh^{AX3}; sqh-sqh::GFP	Gift from Roger Karess	Paris, France	[74]
sqh^{AX3}; E-cad::tdTomato; sqh-sqh::GFP	Made with sqhAx3;sqh-sqh::GFP (gift from Roger Karess) and E-cad::tdtTom (gift from Yang Hong)	Paris, France; Pittsburgh, PA, USA	[74,75]
UAS-Dia::GFP	BDSC	Bloomington, IN, USA	BL#56751
UAS-dia^{FH3FH1FH2}::EGFP/CyO	BDSC	Bloomington, IN, USA	BL#56753
Frl$^{MI03375\text{-}GFSTF.0}$/TM3, Sb^{1} Ser^{1}	BDSC	Bloomington, IN, USA	BL#60195
Capu$^{MI05737\text{-}GFSTF.0}$/CyO	BDSC	Bloomington, IN, USA	BL#66507
DAAM$^{MI04569\text{-}GFSTF.0}$ lncRNA:CR46248$^{MI04569\text{-}GFSTF.0\text{-}X}$/FM7j, B^{1}	BDSC	Bloomington, IN, USA	BL#60213
dia^{2}/CyO-Dfd-GMR-nvYFP	*dia*^{2} Gift from Steve Wasserman and BDSC	San Diego, CA, USA and Bloomington, IN, USA	[76] and BL#23230
rho1^{72O}/CyO-Dfd-GMR-nvYFP	BDSC	Bloomington, IN, USA	BL#7325 and BL#23230
rho1^{72F}/CyO-Dfd-GMR-nvYFP	BDSC	Bloomington, IN, USA	BL#7326 and BL#23230
UAS-Pav shRNA	BDSC	Bloomington, IN, USA	BL#42573
E-cad::tdTomato	Gift from Yang Hong	Pittsburgh, PA, USA	[75]
E-cad::tdTomato; Tubulin-GAL4	Made from E-cad::tdTomato (gift from Yang Hong) and Tubulin-Gal4 (BDSC)	Pittsburgh, PA; Bloomington, IN, USA	[75] BL#5138
Engrailed-GAL4, UAS-mCherry::NLS; UAS-DeGradFP/TM3,Sb	BDSC	Bloomington, IN, USA	BL#38420
sqh^{AX3}; sqh-Utr-ABD::GFP, sqh-sqh::mCherry	Gift from Adam Martin	Cambridge, MA, USA	[43]
sqh-GFP::ROK^{K116A}, Ubi-Par3::mCherry	Made from sqh-GFP::ROK^{K116A} (gift from Jennifer Zallen) and Ubi-Par3::mCherry (gift from Yohannes Bellaiche)	New York, NY, USA; Paris, France	[46,73]

E-cad::tdTomato; sqh-GFP::ROK^{K116A}	Made from E-cad::tdTomato (gift from Yang Hong) and sqh-GFP::ROK^{K116A} (gift from Jennifer Zallen)	Pittsburgh, PA; New York, NY, USA	[46,75]
Ubi-E-cad::GFP, sqh-sqh::mCherry/CyO-Dfd-GMR-nvYFP	Made from Ubi-E-cad::GFP (gift from Jennifer Zallen), sqh-sqh::mCherry (gift from Adam Martin) and sna^{sco}/CyO-Dfd-GMR-nvYFP (BDSC)	New York, NY; Cambridge, MA; Bloomington	[77,78] BL#23230
Eve-GAL4	BDSC	Bloomington, IN, USA	BL#40732
Opa-GAL4	BDSC	Bloomington, IN, USA	BL#47406
E-cad::tdTomato; Eve-GAL4	Made from E-cad::tdTomato (gift from Yang Hong) and Eve-GAL4 (BDSC)	Pittsburgh, PA, USA and Bloomington, IN, USA	[75] and BL#40732
UAS-mCherry::NLS	Gift from Amin Ghabrial	New York, NY, USA	N/A
sqh-sqh^{WT}::GFP	Gift from Jennifer Zallen	New York, NY, USA	[79]
sqh-sqh^{EE}::GFP	Gift from Jennifer Zallen	New York, NY, USA	[79]
UAS-rok^{CA}::HA	Gift from Jennifer Zallen	New York, NY, USA	[46]
E-cad::tdTomato; tGPH	Made from E-cad::tdTomato (gift from Yang Hong) and tGPH (BDSC)	Pittsburgh, PA, USA	[75] and BL#8164
Ubi-CPB::mCherry	BDSC	Bloomington, IN, USA	BL#58726
mbc^{C1}/CyO-Dfd-GMR-nvYFP	BDSC	Bloomington, IN, USA	BL#23230 and BL#1671
Ubi-Abi::mCherry/TM6b, Tb	BDSC	Bloomington, IN, USA	BL#58729
WASp::GFP	BDSC	Bloomington, IN, USA	BL#60289
Fimbrin::GFP	BDSC	Bloomington, IN, USA	BL#51562
RhoGAP19D::GFP	BDSC	Bloomington, IN, USA	BL#78134
Coffilin::GFP	Kyoto Stock Center	Kyoto, Japan	#115280
Elmo::GFP	Kyoto Stock Center	Kyoto, Japan	#115020
Software			
FIJI	www.fiji.sc	N/A	N/A
ImageJ	www.imagej.nih.gov/ij/	Bethesda, MD, USA	N/A
Metamorph Microscopy Automation and Image Analysis Software	Molecular Devices	San Jose, CA, USA	N/A
Axio-Vision Imaging Software	Zeiss	Oberkochen, Germany	Version 4.8

Graphpad Prism	Graphpad Software	San Diego, CA, USA	Version 7.00
Andor IQ3 Live Cell Imaging Software	Andor	Belfast, United Kingdom	N/A

CHAPTER 3: The Mechanical Basis of Cell Alignment

Introduction

Our lab previously reported the requirement for non-muscle Myosin II (Myo-II) in alignment[49]. Furthermore, our lab showed that enrichments of non-muscle Myo-II and F-actin arise along interfaces, forming supracellular actomyosin cables[15,49]. This evidence strongly indicates a role for asymmetric force generation. Using laser ablation approaches and localized depletion of Myosin activity, I determined that alignment arises from elevated cortical tension along aligning junctions. These forces derive from actomyosin contractility from both cell columns making up the aligning interface. Interestingly, loss of force from just one side of the interface is sufficient to disrupt the aligned morphology, indicating a requirement for symmetric force application for proper orientation of these junctions. Finally, I have preliminary evidence that over a longer time scale, force asymmetry dissipates from the interfaces and that the aligned morphology is stabilized independent of actomyosin contractility. This suggests that other mechanisms can maintain non-energetically favorable cell geometries, and that further inquiry into this system may reveal novel insights into cell mechanics.

Results

Junction remodeling does not mechanistically explain the aligned geometry

Our lab previously proposed that alignment was caused by shrinkage of select cell-cell contacts along the interfaces (Fig. 3.1A)[49]. However, analyzing the cell dynamics of this process at higher temporal resolution revealed no correlation between the remodeling events and the emergence of alignment (Fig. 3.1C). Therefore, I considered alternatively whether alignment may be caused by collective cell shape changes driven by actomyosin contractility along the length of the interface (Fig. 3.1C).

Local actomyosin contractility generates force asymmetry to drive alignment

To test this, I used laser ablation to map the forces in the aligning epithelium. I ablated individual junctions within the aligning interface (Fig. 3.2A, magenta) and "orthogonal" junctions intersecting the aligning interfaces (Fig. 3.2B, green). As a control, I ablated junctions within non-aligning interfaces (Fig. 3.2C, orange). Tension along aligning interfaces was over three-fold higher compared with that of orthogonal junctions (Fig. 3.2A vs B, D), revealing a large local force asymmetry. Furthermore, relative to non-aligning junctions, tension was about two-fold higher along aligning junctions (Fig. 3.2A vs C, D) demonstrating that this is asymmetry is not a global property of the epithelium.

To determine whether this tension asymmetry is actomyosin-dependent, I used deGradFP to deplete MLC[69] and disrupt contractility in aligning cells. In brief, this approach utilizes a construct (hereafter "deGradFP") that targets GFP-tagged proteins for degradation (see Materials and Methods). The presence of deGradFP in an MLC mutant embryo (sqh^{AX3}) that only expresses a transgenic GFP-tagged MLC would result in knockdown of Myo-II activity. I used a spatially-restricted Engrailed-GAL4 line to express UAS-deGradFP. This resulted in knockdown of MLC in the cells at only the anterior aligning interface, resulting in alignment defects (Fig. 3.3A, B, red arrowheads and dashed line) and binucleated cells, indicating disrupted cytokinesis (Fig. 3.3A blue arrowheads). This was in contrast to sibling controls that expressed wild-type, untagged MLC from a Sqh+ allele and were, therefore, insusceptible to deGradFP (Fig. 3.3B, yellow "WT CTRL"). To rule out the possibility that cytokinesis defects caused the alignment phenotype, I analyzed embryos expressing interfering RNAs (RNAi) to Pavarotti (Pav), a kinesin-like protein involved in cytokinetic ring assembly[80]. Pav knockdown caused binucleated cells but no disruption to alignment (Fig. 3.3C, D).

I then used deGradFP knockdown to test whether force asymmetry is generated by the actomyosin cables. When I measured the tension along aligning junctions of the MLC-depleted interface, I found that tension was significantly decreased in comparison to the same interface in control embryos (Fig. 3.3E). This resulted in a 30% reduction in tension asymmetry between aligning and orthogonal junctions (Fig. 3.3E). These results demonstrate that cells at the aligning interface generate cortical tension by upregulating actomyosin contractility. Furthermore, I can conclude that these local forces are responsible for alignment, rather than extrinsic forces from tissues distal to the aligning epithelium.

Contractile force is required from cells on both sides of the aligning interface

I gained further insight into the mechanics of alignment by capitalizing on variability in the Engrailed-GAL4 expression pattern. This line primarily expresses in the first column of cells comprising the anterior aligning interface (Fig. 3.4A, B). However, there was occasional GAL4 expression in cells on the posterior side of the interface (Fig. 3.4B). This yielded two scenarios: unilateral knockdown in which depletion only occurred on one side of the interface (Fig. 3.4B, salmon) and "bilateral" knockdown in which cells on both sides of the interface were depleted for MLC (Fig. 3.4B, red). Unilateral knockdown caused a decrease in tension along aligning junctions relative to that of wild-type sibling controls (Fig. 3.4B, gray). With bilateral knockdown, tension was reduced even further compared to unilateral knockdown (Fig. 3.4B). This demonstrates that cortical tension along the aligning interfaces comes from actomyosin in the cells on each side of the interface. Interestingly, alignment was equally defective with either unilateral or bilateral knockdown of MLC (Fig. 3.4C), suggesting that tensile forces must be applied from both sides of the interface for alignment to occur.

The aligned geometry is maintained independent of contractile force asymmetry over the long term

The aligned geometry and actomyosin cables are fully established at the beginning of embryonic Stage 13 (Fig. 3.5A). At least four hours after this, the aligned geometry is maintained. This time frame encompasses a number of significant developmental events in the epithelium. First, at the beginning of Stage 14, dorsal closure begins. As the epithelium migrates to enclose the opening on the dorsal side of the embryo, the ventral epithelial cells are stretched out along the dorsal-ventral axis (Fig. 3.5B). The DiNardo lab showed previously that alignment occurs independently of this stretching process, as dorsal closure mutants still have properly aligned interfaces[49].

Also during Stage 14, as dorsal-closure proceeds, actomyosin begins to accumulate on the apical surface of the ventral denticle cells (Fig. 3.5B). This apico-medial actin pool forms a dynamic, irregular meshwork. During Stage 15, when dorsal closure is mostly complete, this meshwork will aggregate over time into foci that are the precursors to denticles (Fig 3.5C, 1.3C).

In addition to the cellular geometry, it seems that actomyosin polarity persists through all of these stages of embryonic development. At Stage 14, the presence of actomyosin cables is apparent (Fig. 3.5B, right panel). At Stage 15, this is more difficult to discern because of the presence of actin-based protrusions on the apical surface (Fig. 3.5C, third panel). However, when I examined a z-slice 0.5μm below the apical surface, subtle MLC enrichments were seen at the two interfaces (Fig. 3.5C, right panel). I have not quantified this as the actin-based protrusion pool may confound measurements. However, the evidence suggests that actomyosin cables are present for these stages and that they may allow for maintenance of alignment for many hours (Fig. 3.5A-C).

To test this hypothesis, I measured the local force distribution at the aligned interfaces at Stages 14 and 15. I then compared these quantifications to the force asymmetry I measured at Stage 13, when alignment is first initialized.

I was surprised to find that the force asymmetry that I characterized at the aligned interfaces dissipates with time (Fig. 3.5D). Recall that just after alignment, there was an over three-fold elevation in cortical tension between aligning and orthogonal junctions (Fig. 3.5D, Stage 13). In the middle of actin-based protrusion formation, this difference had declined to an over two-fold difference (Fig. 3.5D, Stage 14). By the time actin-based protrusions had fully matured, there was no significance difference in force between aligning and orthogonal junctions (Fig. 3.5D, Stage 15). The size of these two sample groups are relatively small, and the analysis would benefit from repetition of the experiment. However, it is very clear that cortical force asymmetry is not maintained over this time scale, despite the presence of actomyosin enrichments and the persistence of the aligned geometry.

I also tested whether the cortical tension at junctions in older embryos comes from actomyosin contractility. As described previously, at alignment initialization, the tension along aligning junctions is decreased substantially with deGradFP-mediated knockdown of MLC (Fig 3.5E, Stage 13). At Stage 14, the decline in force observed with MLC knockdown is significant, but smaller in magnitude. This is consistent with the previous observation that the actomyosin-derived forces that produce tension asymmetry are beginning to wane at this developmental time point. By Stage 15, there was no significant difference in retraction velocity between control and MLC-depleted aligning junctions. This indicates that whatever cortical tension is remaining at this point is not Myo-II derived, and that the actomyosin-generated force asymmetry has completely disappeared by Stage 15.

Discussion

Actomyosin-generated, bilateral cortical tension is required for alignment

I have shown that alignment constitutes a tissue-scale, coordinated cell shape change driven by local increases in contractile force. Depletion of actomyosin-based forces lowered the tension along aligning junctions, consequentially reducing the force asymmetry relative to orthogonal junctions (Fig. 3.3E). It is worth noting that there was still a significant force asymmetry with Myosin depletion (Fig. 3.3E). One explanation for this decreased tension is that polarized Rho activity along aligning interfaces sequesters Myo-II away from orthogonal junctions. However, it is also possible that other mechanisms actively decrease tension along orthogonal junctions. There has been some suggestion that E-cad enriches along orthogonal junctions and depletes from aligning junctions[49]. This increase in E-cad could indicate an increase in adhesive forces that could counter contractile force. However, qualitatively, I have observed that this re-distribution of E-cad does not begin until at least an hour after alignment has been established. Therefore, I find this hypothesis unlikely.

Two cells contribute actomyosin to each of the junctions in the aligning interface. Therefore, it was not surprising to observe an additional decrease in tension from bilateral vs unilateral knockdown of MLC (Fig. 3.4B). Intriguingly, unilateral depletion of MLC was sufficient to disrupt the aligned morphology (Fig. 3.4C). This implies that the minimum force required for alignment necessitates the contribution of both cells (bilateral contractility). Alternatively, there may be a need for symmetric contractility – unilateral application of force could be as counter-productive to alignment as full depletion of Myo-II activity.

With laser ablation, the read out of cortical tension is the outward retraction rate of junctions. This indicates that contractile force is applied along the junctions starting from the adjacent vertices inwards toward the middle of the junction. However, there

could be other directions of force application that this assay does not directly reveal. With unilateral knockdown, there may be a disruption of the balance of such force vectors that could contribute to loss of the aligned geometry.

The aligned geometry is stabilized by actomyosin-independent mechanisms later in development

The aligned geometry is maintained for a remarkably long period of developmental time – upwards of four hours after actomyosin cables first form, which constitutes about 20% of embryonic development. Even more fascinating is that my preliminary data suggests that the manner by which this geometry is stabilized evolves over developmental time.

It appears that actomyosin cables are present through this entire timeframe, although given the potentially confounding apical signal from denticle formation, a careful quantitative analysis at each developmental stage would be necessary to solidify this conclusion. Regardless, it is clear that the contractile force generated by these cables decreases over time. Irrespective of this, the interfaces remain aligned.

There are a number of interesting cellular and molecular events that temporally correlate with the dissipation of force asymmetry. First, as mentioned previously, the cells stretch along the dorsal ventral axis during the course of dorsal closure. Again, this is partially due to the migration of the dorsal epithelium in order to enclose the amnioserosa. However, our lab showed qualitatively that cells are still anisotropically stretched even when dorsal closure is blocked[49]. This suggests that there are other, potentially intracellular mechanisms for the stretching of these cells. Tissues that are artificially stressed will initially upregulate actomyosin along the axis of stretch, resulting in upregulation of cortical tension in that direction[81]. However, if the stretch is applied for a long enough duration, the forces created by this actomyosin polarity will

dissipate[81]. This is purportedly due to unknown mechanisms that buffer the tissue against mechanical stresses. After at least 2 hours of increasing cellular stretch, such a buffering mechanism could be deployed in the late embryonic epithelium.

Secondly, septate junctions emerge and mature after Stage 13. This is characterized by the emergence of classic septate junction marker Discs large (Dlg) and the tricellular septate junction Gliotactin during Stage 14[49,82,83]. It has recently been proposed that septate junctions can increase the stiffness or viscosity of a tissue, thereby countering contractile forces[84]. Indeed, our lab previously reported that Dlg mutants have alignment defects[49]. However, it was originally hypothesized that Dlg regulated junction remodeling in alignment. This cannot be the case for two reasons: (1) is clear that Dlg is not present at cell junctions until significantly later in development and (2) as I demonstrated above, junction remodeling is not the cell mechanical basis of alignment. It would be interesting to further investigate whether septate junction or Dlg contribute to the mechanics of the tissue during these later stages of development.

A vast majority of developmental mechanics research is focused on actomyosin-derived forces. Exploration of the physical basis of this geometry stabilization will likely reveal novel mechanisms of tissue morphogenesis.

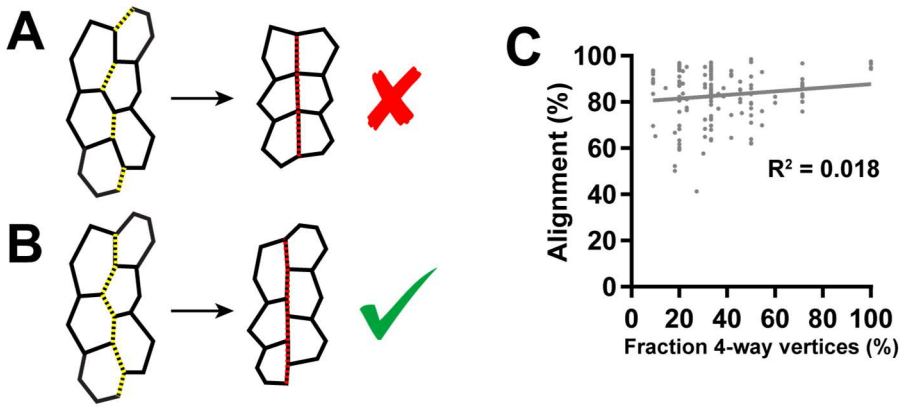

Figure 3.1: Alignment is driven by coordinated cell shape changes rather than junction remodeling.

(A and B) Two models can explain the alignment morphology. (A) The first involves elevated contractility along select junctions in the interface driving remodeling events to create 4-way vertices. (B) The second model has cortical tension elevated along all contacts of the interface to drive coordinated cell shape changes. Yellow dashed lines indicate location of elevated tension.

(C) A lack of correlation between the presence of 4-way vertices and the alignment of the interface eliminated (A) the first model. The R^2 value from a Pearson correlation test is shown as well as a linear regression fit. N = 3 interfaces, 3 embryos

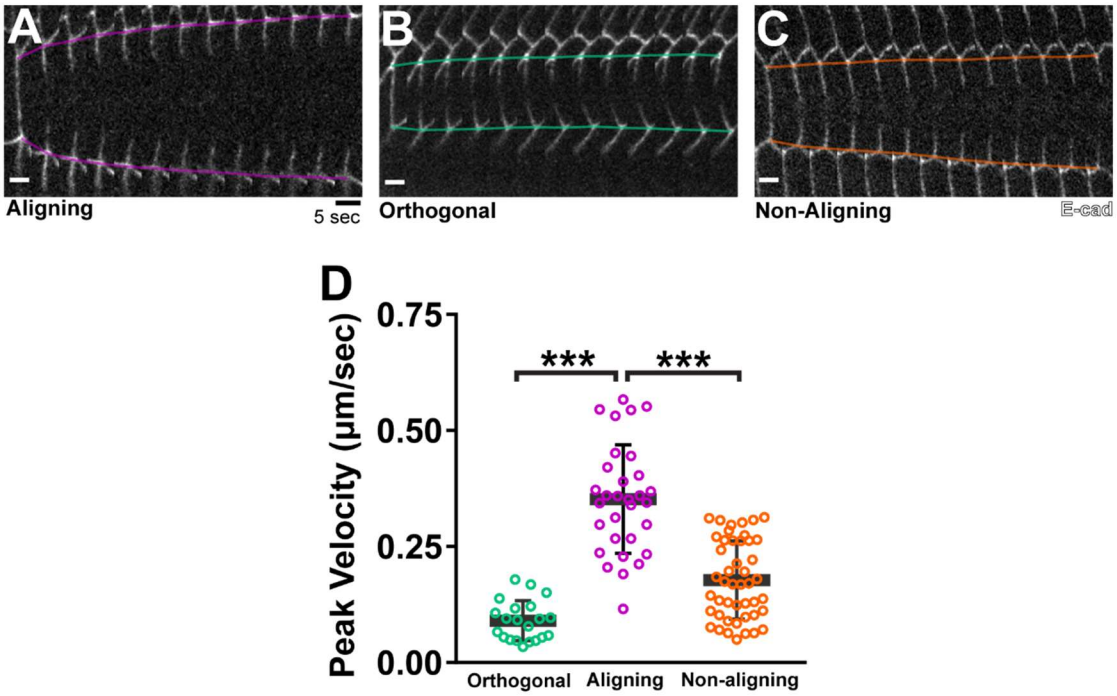

Figure 3.2: Contractile force is upregulated along aligning junctions.

(A-C) Representative montages of retraction in response to laser ablation for (A) aligning, (B) orthogonal and (C) non-aligning junctions. The first image in each sequence shows the junction prior to ablation and each subsequent frame represents a five second interval. Pseudo-colored lines map out the trajectory of motion for the vertices that connect the cut junction.

(D) Tension was elevated along aligning (purple) cell-cell contacts relative to orthogonal (green) and non-aligning (orange) contacts. Cell junctions were visualized with E-cad::GFP. Orthogonal: 21 junctions from 15 embryos; Aligning: 31 junctions, 21 embryos; Non-aligning: 46 junctions, 26 embryos

***p<0.0001, Mann-Whitney U test, Error bars = S.D. Scale bars = 4µm.

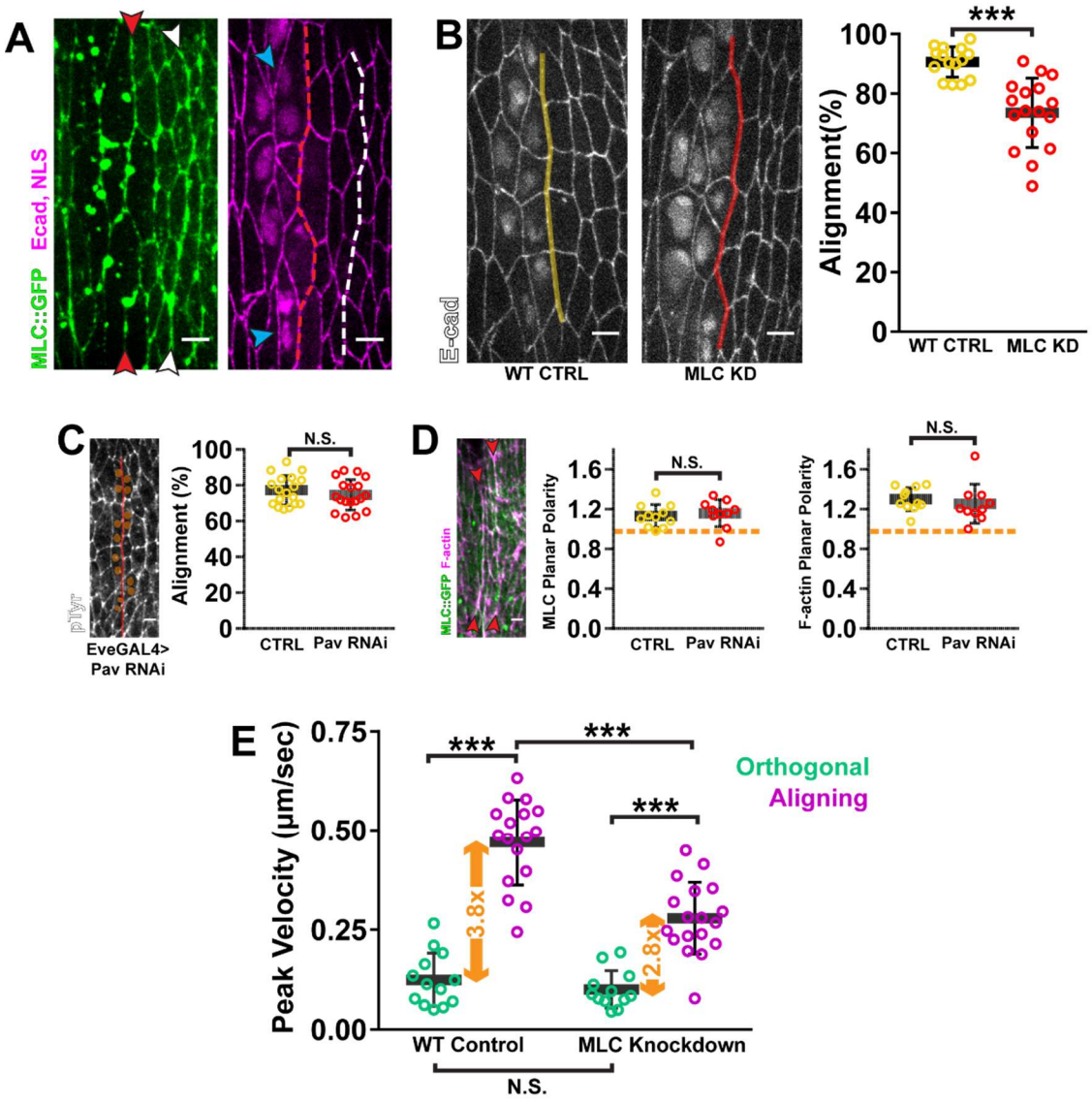

Figure 3.3: Actomyosin cables create force asymmetry to drive alignment

(A) Depletion of MLC along one interface (red arrowheads) caused alignment defects (red dashed line). Cell junctions were visualized with E-cad::tdTomato and deGradFP-expressing cells identified by nuclear mCherry signal. Blue arrowheads mark bi-nucleated cells caused by MLC knockdown. Depletion was restricted to the anterior interface and did not affect the morphology of the posterior interface (white arrowheads and dashed line).

(B) MLC knockdown ("MLC KD", red, right fluorescent image) caused a significant decrease in alignment compared to that of embryos expressing untagged MLC as a control ("WT CTRL", yellow, left fluorescent image). E-cad::tdTomato was used to visualized cell outlines. Nuclear signal marks cells expressing Engrailed-GAL4 > DeGradFP. WT CTRL: 15 interfaces, 6 embryos; DeGradFP+: 17 interfaces, 6 embryos

(Figure 3.3 Continued)

(C) Blocking cytokinesis by Pavarotti knockdown did not cause alignment defects. The position of nuclei in binucleated cells along the aligning interface were identified by Hoechst staining in deeper sections (not shown) and are marked in orange. In the graph, red shows alignment measurements of Eve-GAL4 > Pav RNAi interfaces while yellow are control, non-expressing interfaces. pTyr staining marked cell outlines. CTRL: 11 interfaces, 4 embryos; Pav RNAi: 12 interfaces, 4 embryos

(D) Pav knockdown also did not affect F-actin (magenta) or MLC (green) enrichment to aligning interfaces. CTRL: 11 interfaces, 4 embryos; Pav RNAi: 11 interfaces, 4 embryos

(E) MLC knockdown resulted in a significant decrease in tension compared to WT control along aligning contacts (purple), but no significant change along orthogonal contacts (green). The net result is a reduction in tension asymmetry (orange arrows). WT CTRL: 13 orthogonal junctions, 7 embryos, 17 aligning junctions, 5 embryos; DeGradFP+: 12 orthogonal junctions, 5 embryos, 18 aligning junctions, 6 embryos

***$p<0.0001$, Mann-Whitney U-test, Error bars = S.D. Scale bars = 4μm. Error bars = S.D.

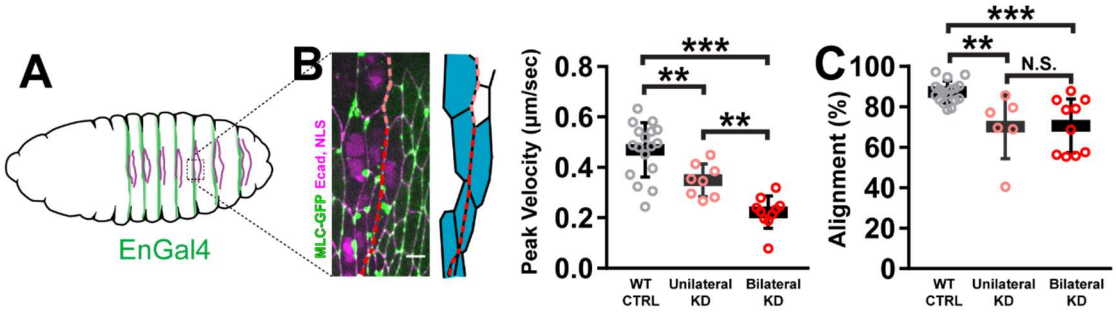

Figure 3.4: Alignment requires that contractile force be contributed from both sides of the interface

(A) A schematic of the Engrailed-GAL4 expression pattern (green) on the ventral face of the embryonic epithelium. Aligning interfaces are marked with purple lines. Only the anterior interface of each pair will be affected by Engrailed-GAL4.

(B) Engrailed-GAL4 variably expressed DeGradFP in cells at the anterior aligning interfaces. NLS-mCherry positively marked Engrailed-GAL4 expressing cells. Along the anterior aligning interface (dashed line), cells affected by DeGradFP-mediated MLC depletion are schematically shown in blue. Cells anterior (left) of the interface always expressed DeGradFP. Without expression on the posterior side (right), this resulted in unilateral knockdown (pink dashed lines and data points). Variably, Engrailed-GAL4 expressed DeGradFP in cells posterior to the interface, resulting in bilateral knockdown (red dashed lines and data points). Both cases resulted in decreased cortical tension compared to aligning junctions in wild-type controls (gray). Bilateral knockdown caused a greater reduction in tension compared to unilateral knockdown. WT CTRL: 17 junctions, 6 embryos; Unilateral KD: 8 junctions, 6 embryos; Bilateral KD: 10 junctions, 10 embryos)

(C) Alignment was equivalently defective in both unilateral and bilateral knockdown scenarios.

***p<0.0001, **p<0.001, Mann-Whitney U-test, Error bars = S.D. Scale bars = 4µm. Error bars = S.D.

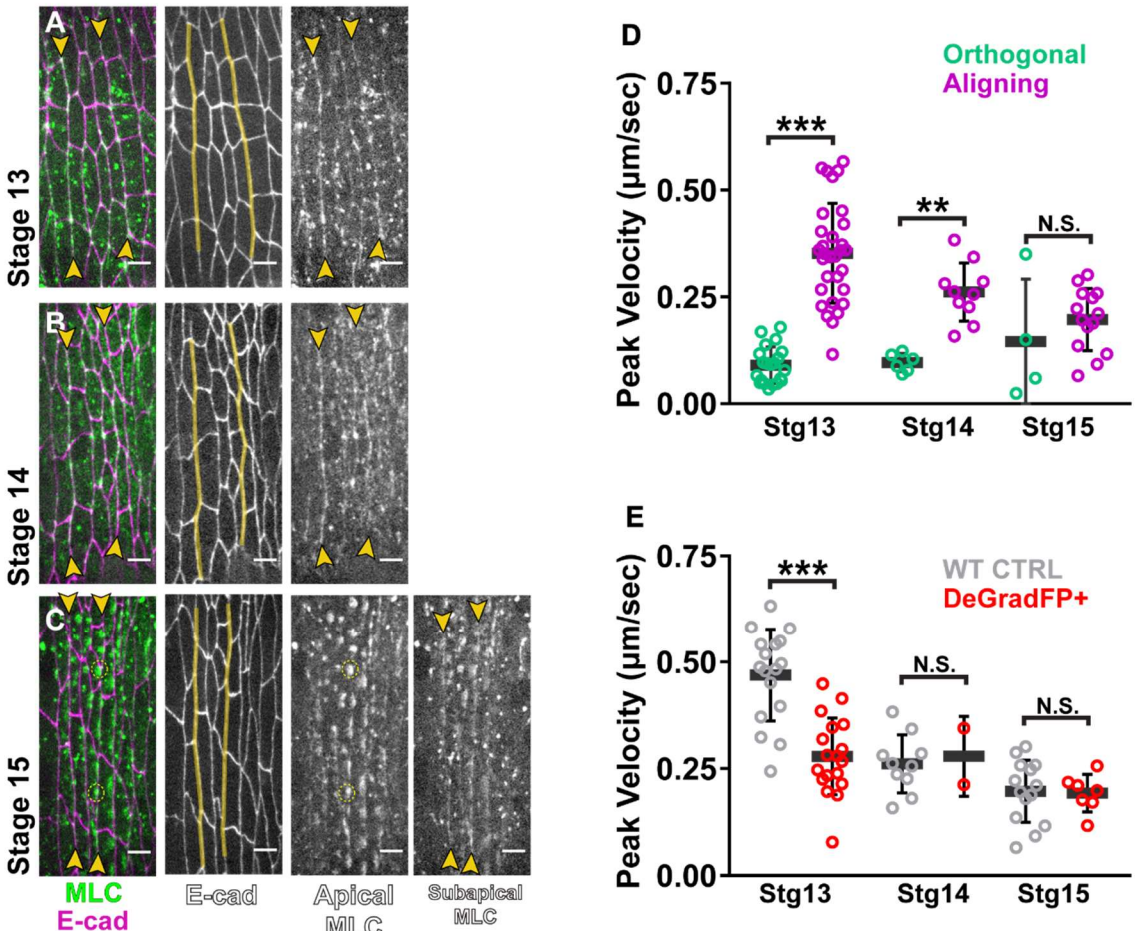

Figure 3.5: The aligned geometry is stabilized independent of actomyosin contractility later in development

(A-C) The aligned geometry and actomyosin polarity are retained until the end of embryo development. Actomyosin cables the form at (A) Stage 13, when alignment is first completed, are retained through (B) Stage 14 and (C) Stage 15. (C) Myo-II (revealed by MLC::mCherry, green) forms an additional medio-apical meshwork starting at stage 14 that will eventually focus into puncta in Stage 15 (yellow dotted circle). 0.5um below the apical network, junctional enrichments of of MLC are still observed at aligning junctions. Interfaces (yellow arrowheads, lines) remain straight throughout these stages. E-cad::tdTomato marks cell outlines.

(D) The force asymmetry at aligning interfaces starts to decrease at Stage 14. By Stage 15, there is no longer a significant difference in force between aligning (purple) and orthogonal (green) junctions.

(Figure 3.5 Continued)

(E) In older embryos, myosin knockdown with deGradFP (red) does not decrease cortical tension significantly along aligning cell junctions compared to aligning junctions in control embryos (gray). This contrasts with the significant decrease in tension observed in stage 13 embryos. This demonstrates that the remaining cortical tension present in older embryos is no longer actomyosin derived.

***p<0.0001, **p<0.001, Mann-Whitney U-test, Error bars = S.D. Scale bars = 4μm. Error bars = S.D.

CHAPTER 4: Planar polarized Rho signaling is essential for alignment

Introduction

Another major objective of my thesis work was to identify the polarity cue for actomyosin accumulation at aligning interfaces.

I have found that planar polarization of Rho signaling is critical for alignment to occur. Both the ROK and Dia branches of the pathway are required enrichment of F-actin and Myo-II along junctions in the aligning interfaces. Furthermore, I present evidence the ROK has more functions in alignment than just phosphorylation of MLC.

Additionally, I explored the requirement for Par3, a polarity protein that can be regulated by ROK. Based on its spatial distribution, our lab previously proposed that Par3 may regulate alignment. However, I have found two different lines of evidence that Par3 does not have a direct role in coordinating alignment.

Results

Planar polarization of Rho signaling coordinates alignment

Given its role in regulating contractile actomyosin, I examined the localization of Rho pathway factors. A fluorescent sensor for activated, GTP-bound Rho exhibited a consistent, subtle enrichment along aligning contacts relative to orthogonal contacts (Fig. 4.1A purple vs green)[45]. Corroborating this, I found that the Rho effectors ROK and Dia, were also enriched along aligning contacts (Fig. 4.1B, C).

To test whether the Rho pathway is required for alignment, I disrupted these three components. First, analysis of strong loss-of-function *rho* mutants had significant alignment defects (Fig. 4.2A).

Second, I tested the necessity for ROK. Genetic depletion was problematic due to the maternal and zygotic contribution of ROK, coupled to the relatively late stage during which alignment takes place. Instead, I injected either of two ROK inhibitors, Y-

27632 and H-1152, each which caused a rapid loss of alignment in contrast to embryos injected with solvent alone (Fig. 4.2B).

Finally, to evaluate the function of Dia, I used complementary genetic and pharmacological approaches. The epithelium of embryos homozygous for a null allele of *dia* was frequently too disrupted to analyze alignment (Fig. 4.3F). However, heterozygous embryos (dia^2/+) had significant alignment defects compared to homozygous, wild-type (+/+) embryos (Fig. 4.3A-D yellow vs pink). To further deplete Dia activity, I analyzed dia^2/+ embryos laid by dia^2/+ females. These embryos had more severe alignment defects relative to dia^2/+ embryos laid by +/+ females, showing that depletion of maternally-contributed Dia compromises alignment further (Fig. 4.3B, C, D pink vs red). Detection of alignment phenotypes even with mild perturbations of Dia suggested a critical role for this formin in alignment.

To achieve stage-specific disruption of Dia during alignment, I treated embryos with the formin inhibitor, SMIFH2[85]. Analysis of expression data for all formin family members indicated that Dia is the only formin present and cortically enriched to aligning interfaces (Fig. 4.3E). Therefore, the effects observed from SMIFH2 treatment can be attributed to the inhibition of Dia.

SMIFH2 treatment caused a significant loss of alignment (Fig. 4.3G). Additionally, individual cell junctions across the epithelium became convoluted in morphology (Fig. 4.3F, barbed arrows), further suggesting a role for Dia in regulating cortical tension[86,87].

Taken together, our data indicates that alignment requires planar polarized ROK and Dia activation via Rho.

Dia and ROK are each required for both F-actin and Myo-II planar polarization

ROK and Dia have well-studied roles in regulating Myo-II and F-actin, respectively. I sought to test whether these factors are necessary for formation of actomyosin cables. As such, I monitored the localization of fluorescently-labelled MLC and an F-actin sensor in response to pharmacological inhibition of ROK or Dia. Before and after treatment, I measured the ratio of fluorescence between aligning and orthogonal junctions and used this as a metric of local planar polarity.

For inhibition of ROK, I used the drug Y-27632 (referred to in this and subsequent experiments as “ROK inhibitor”). Injection of the Y-27632 inhibitor caused an immediate depletion of MLC from cell junctions and a loss in its planar polarity (Fig 4.4A). This is consistent with the known role of ROK in activating Myo-II through phosphorylation.

I next sought to test whether phosphorylation by ROK was sufficient for proper localization of Myo-II. Since inhibitor treatment should block MLC phosphorylation, I tested whether artificially restoring phosphorylation could rescue cortical enrichment and polarization. Phosphomimetic MLC does not rescue the enzymatic activity of Myo-II, but it does allow insight into the phosphorylation dependence of Myo-II localization[88,89]. I examined embryos exogenously expressing a GFP-tagged form of the phosphomimetic mutant MLC in addition to endogenous, wild-type un-tagged MLC. Phosphomimetic MLC enriched along aligning junctions at levels comparable to wild-type MLC expressed with a similar transgenic strategy (Fig. 4.5A-D). This is likely due to co-assembly of phosphomimetic MLC and endogenous MLC into mini-filaments that can be recruited normally to cell junctions.

Upon inhibition of ROK, wild-type MLC-containing mini-filaments would disassemble, whereas phosphomimetic MLC would still form mini filaments with Myosin Heavy Chain. These mini filaments would be recruited to the cortex, but accumulate in a non-polarized manner given the loss of polarized ROK activity. Such symmetric

recruitment is precisely what is observed in embryos earlier in development treated with ROK inhibitor [70]. Surprisingly, during alignment, treatment with the ROK inhibitor not only led to a loss of planar polarity but to depletion of Myo-II from all cortices, as demonstrated by a dramatically reduced fluorescence intensity measured at both aligning and orthogonal junctions (Fig. 4.5A, C, D, E, G, H). These changes were comparable to that exhibited by non-phosphomimetic MLC (Fig. 4.5A, B, E, F). As expected, expression of the phosphomimetic construct did not rescue alignment defects in embryos treated with ROK inhibitor (Fig. 4.5I). These observations suggest that ROK regulates Myo-II targeting to cell junctions in a manner independent of its ability to phosphorylate MLC. I also observed that F-actin became severely disorganized upon ROK inhibition (Fig. 4.4B). In turn this suggests that ROK has a separate function in remodeling F-actin during alignment, in addition to Myosin activation.

Dia disruption also had profound effects on F-actin and Myo-II distribution. Upon SMIFH2 treatment, F-actin planar polarity at aligning interfaces was lost (Fig. 4.4C). This indicates that Dia is the primary driver of actin polymerization in the contractile assemblies that promote alignment. Additionally, planar polarity of MLC was compromised with SMIFH2 treatment (Fig. 4.4D). This demonstrates that Dia-mediated actin remodeling is required to properly incorporate Myo-II into the actomyosin cable.

Our findings show that each of these Rho effectors is necessary to assemble both F-actin and Myo-II into the supracellular cables.

Par3 is not required for alignment

Our lab previously reported that Par3 is preferentially enriched along orthogonal junctions and depleted along aligning junctions (Figure 4.1A, B) [49]. Par3 is a classic regulator of apical-basal polarity, but has also been shown to function in planar polarized processes[70,90,91]. Specifically, during convergent extension, Par3 is preferentially

enriched along non-shrinking junctions where it is thought to repress Myo-II activity[70]. Indeed, its exclusion from shrinking junctions arises due to ROK. ROK is enriched along shrinking junctions, where it can phosphorylate and thereby inhibit Par3 association with the membrane. Given the similar distribution of ROK and Par3 during alignment, it would make sense that Par3 played a role in this process.

To test Par3s function in alignment, I examined embryos with a strong loss-of-function allele for Par3, *baz*$^{815.8}$[92]. I confirmed that mutant embryos have very little Par3 protein by antibody stain (data not shown). Homozygous mutant embryos had no significant alignment deficit compared to control siblings (Fig. 4.6A). To confirm this result, I knocked down Par3 using the deGradFP approach on an endogenously GFP-tagged Par3 expressing line. As described in Chapter 3, I restricted knockdown to the first anterior interface in each abdominal segment by expressing deGradFP with EngrailedGal4. Qualitatively, it appears that deGradFP+ embryos are intact for alignment (Fig. 4.6B). This experiment would benefit from quantification, but Par3 depleted embryos appear completely wild type with respect to alignment. This cumulative data set strongly indicates that Par3 is not required for alignment.

Discussion

Planar polarized Rho is the guidance cue for actomyosin cable assembly

I have demonstrated an essential role for polarization of Rho signaling as a spatial cue. Both branches of the Rho pathway – ROK and Dia – are critical for recruitment of Myo-II and F-actin into the supracellular cables that drive alignment.

This planar polarized distribution of Rho and ROK during alignment is nearly identically to that observed during convergent extension, where Rho- and ROK-upregulated junctions undergo shrinking. This begs the question of what molecularly differentiates these two morphogenetic processes. This question will be more deeply

explored in Chapter 5. However, it is worth noting that Dia is not enriched along Rho-activated junctions during convergent extension. This has been independently shown by two different research groups[30,71]. Whether this difference is functionally significant is not clear. The relative enrichment of Dia during alignment could represent some increased signaling through the actin polymerization branch of the Rho pathway. Additionally, there could be a factor that acts in parallel with Rho that activates or stabilizes Dia function. Experimental approaches that can more precisely down- and upregulate Dia activity in a spatially specific manner would allow further exploration of this question.

Both branches of the Rho pathway are required for actomyosin cables

It was interesting to find that both Rho effectors are required for proper recruitment of both F-actin and Myo-II into cables (Fig. 4.2, 4.3). It was not surprising to find that the formin, Dia, is required for F-actin accumulation at aligning interfaces. Additionally, I have shown that this actin remodeling activity is required for recruitment of Myo-II to these junctions. It is possible that mini-filaments prefer to bind to linear assemblies of F-actin that are promoted by Dia activity. Enhanced Dia activity at aligning junctions could encourage recruitment of Myo-II via this mechanism. This could explain the loss of Myo-II enrichment with Dia inhibition. The interaction between F-actin and Myosin will be investigated further in Chapter 5.

Potential functions for ROK outside of MLC phosphorylation

Similarly, ROK activity is not just required for Myo-II enrichment to aligning interfaces (Fig. 4.4A). F-actin was profoundly disorganized with ROK inhibition (Fig. 4.4B). This could be in part due to loss of MLC phosphorylation, as Myo-II can crosslink and stabilize F-actin networks[93]. However, I found that mimicking phosphorylation in

MLC was not sufficient to rescue Myo-II recruitment nor, apparently, any contractile activity upon ROK inhibition. Therefore, there may be a more direct effect on F-actin by ROK that is required for stabilizing Myo-II at junctions. ROK has numerous other phosphorylation targets that participate in F-actin remodeling[39]. Lim Kinase is one such example, which is a negative regulator of the actin depolymerizing factor, Cofilin[94]. Loss of Lim Kinase activity upon ROK inhibition could lead to aberrant depolymerization of F-actin by Cofilin. This would account for the loss of cortical F-actin I observed in embryos. Ezrin-Radixin-Moesin (ERM) proteins are another group of phosphorylation targets that serve as physical links between the membrane and actin filaments[95,96]. Reduced activation of proteins can also lead to F-actin disorganization[97]. Decreased cortical F-actin via either of these mechanisms could reduce the available filament binding sites available for Myo-II filaments, explaining the inability of both wild type and phosphomimetic Myo-II complexes to associate with cell junctions after ROK inhibition.

Is there a requirement for Par3 repression at aligning interfaces?

No alignment phenotype was observed with Par3 loss, demonstrating that the enrichment of Par3 along orthogonal junctions is not essential for alignment. However, this loss-of-function approach cannot address whether exclusion of Par3 from aligning interfaces is important. To test this, I would need to experimentally force the recruitment of Par3 to aligning junctions and observe the impact on alignment. This has been done in the context of lineage boundaries in the early embryos, where actomyosin supracellular cables are also present[98,99]. Overexpression of Par3 caused these boundaries to aberrantly ingress, creating ectopic furrows[99]. As will be discussed extensively in Chapter 5, Rho pathway overactivation causes a remarkably similar

phenotype. It could be that Par3 suppression along aligning interfaces is required for proper activity of actomyosin cables and/or the Rho pathway.

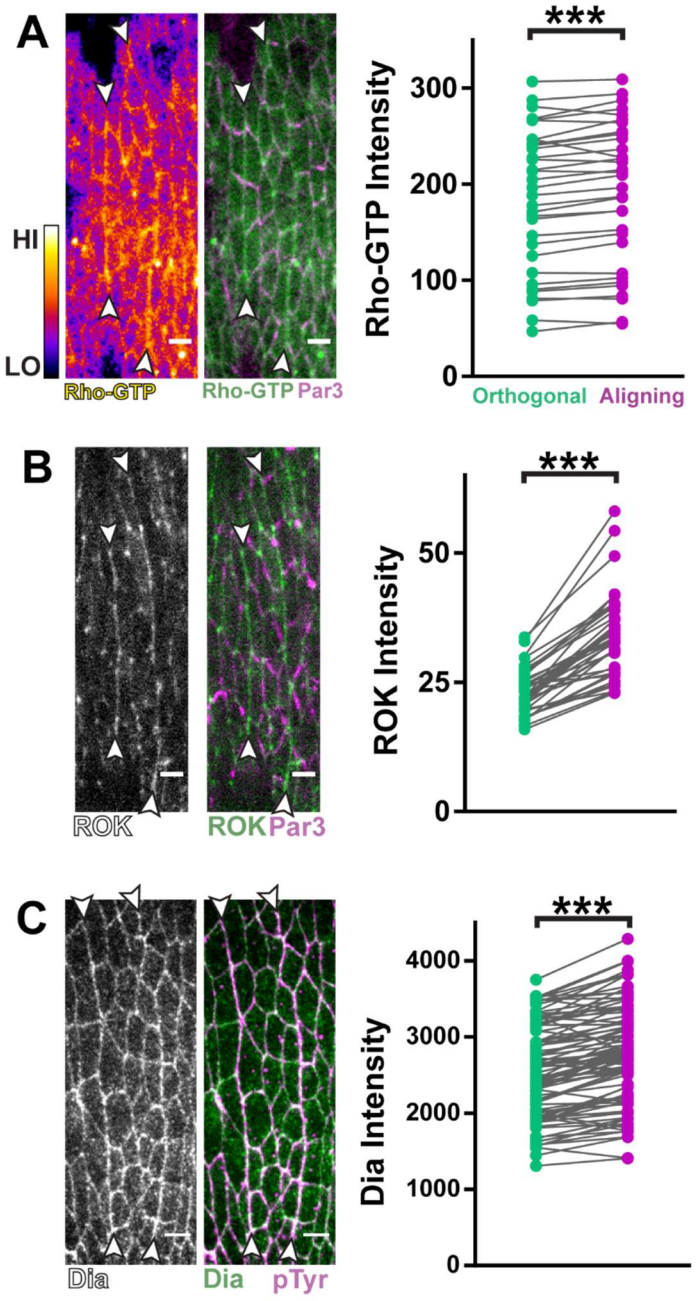

Figure 4.1: Rho signaling is planar polarized to aligning junctions

(A) A GFP sensor for Rho-GTP enriched along aligning junctions (purple in graph) relative to orthogonal junctions (green in graph). On the left, Rho-GTP signal intensity is displayed with the Fire LUT (calibration bar shows Low to High signal). N = 34 interfaces, 7 embryos.

(B) GFP::ROK^{K116A} enriched along aligning interfaces relative to orthogonal junctions. N = 38 interfaces, 7 embryos

(Figure 4.1 Continued)

(C) Dia, as detected by antibody stain, enriched along aligning junctions relative to orthogonal junctions. N = 98 interfaces, 8 embryos.

Par3::mCherry was used to mark AJs in (A, B, magenta).

phospho-Tyrosine (pTyr) antibody staining was used as a marker for cell outlines (C).

***p<0.0001, Mann-Whitney U-test, Error bars = S.D. Scale bars = 4μm.

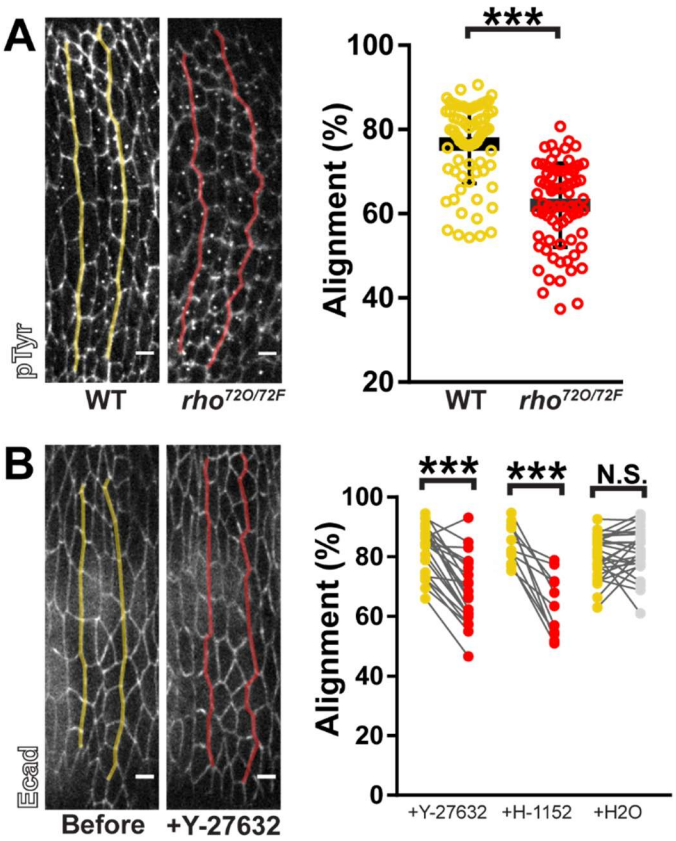

Figure 4.2: Rho and ROK are required for alignment

(A) *rho* loss-of-function mutants (red) had significant alignment defects compared to wild-type sibling controls (yellow). pTyr antibody staining was used to visualize cell outlines. CTRL: 76 interfaces, 6 embryos; $rho^{72O/72F}$: 75 interfaces, 5 embryos.

(B) Pharmacological inhibition of ROK with either Y-27632 or H-1152 caused significant decreases in alignment. Fluorescently-tagged E-cad was used to visualize cell outlines before (yellow) and after (red) drug treatments. Each line in the graphs of represents one interface and matches measurements before (yellow) and after drug treatment (red) or H_2O control injection (gray). Control injections with H_2O did not significantly reduce alignment. Y-27632: 21 interfaces, 5 embryos; H-1152: 11 interfaces, 3 embryos; H_2O: 26 interfaces, 6 embryos

***p<0.0001, Mann-Whitney U-test, Error bars = S.D. Scale bars = 4μm.

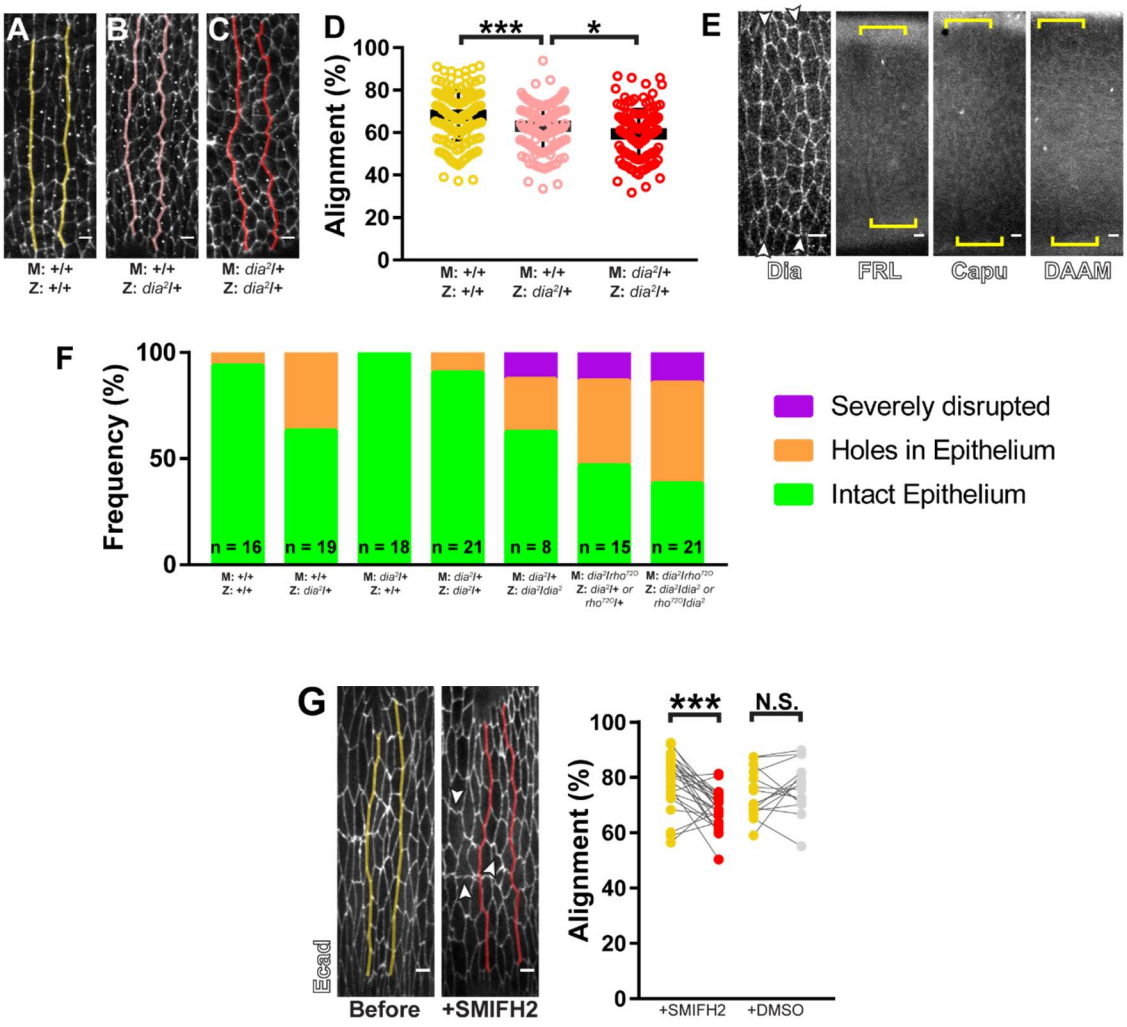

Figure 4.3: Diaphanous is the only formin required for alignment.

(A-D) Partial genetic depletion of Dia causes alignment defects. (B) Embryos heterozygous for the null allele *dia*^{2} (pink) experience a partial depletion of their zygotically (Z) contributed Dia protein. (A) Relative to wild type controls (yellow), this zygotic reduction caused significant defects in alignment (D yellow vs pink). (C) Embryos laid by heterozygous females experience an additional depletion of maternally(M)-contributed Dia protein (red). Heterozygous embryos of this category had more severe defects in alignment compared to *dia*^{2} heterozygotes laid by wild type mothers (D, pink vs red). (A-C) pTyr staining was used to visualize cell outlines. A: interfaces = 157, 13 embryos; B: 137 interfaces, 10 embryos; C: 126 interfaces, 12 embryos

(Figure 4.3 Continued)

(E) We surveyed high-throughput sequencing data sets and *in situ* hybridization studies (flybase.org) of all formins in the Drosophila genome. Only three (FRL, Capu and DAAM), are expressed during the developmental stages relevant to alignment (FRL, Capu and DAAM). For each of these, we assessed the localization of endogenously GFP-tagged transgenic lines. These three formins showed homogeneous cytoplasmic distributions with little cortical targeting, compared to Dia (visualized by antibody staining). Yellow brackets indicate region of aligning interfaces. Dia antibody stain: Representative of 8 embryos; FRL::GFP: representative of 10 embryos; Capu::GFP: representative of 12 embryos; DAAM::GFP: representative of 13 embryos

(F) Increased depletion of Dia is associated with more severe phenotypes that obfuscate analysis of alignment. While heterozygous embryos have mostly intact epithelium (green), upon further loss of Dia activity, a larger fraction of embryos have either some large holes in their epithelium (orange) or many holes and severe disorganization (magenta). Embryos with these two later phenotypes were not analyzed for alignment. N values are displayed for each sample group are displayed on the graph.

(G) Pharmacological inhibition of Dia caused significant decreases in alignment. White arrowheads indicate cell junctions that became convoluted after drug treatment. Fluorescently-tagged E-cad was used to visualize cell outlines before (yellow) and after (red) drug treatments. Each line in the graphs of represents one interface and matches measurements before (yellow) and after drug treatment (red) or DMSO control injection (gray). Control injections with H_2O did not significantly reduce alignment. SMIFH2: 27 interfaces from 6 embryos; DMSO: 16 interfaces from 3 embryos

***$p<0.0001$, *$p<0.01$, Mann-Whitney U-test, Error bars = S.D. Scale bars = 4μm.

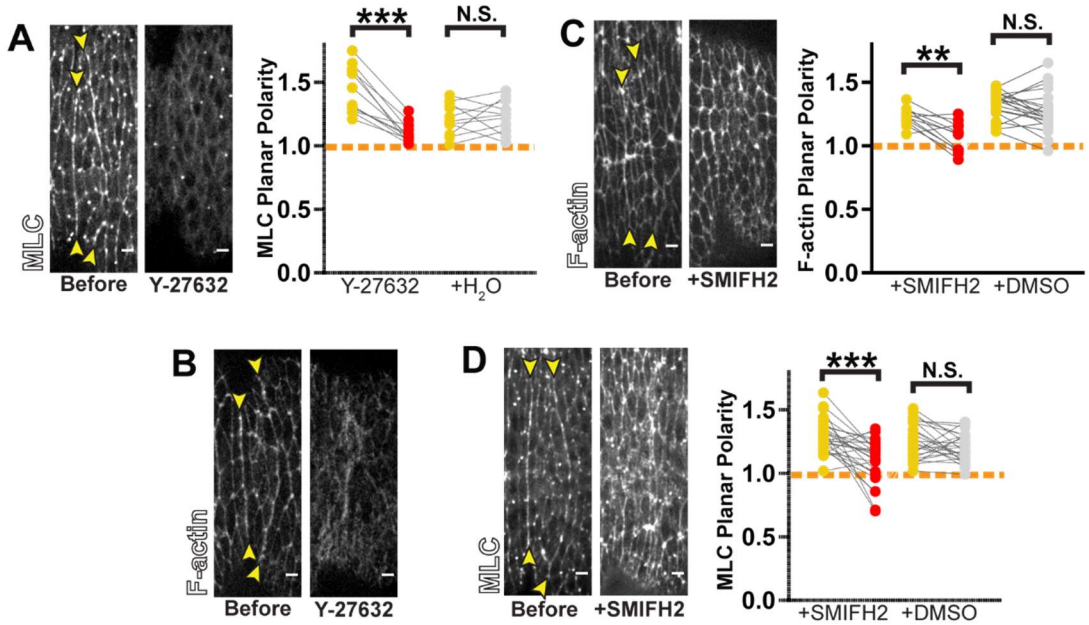

Figure 4.4: Rho effectors are required for actomyosin planar polarity.

(A and B) ROK inhibition caused loss in planar polarity of (A) MLC::GFP (Y-27632: 12 interfaces, 3 embryos; H_2O: 11 interfaces, 3 embryos) and (B) F-actin (representative of 7 embryos).

(C and D) Dia inhibition by SMIFH2 treatment caused loss in planar polarity of (C) F-actin (SMIFH2: 12 interfaces, 3 embryos; DMSO: 21 interfaces, 5 embryos) and (D) MLC::GFP (SMIFH2: 17 interfaces, 4 embryos; DMSO: 26 interfaces, 5 embryos)

Utr-ABD::GFP was used to visualize F-actin (B and C). Planar polarity was quantified as a ratio of fluorescence intensity between aligning and orthogonal regions. Each line in the graphs (A,C, D) represents one interface and matches the measurements before (yellow) and after (red) drug treatment.

Control injections with H_2O (for Y-27632) or DMSO (for SMIFH2) did not result in significant changes in planar polarity in either MLC or F-actin.

***p<0.0001, **p<0.001, Mann-Whitney U-test. Scale bars = 4μm.

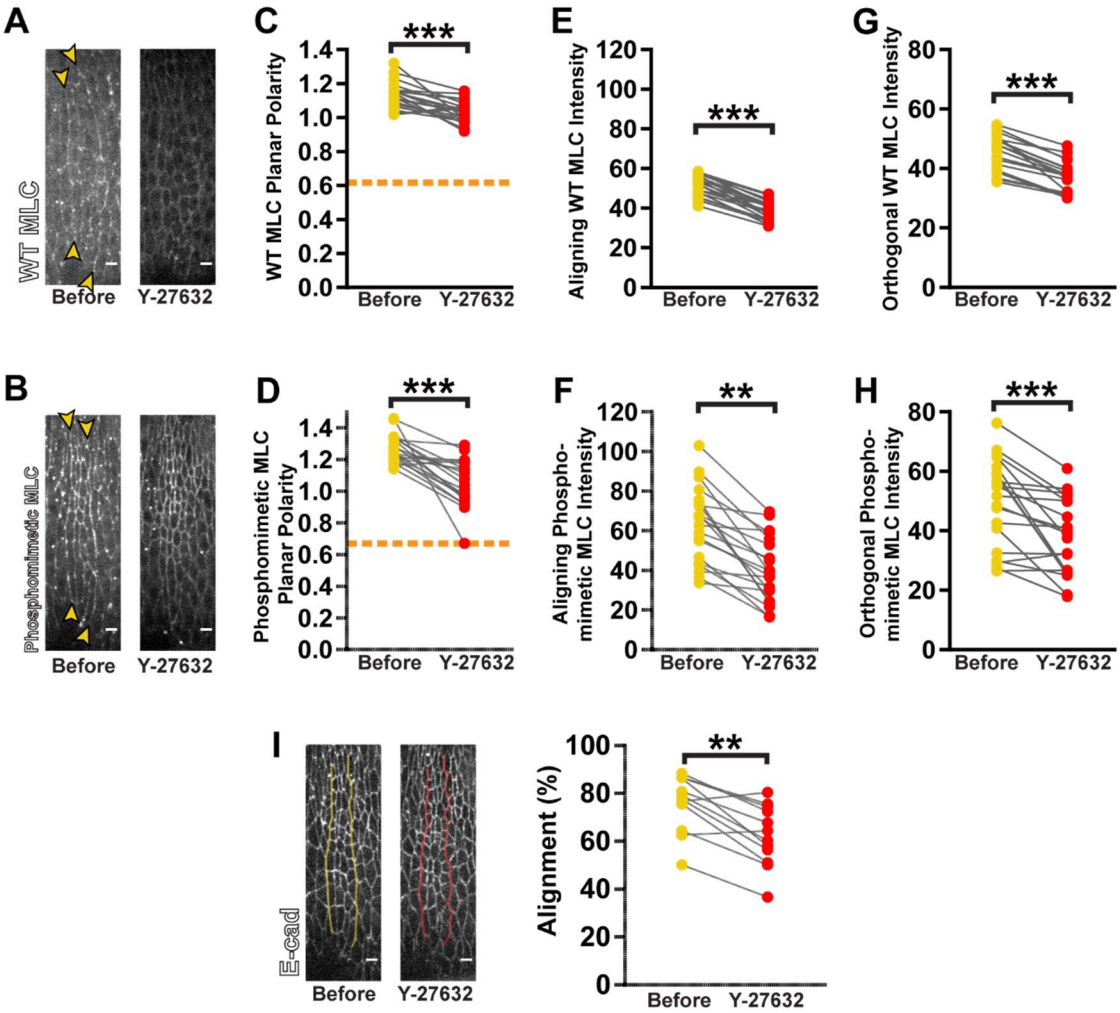

Figure 4.5: Phosphorylation is not sufficient for Myosin activity or polarity.

(A-H) Phosphorylation of MLC by ROK is not sufficient for junctional recruitment and planar polarity. (A) GFP-labelled wild type MLC or (B) phosphomimetic MLC were expressed with a similar transgenic strategy so that protein levels would not confound analysis. (C, D, yellow) Both versions of MLC were planar polarized properly to aligning interface. Upon ROK inhibition (red), both constructs lost (C, D) planar polarity and exhibited decreased cortical targeting to both (E, F) aligning junctions and (G,H) orthogonal junctions (G, H).

(I) Embryo expressing phosphomimetic MLC still exhibited significant alignment defects upon ROK inhibitor treatment. E-cadherin-tdTomato was used to visualize cell outlines. sqh-sqh^{WT}::GFP: 20 interfaces from 5 embryos; sqh-sqh^{EE}::GFP: 20 interfaces from 6 embryos

Each lines in graphs represents one interface and matches measurements before and after drug treatment.

***p<0.0001, **p<0.01, Mann-Whitney U-test, Scale bars = 4μm.

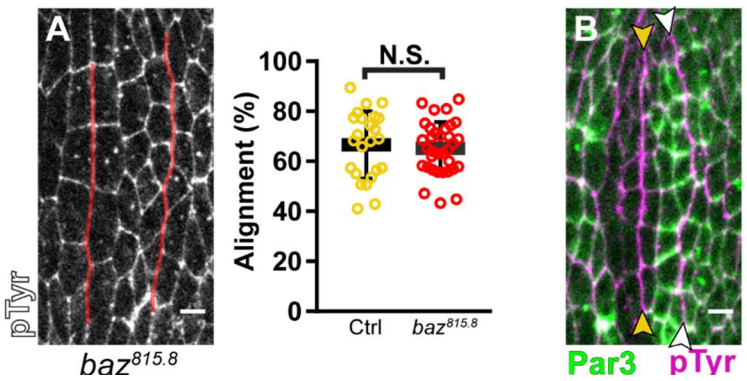

Figure 4.6: Par3 is not required for alignment.

(A) Embryos with a strong hypomorphic allele of Par3, *baz*$^{815.8}$ (red lines and data points), do not have an alignment phenotype relative to control siblings (yellow).

(B) DeGradFP mediated knockdown of Par3 (green) did not disrupt alignment (red arrowheads). White arrowheads mark the unaffected second interface. pTyr (magenta) marks cell outlines.

Mann-Whitney U-test, Scale bars = 4μm.

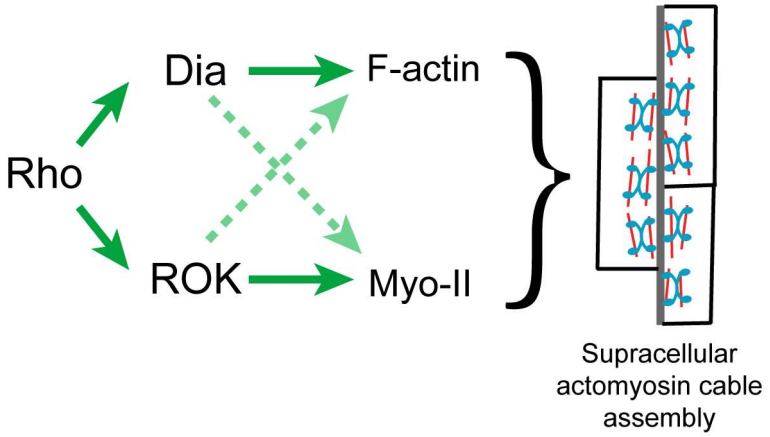

Figure 4.7: Model of Rho pathway function in alignment

Model of Rho effector function in forming actomyosin cables during alignment. Dashed green arrows represent interactions that are not mechanistically well understood and may be direct or indirect.

Chapter 5: Multiple feedback mechanisms fine-tune Rho signaling to regulate morphogenetic outcomes

Introduction

Rho signaling is required in many morphogenetic programs, but how this pathway allows for production of distinct cell and tissue morphologies is still poorly understood. One contributing factor is spatial regulation of Rho activation. As described in Chapter 4, I have demonstrated that planar polarization of Rho activation and its effectors to aligning junctions is critical for the formation of actomyosin cables, thereby driving alignment.

However, planar polarization of Rho can result in cell geometries different from alignment. Two such examples are convergent extension and mechanical tissue boundaries. During convergent extension, junctions along the dorsal-ventral axis become upregulated for Rho signaling[42,45,46], initiating the formation of actomyosin asymmetry[28,31]. At mechanical boundaries, actomyosin cables also increase force along cell-cell contacts in order to prevent cell mixing between tissue compartments[16,17,33,47,98]. Studies suggest that Rho signaling is also polarized to guide the formation of these boundaries in many tissues (unpublished from our lab)[16,17,33,47].

These two processes strongly resemble alignment in the manner that Rho signaling and actomyosin remodeling is polarized to create local force asymmetry in the tissue[16–19,33]. Yet, the final resulting morphologies of these events are quite different from one another. During convergent extension, junctions activated for Rho and actomyosin will shrink and remodel[28,31]. At tissue boundaries, cell-cell contacts also shorten in length and partly align with one another[16,17]. In contrast, alignment produces very straight interfaces of cell-cell contacts where individual contacts elongate relative to neighboring, orthogonal contacts (Figure 1a). Indeed, the observation that the contacts under the most tension are competent to lengthen is contrary to most current *in silico* models[52,53], highlighting a key distinguishing feature of alignment.

Given that these systems do not appear to exhibit differences in the spatial deployment of Rho or its effectors, other mechanisms must account for these disparate morphological outcomes. In this report, I present evidence that pathway feedback could allow for modification of Rho signaling outcomes. I explored the interactions among the major components in the Rho pathway. Consistent with reports in other morphogenetic processes, I found that F-actin negatively feeds back to Rho activation [100–102]. It appears that ROK may mediate some aspects of this interaction. I also present evidence that suggests a novel feedback interaction between F-actin and Dia. In contrast to observations in other systems, I found no role for Myo-II activity nor contractility in feedback regulation of Rho[45,102–104]. However, it seems that ROK is able to positively regulate Dia in a Myo-II independent manner. These results suggest that numerous feedback interactions can fine-tune Rho signaling to allow for plasticity in morphological outcomes.

Results

Constitutive activation of Rho effectors changes the morphogenetic activity of actomyosin cables

To further probe the function of the Rho pathway during alignment, I tested the effect of overactivating Rho effectors. I expressed constitutively-activated ROK (ROK-CA)[70,105] or Dia (Dia-CA)[71] along a broad patch of the epithelium (Fig 5.1A, Opa-GAL4). Activating either effector caused ectopic furrows that coincided with aligning regions, while adjacent non-aligning regions remained flat (Fig. 5.1B-F). To confirm that the invaginations correspond with aligning regions, I examined the localization of the marker Cubitus interruptus, which accumulates in a segmental pattern beginning in the cells posterior to the first aligning interface (Fig. 5.1D). I always observed the border of

this expression domain in the ectopic furrow (Fig. 5.1E,F arrowheads). Additionally, upon expression of the constitutively active effectors in alternating segments (Fig. 5.2A, Eve-GAL4), the aligning interfaces were no longer apparent in the expressing segments because they were hidden in the furrows (Fig. 5.2B, red vs yellow bracketed regions). These ectopic furrows were previously described by other groups and attributed to aberrant persistence of grooves that form normally early in development[71,106]. However, my live imaging showed that the early appearing grooves regressed normally despite constitutively active effector expression (data not shown). Thus, the furrows arise *de novo* at aligning interfaces.

I found ROK-CA expression caused additional, irregular changes across the epithelium (Fig. 5.1G). These cell shape changes do not appear to be relevant to furrow formation, as I did not observe this in Dia-CA expressing embryos (Fig. 5.2C, 5.3A). Therefore, I focused on Dia-CA expression to investigate how furrows form.

Initially, I hypothesized that furrows result from the absence of the spatial cue that promotes actomyosin assembly. Expression of constitutively active effectors that accumulate along all cell junctions would lead to apolar upregulation of actomyosin. Apolar cytoskeletal forces would cause isotropic apical constriction, leading to furrow formation [13].

However, I was surprised to observe that apical constriction was anisotropic in cells expressing Dia-CA (Fig. 5.2C). Using Eve-GAL4 to express Dia-CA in alternating segments (Fig. 5.2A, B, Eve-GAL4), I indeed observed decreases in cell surface area in aligning cells as the furrow deepened compared to cells in non-expressing segments within the same embryo (Fig. 5.2C-E, G red vs yellow). If anything, these control cells slightly increase in surface area (Fig. 5.2E, G yellow). This increase was comparable to that observed in cells within wild type embryos (Fig. 5.2G gray). As apical surface area of furrowing cells decreased, cells became more anisotropic along the axis of alignment,

the result of contraction along the orthogonal axis (Fig. 5.2C, D, H red vs yellow & gray). This asymmetric behavior is not consistent with the hypothesis that depolarized Rho signalling drives furrow formation.

In fact, when I examined the distribution of F-actin just prior to when aligning interfaces fully ingressed into furrows, I observed that planar polarity was maintained at levels comparable to that of control interfaces (Fig. 5.3A, B). This was observed when expressing Dia-CA with either Eve-Gal4 (Fig. 5.3A) or Opa-GAL4 (data not shown). The same retention of planar polarity was observed for MLC (Fig. 5.3D, E), suggesting the actomyosin remain polarized along aligning junctions. As expected from constitutive activation of a formin, I did find that F-actin levels were significantly elevated at interfaces with Dia-CA expression relative to control interfaces (Fig. 5.3C). However, surprisingly, this did not correspond with an increase in MLC (Fig. 5.3F).

Given that there is no apparent change to the polarized distribution of actomyosin, the data suggest that furrow formation is caused instead by a change in the activity of those polarized assemblies. That change might be linked to the increase in F-actin level driven by Dia-CA, or possibly in the organization of that actin (see Discussion).

F-actin mediates negative feedback to multiple levels of Rho signaling

The generation of these ectopic furrows suggests strongly that there are mechanisms in place to temper Rho pathway activity during alignment. Feedback is one such mechanism that could moderate of Rho signaling and regulate morphological outcomes. Given the correlation between furrow formation and increased F-actin polymerization, I next asked whether F-actin itself could feedback to Rho. Indeed, recent studies have shown that F-actin can negatively feedback to Rho in other systems [100,101]. Therefore, I assessed the response of the Rho pathway after treatment with

Latrunculin B (LatB). Injection of LatB caused a rapid loss of F-actin from cell junctions, indicating increased depolymerization (Fig. 5.4A, Movie 1). The remaining signal was found in foci, indicating severe filament disorganization as well (Fig. 5.4A, Movie 1).

Consistent with previous reports, LatB treatment led to upregulation of Rho-GTP, as high intensity puncta of Rho-GTP appeared rapidly after treatment (Fig. 5.4B-D, Movie 2). These puncta were located in the plane of adherens junctions (AJs), indicating that these represent cortical overactivation of Rho rather than artifactual aggregation of the sensor (Fig. 5.4B, Movie 2). Quantification showed that total Rho-GTP at aligning junctions increased significantly (Fig. 5.4C). Assessment of planar polarity was complicated by the punctate, heterogeneous signal, but my measurements showed no significant differences in relative enrichment at aligning junctions (Fig. 5.4D). This suggested to us that the unknown, upstream signal that orients Rho activation is unperturbed by this manipulation.

As expected from aberrant overactivation of Rho, both ROK and Dia distribution were disrupted with LatB treatment. While there were no consistent changes in ROK planar polarity or levels at aligning junctions, its distribution became more punctate and heterogeneous at cell junctions (Fig. 5.4E-G, Movie 3). Dia signal also became more punctate (Fig. 5.4H, Movie 4). In contrast to ROK, the amount of Dia at aligning junctions increased consistently whereas planar polarity was not disturbed (Fig. 5.4I, J, Movie 4). The dissimilar responses by Dia and ROK to LatB treatment may reflect differences in the manner by which Rho activates each effector.

To understand mechanistically what is mediating negative feedback between F-actin and Rho, I used Cytochalasin D (CytoD), which had a different effect on F-actin in the embryo. Upon CytoD treatment, F-actin levels did not decrease, but qualitatively appeared to increase, indicating no net depolymerization (Fig. 5.5A, Movie 5). However, F-actin distribution was broadly disrupted. There was an obvious loss of planar polarity

at the aligning interfaces along with formation of aberrant foci at cell edges (Fig. 5.5A, B, Movie 5). This likely reflects ectopic F-actin assemblies and dramatic changes in filament organization.

Surprisingly, this inhibitor caused no significant changes in recruitment or planar polarity for Rho-GTP and ROK (Fig. 5.5E-J). However, CytoD treatment dramatically increased Dia levels at aligning junctions (Fig. 5.5B, C). Dia planar polarity was retained with a small increase in enrichment along aligning interfaces (Fig. 5.5D). I considered the possibility that the effect on Dia was simply due to non-specific binding to the ectopic F-actin aggregates generated by CytoD. However, Capping Protein Beta (CapB), another barbed-end binding protein, exhibited no increased or decreased recruitment to aligning cell junctions (Fig. 5.5K). Therefore, the upregulation of Dia recruitment to cell junctions suggests that there is selective negative feedback from F-actin to the Dia branch of Rho signaling (Fig. 5.5L). The organization of actin filaments may be the cue for this feedback, as upregulation of Dia did not correlate with net actin depolymerization.

Cumulatively, our observations suggest negative feedback from F-actin to multiple points in the Rho pathway, engaging distinct mechanisms for each of these interactions (Fig. 5.4K vs 5.5L).

Positive cross-talk between F-actin and Myo-II in actomyosin cables

I then tested whether the two cytoskeletal components regulate each other. MLC depletion by deGradFP caused a decrease in F-actin levels along aligning interfaces resulting in attenuation of planar polarity (Fig. 5.6A-C). Reciprocally, exposure to either CytoD or LatB caused an immediate decrease in MLC planar polarity (Fig. 5.6D, E). Thus, mutual positive feedback between Myo-II and F-actin is critical to formation of actomyosin cables.

Contractility and Myo-II do not regulate Rho signaling

Myo-II itself has also been shown to feedback to Rho. Additionally, I demonstrated that F-actin levels decrease with MLC knockdown. This suggests that Myo-II could also regulate the Rho pathway through F-actin.

I could not assess the effect of Myo-II disruption on Rho activation directly, nor analyze ROK, because these assays require a GFP-tagged sensor or reporter, respectively. Since DeGradFP-mediated knockdown targets the GFP moiety, this would also interfere with analysis of any other GFP-tagged factors in those cells. However, I were able to analyze Dia levels using antibody staining. Surprisingly, MLC knockdown affected neither the level of Dia along aligning junctions, nor its polarized enrichment to those junctions (Fig. 5.7A-C). This suggests that there is no feedback from Myo-II to Rho signaling in the context of alignment, with the caveat that I could not directly assay Rho activity. If feedback is indeed absent, this contrasts to other cases in which Myo-II has been shown to feedback to Rho either positively or negatively [45,102,103,107].

Collectively, our data indicates not only that F-actin-mediated negative feedback is independent of contractility, but that it also does not rely on total actin filament levels. This latter insight follows from the observation that a reduction of F-actin caused by MLC knockdown did not correlate with a change in Rho pathway activity. Instead, I hypothesize that actin filament organizational changes are the cue for feedback (see Discussion).

ROK positively regulates Dia in a Myo-II independent manner

While Myo-II did not appear to feedback to Rho signaling, I wanted to test if ROK has any feedback interactions with the pathway independent of its ability to activate Myo-II. Indeed, after ROK inhibitor treatment, I observed a dramatic elevation in Rho-

GTP levels (Fig. 5.7D, F). Planar polarity of Rho-GTP was maintained, indicating that the underlying polarity signal orienting Rho activation does not rely on ROK (Fig. 5.6E). Given that F-actin is significantly disorganized with ROK inhibition (see Chapter 4, Fig. 4.4B) and that LatB-mediated disruption of F-actin also resulted in an upregulation in Rho-GTP (Fig. 5.4B, C), I hypothesize that an F-actin remodeling activity of ROK mediates negative feedback to Rho.

While ROK inhibition increased Rho-GTP levels, it did not increase Dia levels at aligning junctions (Fig. 5.7G, I). However, Dia planar polarity was lost (Fig. 5.7H), despite the maintenance of Rho polarity (Fig. 5.7D, E). This indicates that ROK has a separate role in maintaining Dia enrichment at aligning interfaces.

Discussion

The plasticity of Rho signaling outcomes

At both cytoskeletal and signaling levels, alignment strongly resembles two other morphogenetic processes -- convergent extension and mechanical boundary formation. These two processes produce a cell geometry distinct from alignment. Convergent extension results in junctions that shrink completely[28,31]. Junctions also shorten along mechanical boundaries[16,17,32]. In contrast, junctions elongate during alignment despite being under cortical tension at a level comparable to both convergent extension and mechanical boundary formation[16–19,32,33]. In all three cases, the force asymmetry is driven by supracellular actomyosin cables[16–19,47] that are assembled downstream of Rho planar polarization. How Rho is able to orchestrate these very different cell shape changes while initiating the same downstream events is perplexing and was the primary motivation for our studies on feedback.

Overactivation of the Rho pathway alters the morphogenetic output of actomyosin assemblies

Overactivation of Rho effectors in the aligning epithelium provided the first hint that feedback regulation allows for plasticity in pathway outcomes. Constitutive activation of either Dia or ROK altered the activity of actomyosin cables to yield a distinct tissue morphology – tissue invagination.

It is unclear how the structure or activity of actomyosin cables is modified to produce furrows. Increased Myo-II activity can induce ectopic furrowing in the early embryo[99]. However, I did not observe increased MLC recruitment in our system. It remains possible that changes in the distribution of mono- and di-phosphorylated MLC, and therefore some change in Myo-II activation that I could not assess might account for furrowing. However, in the aforementioned study in early embryos, the increased recruitment of MLC did not correlate with additional contractile force along the plane of AJs [99]. It is notable that the furrows I observed correlated with an increase in F-actin polymerization. Perhaps this changes the organization and/or activity of contractile assemblies leading to furrowing. For example, a reorganization of assemblies might shift the direction of contractile force generated rather than its magnitude. Another reasonable hypothesis is that the additional filaments allow actomyosin cables to mechanically engage with other contractile assemblies, such as medio-apical actomyosin. Connectivity of the medio-apical actomyosin network to junctions is critical for ventral furrow formation in the early embryo, and the emergence of this furrow is also coupled to anisotropic apical constriction as I observe in our system[7]. Further exploration of this question will provide insight into why moderation of Rho effectors is important for differentiating the function of actomyosin in morphogenesis.

Self-regulation of Rho signaling through feedback

Our study suggests a number of feedback interactions in the pathway that could temper Rho activity during alignment (Fig. 5.8). Consistent with other works [100–102], LatB treatment revealed a potential role for negative feedback from F-actin to Rho activation. While some RhoGAPs have been implicated in this regulatory loop, the underlying mechanisms are mostly unknown[101,102]. The broad conservation of this feedback suggests that many relevant players are still to be identified[101,102]. While corroboration of our findings with genetic approaches to manipulating F-actin would extend the power of our study, our data yield three significant insights into this potential mechanism.

First, it is not mediated by contractile force, as disruption of Myo-II did not appear to increase Rho pathway activity. This contrasts with several morphogenetic events where Myo-II activity positively regulates Rho [45,102,103]. The lack of feedback between Myo-II and Rho during alignment is supported by the fact that I observed no increase in Myo-II levels upon Rho pathway overactivation. Indeed, there have been recent reports of oscillating Rho activity in other systems that are Myo-II independent [101,108], corroborating the idea that contractile feedback is not a universal property of the Rho pathway. The activation state of Rho is primarily determined by GTPase Activating Proteins (RhoGAPs) that turn off Rho and Guanine Exchange Factors (RhoGEFs) that promote its activation. It is possible that only a subset of RhoGAPs/GEFs are responsive to feedback from Myo-II and that this subset does not participate in alignment. If this is the case, context-dependent control over specific RhoGAPs/GEFs may be a strategy for differentiating signaling outcomes. For example, one mediator of negative feedback between Myo-II and Rho has recently been identified in the Arf-GEF, Steppke [107]. I found that alignment occurred normally in *steppke* mutant embryos (data not shown), supporting the idea that regulatory links between Myo-II and Rho utilized for one morphogenetic process might not be engaged in others.

Second, it is likely that the negative feedback circuit is not simply monitoring the total level of F-actin. Recall that LatB-induced depolymerization set off Rho activation whereas redistribution of F-actin by CytoD did not. This initially indicated to us that the total amount of actin filaments may be the cue for negative feedback. However, MLC depletion caused a 30% reduction of F-actin at aligning interfaces, but this did not affect the polarized recruitment of Dia. While it is possible that more significant depletion is needed to attenuate negative feedback, it is more probable that some aspect of actin organization is the cue for inhibitory regulation and that this organization is unaffected by Myo-II depletion. Indeed, the organization of filaments can determine binding specificity of different actin regulators[109]. Such regulators could interact with RhoGAPs/GEFs in a manner that antagonizes Rho.

Finally, I have presented evidence that ROK facilitates this negative feedback. This must be a Myo-II independent function of ROK, as MLC depletion did not appear to effect Rho activity whereas ROK inhibition upregulated the Rho-GTP sensor. ROK can regulate the actin cytoskeleton through phosphorylation of other targets such as Moesin, which itself can suppress Rho via a RhoGAP[97,105,110,111].

Other factors besides ROK may also participate in negative feedback, and in turn allow for different actin remodeling activities that could affect morphological outcomes. For example, Rho can be antagonized by Rho family members Rac and Cdc42, although the mechanisms underlying this antagonism are not fully elucidated [112]. Dynamic interchange between by Rho and Rac/Cdc42 activation could strike a balance between promoting linear actin and branched actin. This concept will be explored more in Chapter 6.

Novel to this study, our data also suggest that a second tier of negative feedback control over Dia exists and that this feedback might be directly engaged by F-actin. It is logical that F-actin feedback would target the branch of Rho signaling responsible for

filament polymerization to maintain appropriate levels of actin remodeling, particularly since I demonstrate that the formation of ectopic furrows is correlated to an elevation in F-actin levels. However, because the mechanism underlying this reaction remains unclear, establishing further genetic support for this feedback is warranted. Still, I can glean some information from that fact that after CytoD treatment, Dia accumulated at both membrane and in larger foci (Fig. 5.4B). The latter likely corresponds to the aggregates of F-actin observed with drug treatment (Fig. 5.4A). Therefore, I hypothesize that this feedback mechanism suppresses recruitment of Dia to both the cell membrane and to actin filaments. Analysis of transgenic lines expressing forms of Dia deficient in either actin- or membrane-binding would give additional insight into this mechanism.

Additionally, I have demonstrated that ROK has a separate function in positively regulating Dia planar polarity. In mammalian cells, it has been shown that ROK can phosphorylate Dia to activate it directly[113]. It is unknown whether this phosphorylation site is conserved in *Drosophila*, so genetics-based approaches to manipulating putative phosphorylation residues as well as ROK activity would allow us to test this hypothesis further.

Regulation of feedback as a strategy for diversifying morphogenesis

Combinatorial control over feedback could modify signaling outcomes of the Rho pathway. In many contexts where positive feedback on Rho has been demonstrated, the GTPase cycles between activation and inactivation (i.e. activator-inhibitor systems) [45,100–102]. The consequences of this are spatio-temporally dynamic actomyosin assemblies. While the temporal resolution at which I analyzed Rho-GTP and actomyosin at aligning junctions is limited in this report, these enrichments appear to be more stable than that observed in excitable systems. This may be a product of the apparent lack of a positive feedback control over Rho activity coupled to multiple tiers of

negative feedback. This idea would require a more robust sensor for Rho-GTP that would allow analysis of its dynamics at higher temporal resolution.

Negative feedback also appears important for suppression of epithelial invaginations. Additionally, I demonstrated positive feedback between Myo-II and F-actin as well as from ROK to Dia. This positive feedback amongst downstream components in the pathway may allow for amplification of the relatively subtle enhancements of Rho-GTP I have observed in alignment. Additionally, positive feedback may buffer against small fluctuations in Rho activity that may arise from negative feedback[103,114].

Since the Rho is central to numerous morphogenetic programs, further investigation into the factors that dictate feedback regulation will provide insight into the extraordinary versatility of this signaling pathway.

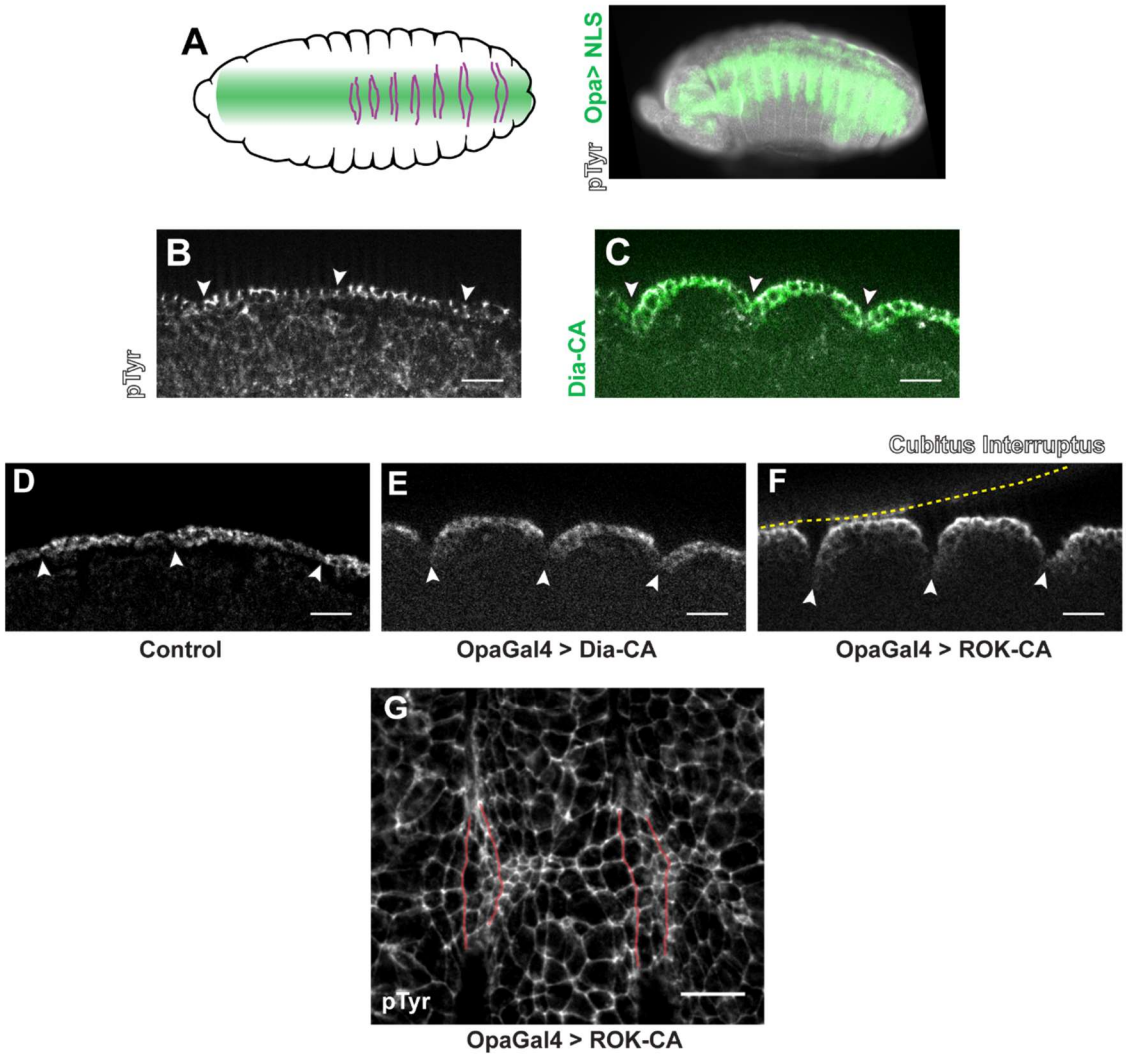

Figure 5.1: Overactivation of Rho signaling causes ectopic furrowing at aligning interfaces

(A) Schematic shows the expression pattern (green) of Opa-GAL4 over the ventral face of the embryonic epithelium. Magenta lines show the aligning interfaces in each abdominal segment. Fluorescent image shows fixed embryo that expresses UAS-NLS::mCherry with Opa-GAL4. With respect to the schematic, the embryo is slightly tilted along the Dorsal-Ventral axis.

(B and C) In (B) wild type embryos, the epithelium is flat within the plane of AJs. (C) Opa-GAL4 > Dia-CA drives invagination only in aligning regions. Arrowheads indicate the location of the anterior aligning interface within each segment. The epithelium is shown in cross-section along the apical-basal axis with apical side on top. WT CTRL: representative of 5 embryos; Eve-GAL4>Dia-CA: representative of 4 embryos.

(Figure 5.1 Continued)

(D-F) Ectopic furrows only form where aligning interfaces would normally form. (D) The boundary of Cubitus Interruptus expression is located at the anterior aligning interface (arrowheads). These regions are flat in wild type embryos. Upon expression of (E) Dia-CA or (F) ROK-CA with Opa-GAL4, ectopic furrows form at the Cubitus Interruptus boundary. Cross sections of the ventral epidermis are shown with the apical surface on top. Above the yellow dashes line, a second, irrelevant embryo lies in the field of view. CTRL: representative of 5 embryos; Dia-CA: representative of 4 embryos; ROK-CA: representative of 5 embryos

(G) ROK-CA expression results in additional cell morphology changes across the epithelium in addition to furrow formation. Red lines mark the aligning interfaces within the ectopic furrows. Representative of 5 embryos

pTyr antibody staining was used to mark AJs in all fluorescent images

Scale bars = 12μm

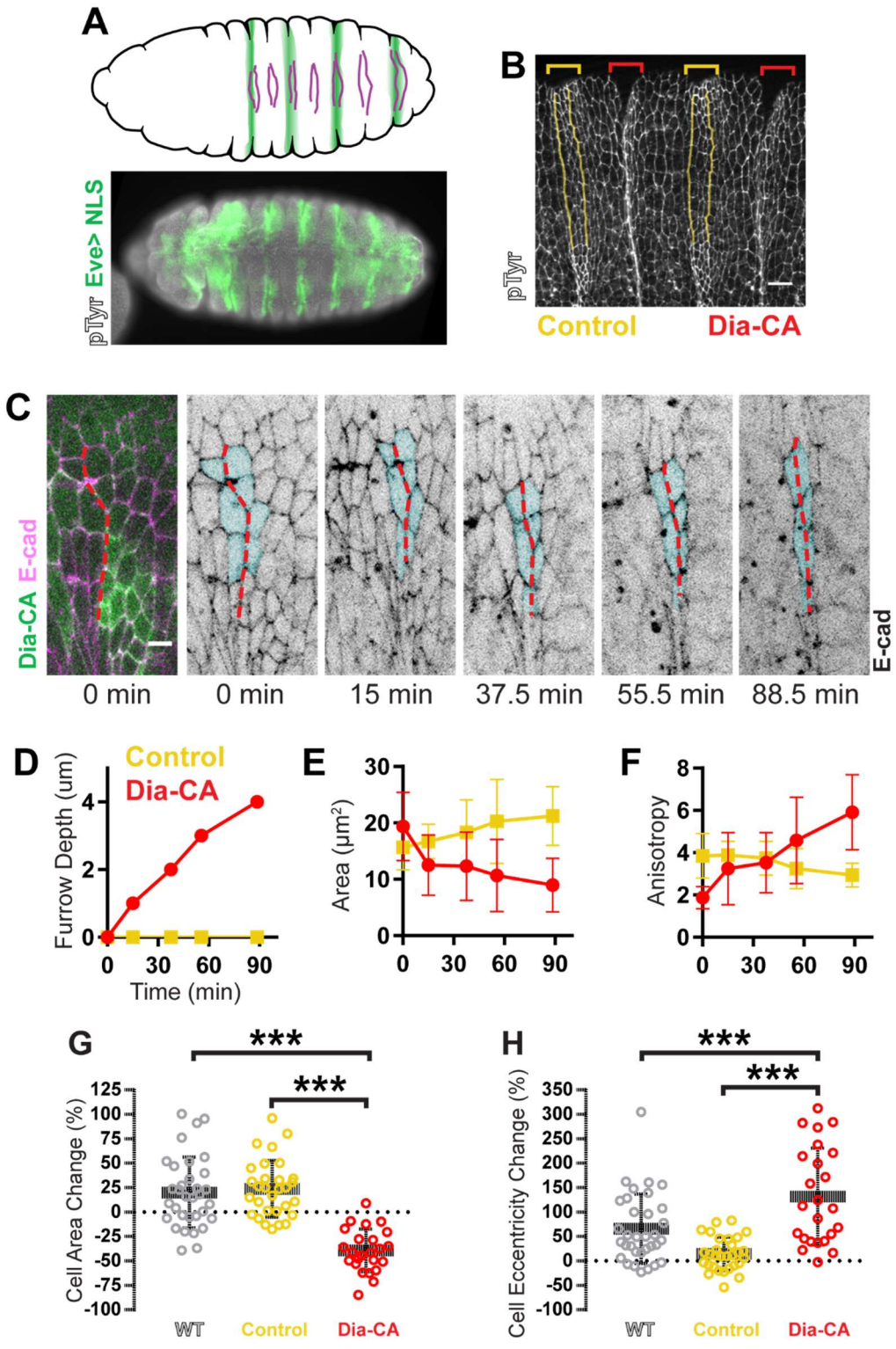

Figure 5.2: Overactivation of Rho signaling changes the morphological outcome from alignment to apical constriction.

(Figure 5.2 Continued)

(A) Schematic shows the expression pattern (green) of Eve-GAL4 in alternating abdominal segments over the ventral face of the embryonic epithelium. Magenta lines show the aligning interfaces in each abdominal segment. Fluorescent image shows a fixed embryo of a similar orientation expressing UAS-NLS::mCherry with Eve-GAL4.

(B) Aligning interfaces invaginate with constitutive activation of Dia. Anterior aligning interfaces in non-expressing, control segments (yellow brackets) are pseudo-colored yellow. In a surface view, the aligning interfaces are no longer detected in Eve-GAL4 > Dia-CA expressing segments (red brackets), as they are located within furrows. Representative of 5 embryos.

(C-F) Anisotropic apical constriction in Eve-GAL4 > Dia-CA expressing cells was observed by live imaging. (C) E-cad::tdTomato marked cell outlines. As the ectopic furrow formed, (D) furrow depth, (E) apical area, and (F) anisotropy were measured for tracked cells (pseudo-colored cyan in e). (E) Area and (F) anisotropy measurements for all the tracked cells were averaged at each time point in the graphs for the same interface: either Dia-CA expressing (red) or a control interface from a non-expressing segment in the same embryo (yellow). We observed identical trends for three other embryos that were analyzed in this manner (not shown).

(G) Cell surface area significantly decreases upon Dia-CA expression (red) compared to adjacent, control interfaces (yellow) or to interfaces in wild type embryos (gray). WT: 33 cells, 4 embryos; Ctrl: 30 cells, 4 embryos; Dia-CA: 24 cells, 4 embryos

(H) Cell eccentricity significantly increases upon Dia-CA expression (red) compared to adjacent, control interfaces (yellow) or to interfaces in wild type embryos (gray). WT: 33 cells, 4 embryos; Ctrl: 30 cells, 4 embryos; Dia-CA: 24 cells, 4 embryos

***$p<0.0001$, The Mann-Whitney U-test. Error bars = S.D. (B) Scale bar = 12μm, (C) Scale bar = 4 μm.

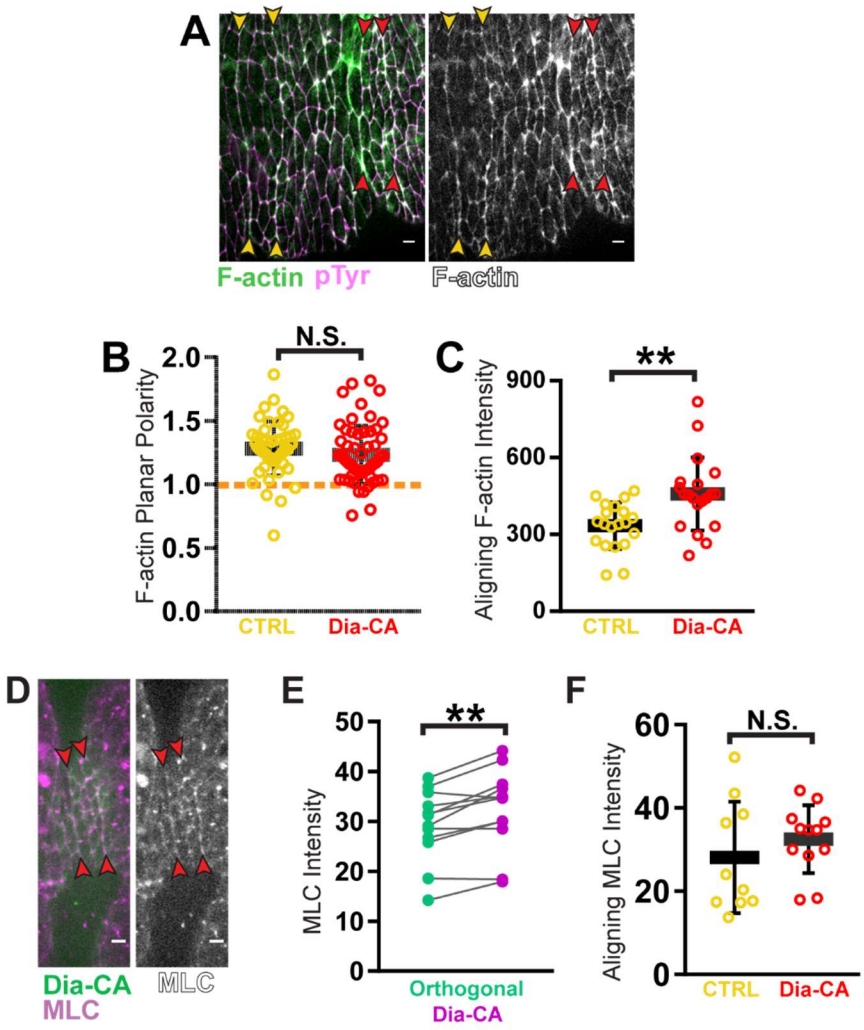

Figure 5.3: Ectopic furrow formation is associated with increased actin polymerization, not Myo-II recruitment

(A-C) F-actin planar polarity was retained, but levels increased by Dia-CA. (A) Dia-CA (green) was expressed with Eve-GAL4. F-actin (green) distribution was detected by Phalloidin staining. pTyr marked cell outlines (magenta). (B) F-actin planar polarity was not significantly different in Dia-CA expressing segments (red arrowheads and data points) compared to control, non-expressing segments (yellow arrowheads and data points). (C) Dia-CA expression caused elevation of F-actin levels along aligning junctions compared to control interfaces. CTRL & Dia-CA: 20 interfaces, 5 embryos

(Figure 5.3 Continued)

(D-F) Dia-CA expression does not enhance or alter the planar polarized distribution of MLC at aligning interfaces. (D) Dia-CA::GFP (green) was expressed with Eve-GAL4 and MLC::mCherry (magenta) was imaged. (E) MLC was still significantly enriched at aligning junctions relative to orthogonal cell-cell contacts. Each line represents one interface and matches orthogonal (green) and aligning (purple) measurements. Orthogonal & Aligning: 12 interfaces, 7 embryos. (F) There was no significant difference in the amount of MLC at aligning junctions in Eve-GAL4 > Dia-CA expressing segments (red) in comparison to control segments (yellow). CTRL: 10 interfaces, 6 embryos; Dia-CA: 12 interfaces, 7 embryos

***$p<0.0001$, **$p<0.01$. (E) The Wilcoxon Rank paired test. (B,C,F) The Mann-Whitney U-test. Error bars = S.D. (A-D) Scale bars = 12μm, (E) Scale bars = 4 μm.

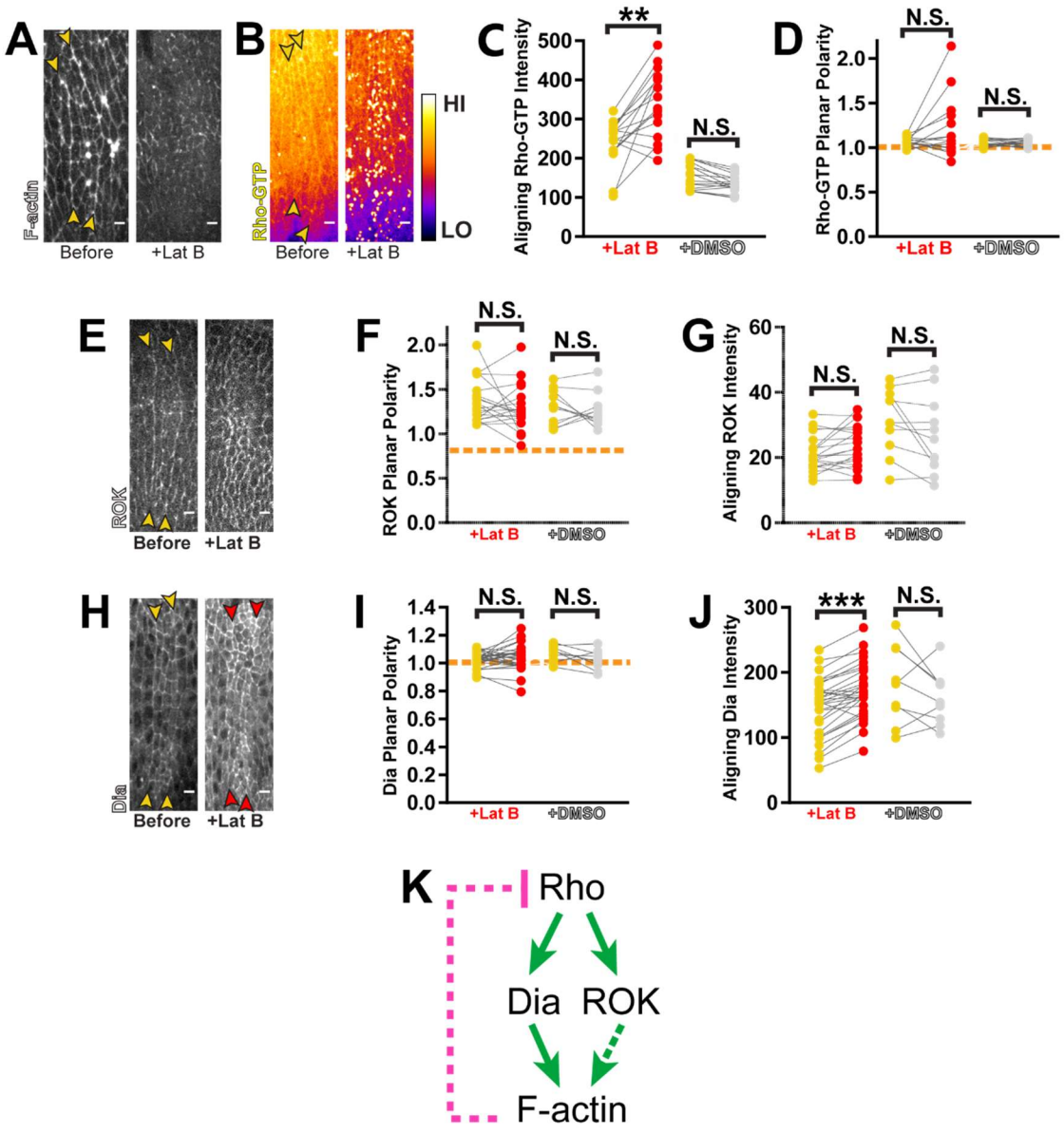

Figure 5.4: F-actin negatively feeds back to Rho.

(A) LatB-induced mass depolymerization of F-actin. Utr-ABD::GFP was used to visualize F-actin. Representative of 4 embryos.

(B-D) LatB treatment reveals negative feedback regulation of Rho-GTP. (B) Rho-GTP was visualized with a GFP-labelled sensor. Fluorescence intensity is displayed with the Fire LUT (calibration bar shows Low to High signal). (C) Rho-GTP levels increased significantly along aligning junctions after LatB treatment, whereas (D) planar polarity was unaffected. LatB: 16 interfaces, 4 embryos; DMSO: 16 interfaces, 4 embryos

(Figure 5.4 Continued)

(E-G). LatB caused defects in ROK distribution along junctions. (A) GFP::ROK^{K116A} appeared more punctate at cell junctions after drug treatment. (B) Planar polarity and (C) the amount of ROK at aligning junctions did not change significantly with LatB treatment. LatB: 20 interfaces, 5 embryos; DMSO: 11 interfaces, 3 embryos

(H-J) Dia recruitment increases upon LatB treatment. (D) Dia::GFP was imaged. (E) The planar polarized distribution of Dia was not affected by LatB exposure. (F) The levels of Dia at aligning interfaces increased with drug treatment. LatB: 30 interfaces, 6 embryos; DMSO: 9 interfaces, 3 embryos

(K) Model of F-actin negative feedback to Rho.

Each line in graphs represents one interface and matches measurements taken before (yellow) and after drug treatment (red) or vehicle treatment (gray).

Control injections with DMSO did not result in significant changes in fluorescence intensity or planar polarity.

***$p<0.0001$, **$p<0.01$, As explained in text, (I, J) the Wilcoxon-Rank test was used to assess statistical significance for changes. For all other experiments, the Mann-Whitney U-test was used. Scale bars = 4μm.

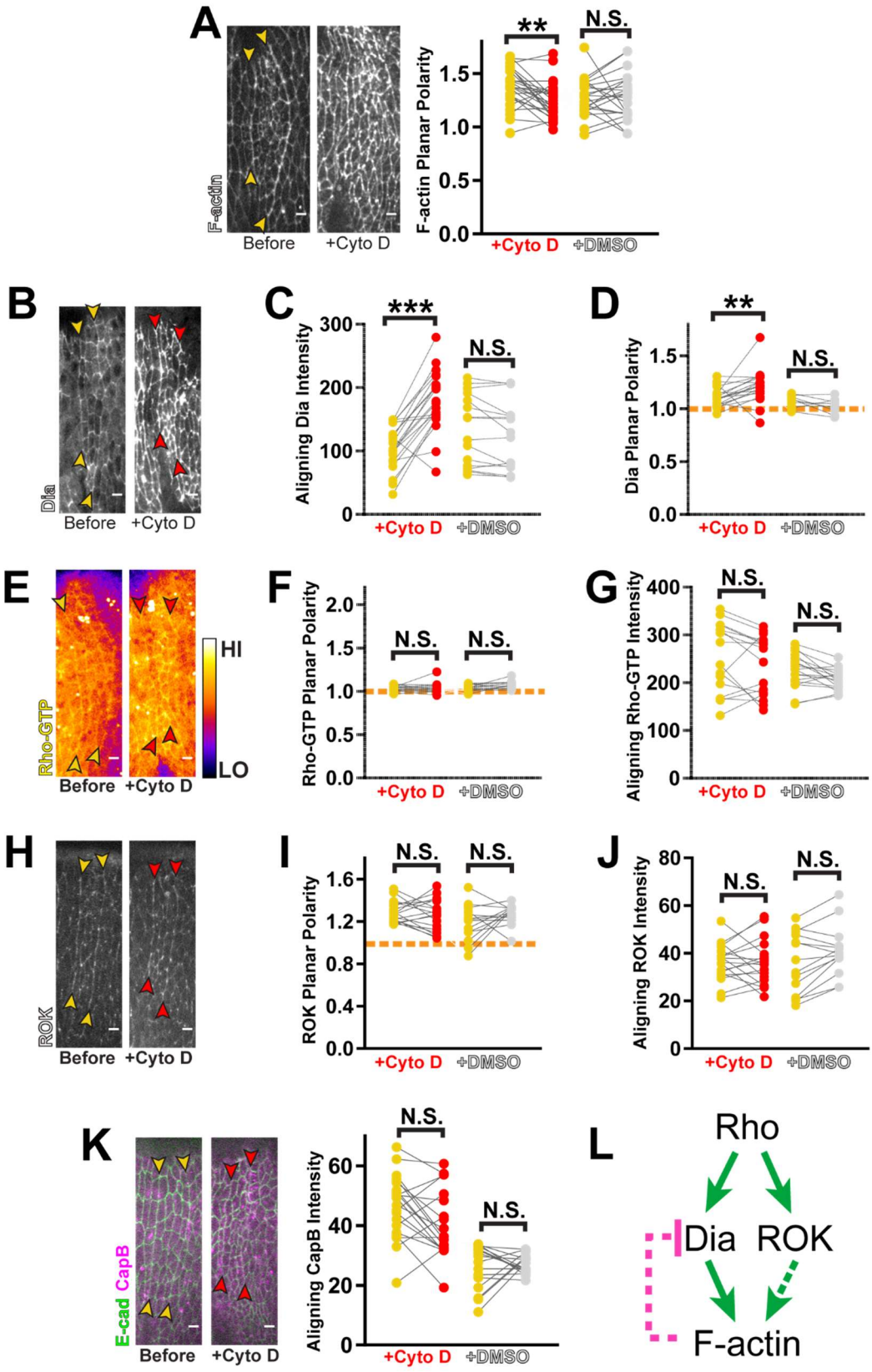
A
F-actin
Before
+Cyto D
F-actin Planar Polarity
**
N.S.
+Cyto D
+DMSO
B
Dia
Before
+Cyto D
C
Aligning Dia Intensity
***
N.S.
D
Dia Planar Polarity
**
N.S.
E
Rho-GTP
HI
LO
Before
+Cyto D
F
Rho-GTP Planar Polarity
N.S.
G
Aligning Rho-GTP Intensity
H
ROK
I
ROK Planar Polarity
J
Aligning ROK Intensity
K
E-cad CapB
Aligning CapB Intensity
L
Rho
Dia
ROK
F-actin

Figure 5.5: F-actin exerts additional feedback on the Dia branch of the Rho pathway.

(A) CytoD had profound effects on F-actin organization, resulting in loss of planar polarity. However, this drug did not induce net depolymerization of cortical F-actin. Utr-ABD::GFP was used to visualize F-actin. Cyto-D: 26 interfaces, 5 embryos; DMSO: 22 interfaces, 7 embryos

(B-D) CytoD treatment reveals negative feedback to Dia. (B) Dia::GFP was used to visualize its distribution. (C) CytoD caused a dramatic increase in total levels at aligning junctions and (D) a slight enhancement of planar polarity. CytoD: 22 interfaces, 4 embryos; DMSO: 22 interfaces, 7 embryos

(E-G) CytoD does not alter Rho-GTP distribution. (G) Rho-GTP is visualized with a GFP-labelled sensor. Fluorescence intensity is displayed with the Fire LUT (calibration bar shows Low to High signal). Neither (H) Rho-GTP planar polarity or (I) levels at aligning junctions changed significantly after CytoD treatment. CytoD: 16 interfaces, 6 embryos; DMSO: 18 interfaces, 5 embryos

(H-J) CytoD does not alter ROK distribution. (J) GFP::ROK^{K116A} was live imaged. Neither ROK planar polarity (K) or levels at aligning junctions (L) changed significantly after CytoD treatment. CytoD: 18 interfaces, 5 embryos; DMSO: 8 interfaces, 3 embryos

(K) CytoD has no effect on CapB cortical levels. CapB::mCherry (magenta) was imaged with E-cad::GFP (green) as a reference for cell junctions. CapB levels at aligning junctions did not change significantly with CytoD injection. CytoD: 20 interfaces, 6 embryos; DMSO: 16 interfaces, 4 embryos

(L) Model of F-actin negative feedback to the Dia branch of Rho signaling.

Each line represents one interfaces and matches measurements before (yellow) and after (red) drug treatment or vehicle treatment (gray).

No significant changes in fluorescence intensity or planar polarity were observed with control injections of 50% DMSO.

***$p<0.0001$, **$p<0.01$, Mann-Whitney U-test. Scale bars = 4μm.

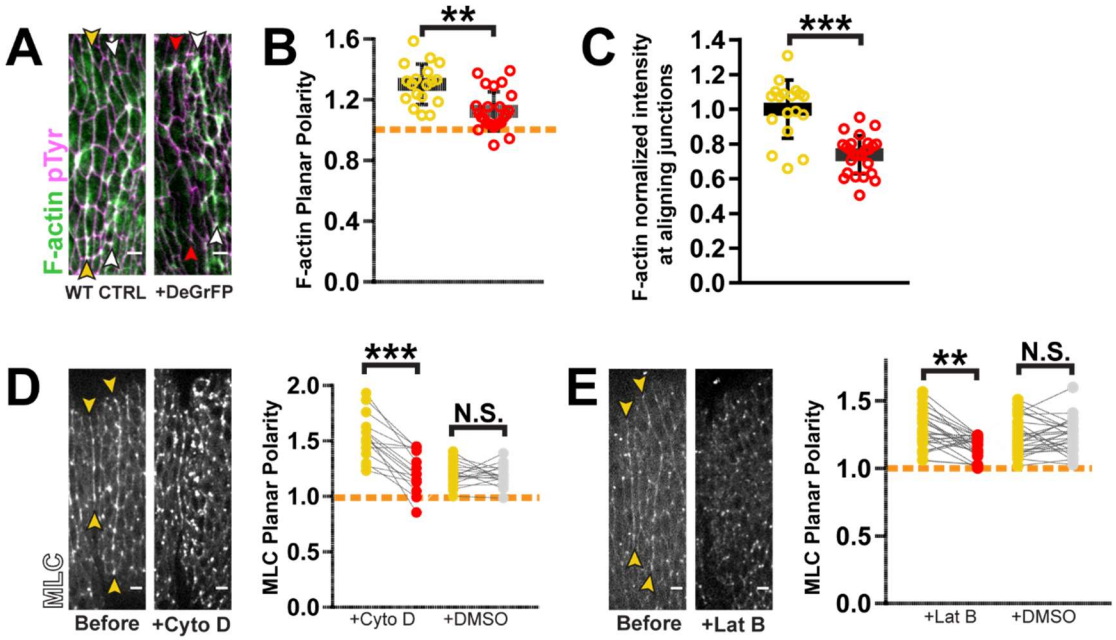

Figure 5.6: F-actin and Myosin positively regulate one another within contractile cables.

(A-C) F-actin was depleted from actomyosin cables upon MLC knockdown. (A) Red arrowheads indicate the interface where MLC was depleted. Knockdown condition was compared to sibling control (WT CTRL, yellow arrowheads). Phalloidin staining was used for F-actin detection. pTyr antibody staining marked cell outlines. (B) F-actin planar polarity was reduced with MLC depletion. (C) F-actin levels at aligning junctions were also decreased with MLC knockdown. To account for variability between samples, the fluorescence of the affected interface was normalized to that of the unaffected, posterior interface (white arrowheads in A). WT CTRL: 18 interfaces, 4 embryos; deGradFP+: 25 interfaces, 5 embryos

(D) MLC::GFP enrichments along aligning interfaces were lost with CytoD treatment. Cyto-D: 16 interfaces, 3 embryos; DMSO: 16 interfaces, 5 embryos

(E) MLC::GFP enrichments along aligning interfaces were lost with LatB treatment. LatB: 25 interfaces, 6 embryos; DMSO: 27 interfaces, 5 embryos

Each line in graphs (D,F) represents one interface and matches measurements taken before (yellow) and after drug treatment (red) or vehicle treatment (gray).

No significant changes in MLC were observed with control injections of DSMO

***p<0.0001, **p<0.001, Mann-Whitney U-test, Error bars = S.D. Scale bars = 4μm.

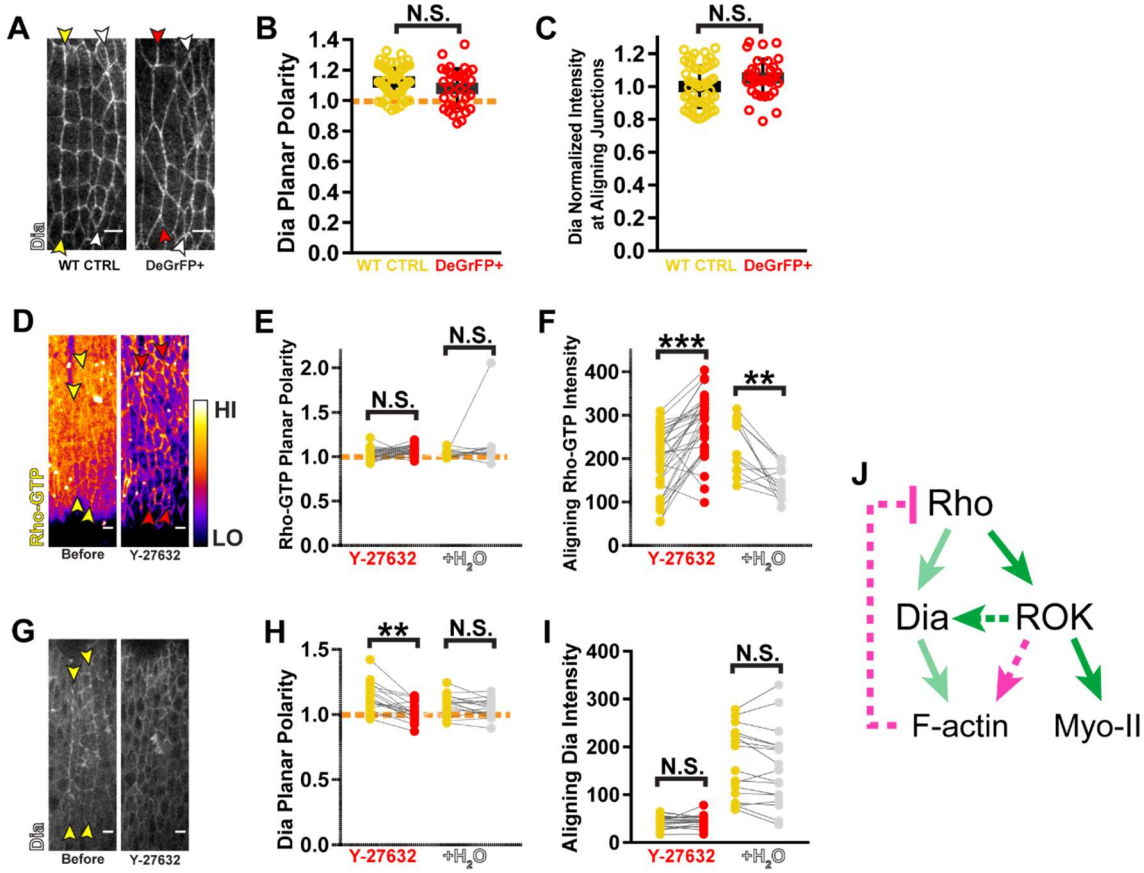

Figure 5.7: Independent of actomyosin contractility, ROK regulates the Rho pathway.

(A-C) MLC and contractility do not feedback to the Rho pathway. (A) Dia was detected by antibody staining. MLC knockdown did not change (B) Dia planar polarity or (C) levels at aligning interfaces. Fluorescence measurements at interfaces with MLC depletion (red) were compared to those of sibling controls (yellow). WT CTRL: 57 interfaces, 11 embryos; DeGradFP+: 34 interfaces, 6 embryos.

(D-F) ROK negatively regulates Rho activation. (D) Rho-GTP is visualized with a GFP-labelled Rho sensor. Yellow arrows mark the aligning interfaces before drug treatment. Fluorescence intensity is displayed with the Fire LUT. (E) Planar polarity of Rho-GTP was not affected by this treatment, but (F) the total amount at aligning junctions increased significantly. Y-27632: 34 interfaces, 7 embryos; H_2O: 15 interfaces, 4 embryos

(G-I) ROK positively regulates Dia planar polarity. (G) Dia::GFP distribution is altered with ROK inhibition. (H) Planar polarity of Dia is decreased significantly with ROK inhibition. (I) Drug treatment did not significantly decrease Dia levels at aligning interfaces. Y-27632: 18 interfaces, 4 embryos; H_2O: 17 interfaces, 4 embryos

(J) Schematic for model of ROK-mediated negative feedback through F-actin.

(Figure 5.7 Continued)

For graphs (D-I), each line represents one interface and matches measurements taken before drug exposure (yellow) and after Y-27632 injection (red) or vehicle treatment. Rho-GTP levels were found to significantly decrease with control water injection. This likely reflects photobleaching during the course of the experiment. However, given that Y-27632 resulted in the opposite change (increase in Rho-GTP levels), the change in signal from control injection does not impact the conclusions made from the experiment. In all other instances, control water injection did not significantly alter fluorescence intensity or planar polarity.

***p<0.0001, **p<0.01, Mann-Whitney U-test, Error bars = S.D. Scale bars = 4μm.

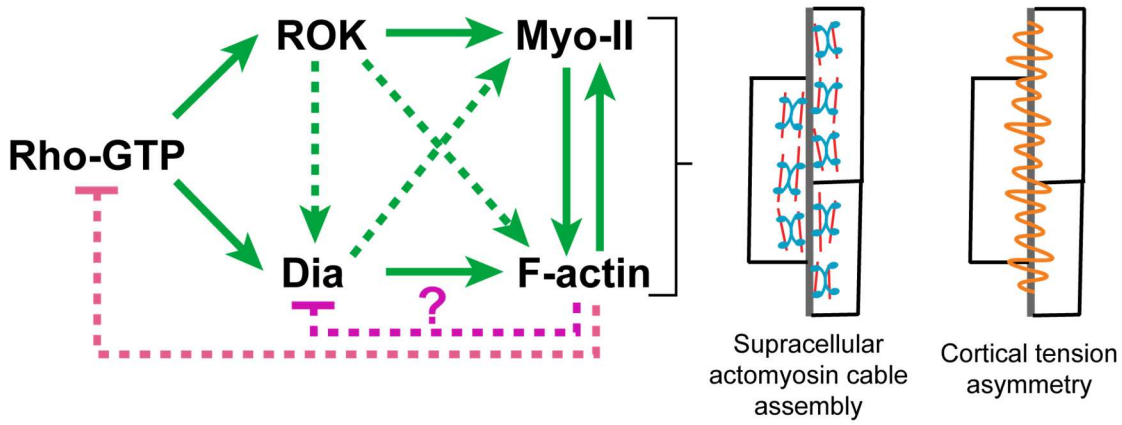

Figure 5.8: Model of Rho pathway interactions that mediate polarization of actomyosin assembly and cortical tension during alignment.

Green lines indicate positive regulation while pink/magenta lines indicate inhibitory interactions. Solid lines indicate direct interactions. Dashed lines signify interactions that may be direct or indirect.

CHAPTER 6: A potential role for Rac-Arp2/3 signaling in alignment

Introduction

My findings in Chapter 3-5 elucidate important fundamentals on the mechanical and signaling basis of alignment, as well as the importance of moderating Rho signaling. However, they do not address the question of how cell junctions in aligning interfaces are able to elongate while under contractile force. Even with constitutive activation of Rho effectors, aligning cells undergoing furrowing still lengthen along the dorsal-ventral axis, the direction along which cortical tension would be upregulated (Fig. 5.1). Therefore, there are still large gaps in our knowledge of the mechanical basis of alignment.

One reasonable hypothesis is that there is an actin remodeling activity yet to be discovered that explains the unique morphogenetic job these cables perform. A strong candidate is Arp2/3-mediated actin polymerization, which results in a branched arrangement of actin filaments[14,56,115]. Branched actin has been shown to support junction lengthening in different systems[59,60]. This organization of actin is thought to produce pushing or compression forces at cell junctions [59,60]. Applied in the direction orthogonal to the junction, these forces would strengthen cell adhesions in order to promote junction lengthening[59,60]. In further support that this may be deployed during alignment, Arp2/3 activity is repressed during convergent extension where junctions that are under tension shrink dramatically[30].

In this chapter, I present preliminary lines of evidence that Arp2/3 activity contributes to actin within supracellular cables, and that this is significant to the mechanical properties of these structures. Additionally, at aligning interfaces, I have detected the presence of a bipartite RacGEF, Mbc/Elmo, and observed alignment defects upon knockdown of one of its components. This suggests that the Rho relative, Rac, is responsible for regulating this branched actin pool.

If both contractile and compression forces are deployed during alignment, there are likely mechanisms that precisely coordinate their activities. Indeed, it is known that Rho and Rac participate in both negative and positive crosstalk with one another[112]. These interactions are reported to occur at different levels within the pathways and primarily act upon the regulating GEFs and GAPs (Fig. 6.4A) [112]. One potential mechanism for simultaneously regulating different GTPases is the coupling of GEFs and GAPs. Mbc/Elmo has been proposed to be coupled to RhoGAP19D in order to mediate rapid shifts in activity from Rho to Rac [115]. I have found that this RhoGAP19D is indeed present at cell junctions during alignment, suggesting that potential cooperation between these small GTPase regulators could be significant to alignment.

Results

Dynamic F-actin protrusions found at actomyosin cables indicate Arp2/3 activity

By imaging actomyosin cables at a high temporal resolution, I found that the distribution of F-actin was dynamic and heterogeneous along the length of aligning interfaces. Specifically, protrusions extend and retract from cables at varying rates (Fig. 6.1A blue, yellow and pink arrowheads, Movie 6). Some protrusions were thinner and more filopodia-like in morphology (Fig. 6.1C-D orange, Movie 6). This observation is not particularly surprising given that Dia does participate in building the actin in filopodia[85,116,117]. Other protrusions were wider and appeared more like ruffles, indicating that they may be similar to lamellipodia molecularly (Fig. 6.1B-C green, Movie 6) [14,116]. Arp2/3-mediated branched actin is the major structural component of lamellipodia. Therefore, it appears that the filament organization within actomyosin cables may be complex and contain both branched and linear filament arrangements.

It should be noted that there is no obvious increase in the frequency of lamellipodia along aligning junctions relative to junctions in the rest of the tissue.

However, careful quantification of these protrusions would be required to rigorously conclude one way or the other.

Localization of branched-actin associated proteins suggest a requirement for Arp2/3 activity

While I was not able to achieve the imaging resolution necessary to discern the filament organization within these protrusions, I imaged multiple factors that are known to be associated with branched actin networks. First, I looked at the distribution of key NPFs, WASp and the WAVE complex. An endogenously GFP-tagged version of WASp appeared to be enriched to aligning interfaces relative to junctions in the rest of the tissue (Fig. 6.2A). Two components of the WAVE complex, Scar and Abi, were also found at aligning junctions (Fig. 6.2B, C). Quantification would be needed to determine whether there is a significant enrichment of any of these three factors along aligning junctions.

I then examined the distribution of phosphatidylinositol (3,4,5)-trisphosphate (PIP3), which is a phosphoinositide known to assist in the activation of both WASp and Rac[118,119]. To image the distribution of this lipid, I used a plekstrin-homology domain specific to PIP3 fused to GFP[120]. This sensor was enhanced significantly along aligning interfaces (Fig. 6.2D, G).

Fimbrin is a small actin crosslinker that is preferentially recruited to branched actin networks[109,121]. An endogenously GFP-tagged version of fimbrin was polarized to aligning junctions (Fig. 6.2E).

Lastly, I examined the distribution of the cofilin binding partner, AIP-1[122]. The depolymerization activity of cofilin is essential to the propagation of branched actin networks[116,122]. AIP-1 was enriched along aligning interfaces, revealing another

piece of evidence pointing towards the presence of branched actin within supracellular actomyosin cables (Fig. 6.2F).

At the present time, the above observations are qualitative in nature, and thus, should be quantified in future work. However, collectively they strongly suggest that actomyosin cables are composed of heterogeneous populations of actin, some of which arise from the activity of Arp2/3.

The Elmo/MBC complex is required for alignment

Given the potential presence of Arp2/3, this raises the question of what small GTPase is involved with its activation. It is challenging to inhibit Rac or Cdc42 during alignment to test their role directly. Instead, I sought to test the function of specific GEFs that might activate these small GTPases. I analyzed alignment in embryos homozygous for a null allele of *mbc*, which encodes a component of a bipartite RacGEF. mbc^{C1} embryos had significant alignment defects compared to wild-type embryos (Fig. 6.3B). It is important to note here that the control group measurements I report for this preliminary experiment are not from sibling embryos. This was because sibling embryos, many of which are heterozygous for mbc^{C1}, also appeared to have alignment defects (data not shown). This is likely due to partial maternal and zygotic depletion of Mbc, as I observed in a similar experimental set up with the *dia* null allele (Chapter 4, Fig. 4.2A-D). Thus, mbc^{C1} analysis will need to be repeated so that the homozygous mutant embryos can be compared to a proper control group. In such cases, it would also be best to blind the samples prior to alignment analysis.

Nevertheless, the suggestion that Mbc is required for alignment led me to examine the distribution of its binding partner, Elmo. Qualitatively, enrichment of Elmo was found along aligning junctions (Fig. 6.3A). This preliminary result is indicative of a function for the Mbc/Elmo complex and Rac.

Mbc/Elmo has been shown to coordinate the balance of Rho/Rac activity via cooperation with a RhoGAP, namely RhoGAP19D[115]. Imaging an endogenously GFP-tagged version of RhoGAP19D, I found that this GAP was localized to cell junctions during the time that alignment takes place. Qualitatively, it does not appear to be enriched at aligning interfaces. Note that I am analyzing total RhoGAP19D protein, which may not reveal where active RhoGAP is accumulating. I have imaged other RhoGAPs, one of which has been implicated in feedback between F-actin and Rho, RhoGAP17E[101,102]. The signal of an endogenously GFP-tagged version of RhoGAP17E was extremely dim in embryos and mostly localized to the cytoplasm (data not shown). Therefore, RhoGAP19D is currently the strongest candidate for regulating Rho activity during alignment.

Discussion

Potential functions for Mbc/Elmo-Rac-Arp2/3 during alignment

Rac-Arp2/3-mediated actin remodeling may serve two different functions during alignment. First, it may modulate that mechanical properties of actomyosin cables, allowing for the lengthening of junctions that are under contractile force (Fig. 6-4A). Second, it may suggest a role for crosstalk between small GTPase signaling pathways as a mechanism for moderating Rho activity (Fig. 6-4A, B). Indeed, it may be the missing link between F-actin and Rho in terms of the negative feedback proposed in Chapter 5.

Mechanical coordination between branched and linear actin

As suggested before, branched actin may exert pushing forces onto junctions in order to allow for their elongation during alignment[59,60]. More robust methods of

depleting Rac, Arp2/3 and other branched actin associated proteins will be needed in order to thoroughly dissect their mechanical contribution to alignment. Additionally, their activity likely needs to be tightly balanced with the contractility of linear assemblies in order to achieve the proper, final cell geometry.

So-called supracellular cables perform different types of morphogenetic tasks[15,16,19,33,123]. The filamentous organization of actin in these structures has not been investigated at all due to lack of spatial resolution. Their structure has been presumed to be linear due to the requirement for Rho signaling in many cases as well as the resemblance of cables to stress fibers. However, filament architecture may be quite different comparing cables that act in different morphogenetic contexts. There might even be heterogeneity within a single cable. I hypothesize that the ratio of branched actin to linear actin may explain the diversity of outcomes from cable activity (Fig. 6.4B). For example, the cables that participate in convergent extension function under conditions where Arp2/3 is repressed[30]. Therefore, it seems likely that these structures are predominantly composed of linear actin that can produce primarily contractile force (Fig. 6.4B). In alignment, it may be that there exists an equal balance between branched actin and linear actin, leading to a duality in mechanical properties (Fig. 6.4B). My preliminary evidence suggest that this may be the result of precise regulation of Rac and Rho pathways (expanded upon below).

Potential roles for Mbc/Elmo in alignment

Mbc and Elmo can bind together to form a critical RacGEF that most notably functions during myoblast fusion[124,125]. Further investigation of the function of Mbc in alignment is a key step in assessing the role of the Rac pathway during alignment, as well as being informative as to the contribution of Arp2/3. The requirement for Elmo can also be tested with zygotic mutants that are currently available[115,126]. It will also be

important to characterize both the cell and actin morphology dynamics with live imaging after Mbc/Elmo depletion.

It is worth noting that junction elongation did not appear to be disrupted in *mbc*^{C1} mutants, although this was not quantified. This would seem to contradict my hypothesis that Arp2/3-mediated activity may be required for the lengthening of junctions during alignment. If indeed junctions can elongate without Mbc, there are a few possible explanations. First, junction elongation may not be the function of Arp2/3 in alignment. Second, Rac may activate an array of factors, with Arp2/3 being just one. Different RacGEFs may promote different branches of Rac signaling. Thus, Mbc/Elmo may not necessarily be involved in activating the Arp2/3 module of Rac. It is also possible that Cdc42 is sufficient to activate Arp2/3 in this context, and that Mbc depletion reveals some other, significant function of Rac. These possibilities highlight the importance of testing the function of Rac, Cdc42, Arp2/3 and putative RacGEFs during alignment separately.

Both Mbc and Elmo can form complexes with other proteins to act as RacGEFs with distinct functions. Mbc complexes with the protein Crk, forming a RacGEF that is essential for adult thorax development[127]. When bound to the protein Sponge, Elmo functions as a different RacGEF that has a role in CNS development and epithelial morphogenesis in the early embryo [126,128]. It is possible that multiple RacGEFs are deployed and function non-redundantly in the same process. In addition to verifying the requirement for Mbc in alignment, the function of Crk, Sponge and Elmo in alignment should be pursued.

Crosstalk between Rac and Rho signaling

Crosstalk between Rac and Rho could allow for coordinating the balance between branched and linear actin polymerization (Fig. 6.4A, B). Negative and positive crosstalk is known to occur at many levels within each of these pathways (Fig. 6.4A).

GAPs and GEFs that regulate different small GTPases can directly and indirectly cooperate with one another[112]. It has also been proposed that GAPs and GEFs are physically coupled in complexes in order to act as molecular switches[129,130] (Fig. 6.4A). For example, the complexing of a RacGEF with a RhoGAP can rapidly shift activity from Rho to Rac. Unique combinations of GEFs and GAPs that complex with other regulating proteins can allow for many different types of switches that fulfill diverse functions. So far, I have found that many of the RhoGEFs and GAPs implicated in Rho pathway feedback in other systems are either not expressed in the embryo during alignment, do not exhibit defects when depleted (data not shown), or do not have clear homologs in *Drosophila* [42,101,102]. This suggests to me that exploring this direction further could reveal unique Rho regulators and potentially novel complexes with RacGEFs.

Although not mechanistically understood, Mbc/Elmo coordinates with RhoGAP19D to simultaneously downregulate Rho and upregulate Rac activity (Fig. 6.4B) [115]. However, it is worth noting that there was no obvious furrow phenotype in mbc^{C1} mutants, which we would anticipate if Mbc is involved with antagonizing the Rho pathway. This observation needs to be verified, but even if confirmed, it does not exclude the possibility that other RacGEFs are involved with mediating crosstalk with Rho. This would mean that Mbc/Elmo serves a separate function in regulating Rac-Arp2/3.

It makes sense that there would be both positive and negative regulatory interaction between small GTPases, as only inhibitory feedback could lead to the extinguishment of all signaling activity. Rho is known to reciprocally feedback both

positively and negatively to Rac via the Mbc/Crk RacGEF. Dia can activate Mbc/Crk whereas ROK represses it [131]. These are interactions have been described in mammalian cell culture, so whether they occur in *Drosophila* needs to be address. This could be tested simply using the ROK and SMIFH2 (formin) drug inhibitors.

One of the more interesting findings from Chapter 6 is that F-actin negatively feeds back to Rho and Dia activity. Given its known ability to antagonize Rho, Rac mediated Arp2/3-activity may be the missing link in the feedback circuit from F-actin to Rho activation (Fig. 6.4A). Of many possibilities, two hypotheses match the observations thus far. First, branched F-actin directly or indirectly may recruit a RhoGAP to inhibit Rho activation. Second, branched actin may upregulate Rac/Cdc42 through recruitment of a corresponding GEF, and consequentially initiate antagonistic feedback to the Rho pathway. These hypotheses are not mutually exclusive, and I anticipate a number of mechanisms are in place to tightly regulate Rho activity.

Many morphogenetic processes require both linear and branched actin, as well as multiple Rho family members[35,37]. Therefore, further study of the mechanisms of that coordinate multiple Rho Family members would be broadly applicable.

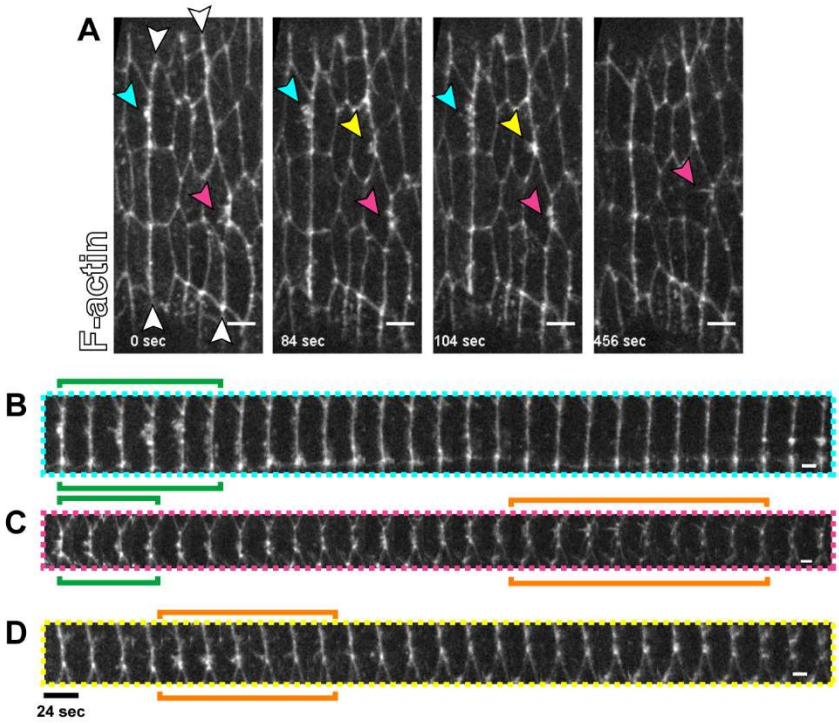

Figure 6.1: Dynamic protrusions indicate potential Arp2/3 activity in actomyosin cables

(A) Dynamic F-actin protrusions emanate from actomyosin cables. Arrowheads point to regions in the montage where a protrusion is either in the process of extending or retracting.

(B-C) Higher magnification montages of junctions in aligning interfaces showing the extension and retraction of F-actin protrusions. Dashed line box colors correspond to the arrowheads in (A). Green brackets indicate frames where protrusions resemble lamellipodia while orange brackets mark timepoints where protrusions are filopodia-like. Each frame is separated by a 24 second interval.

Utr-ABD::GFP was used to visualized F-actin.

Scale bars in (A) = 4μm. All others are 2μm.

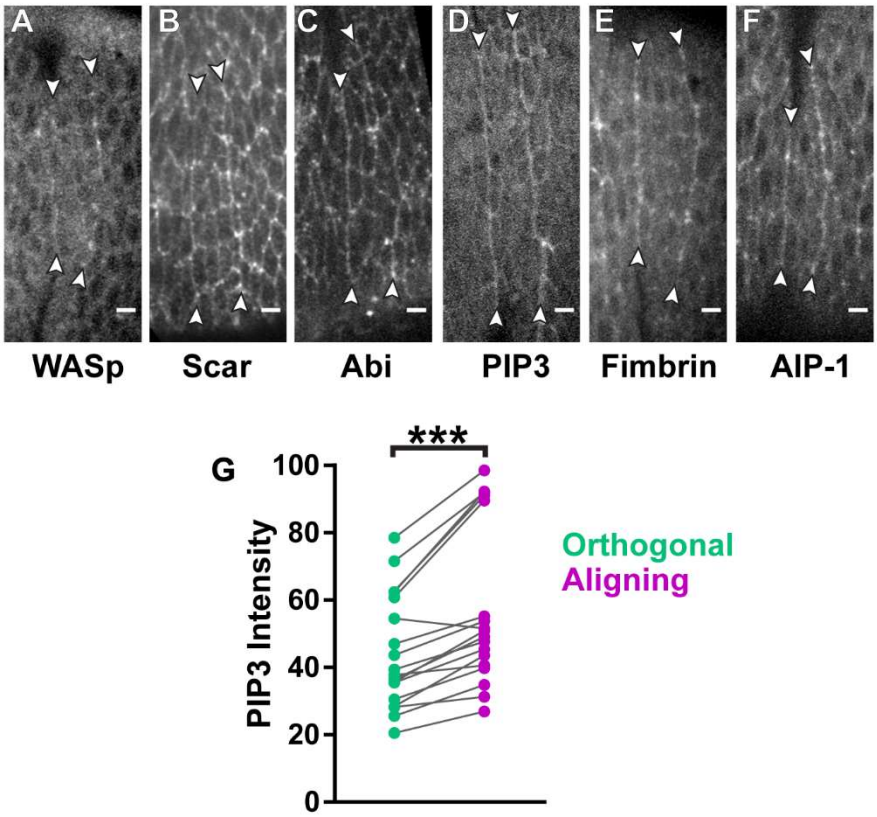

Figure 6.2: Arp2/3 associated factors are localized to aligning junctions

(A-C) Arp2/3 activating proteins are recruited to aligning interfaces. (A) WASp and (B) WAVE complex member Scar appear to be enriched along aligning junctions. (C) Another component of the WAVE complex, Abi, is also found along aligning interfaces. (A) Endogenously tagged WASp::GFP was imaged. Representative of 4 embryos (B) Antibody stain was used to detect Scar. Representative of 3 Embryos(C) Ubiquitously expressed Abi::mCherry was visualized. Representative of 4 Embryos

(D, G) PIP3, a phosphoinositide associated with activating WASp, is significantly enriched along aligning junctions (purple) relative to orthogonal junctions (green). (D) A Plekstrin Homology domain fused to GFP was used as a sensor for PIP3. (G) Each line represents a single interface, matching aligning and orthogonal junction measurements. N = 18 interfaces, 5 embryos

(E) Fimbrin, a cross-linking protein associated with branched actin networks, appears enriched along aligning junctions. Endogenously-tagged Fimbrin was imaged. Representative of 6 embryos

(F) Coffilin activity, a necessary depolymerizing factor in dynamic lamellopodia, may be enhanced along aligning junctions. Endogenously tagged AIP-1::GFP, a binding partner with Coffilin, appears enriched along aligning junctions. Representative of 5 embryos

***p<0.0001, Wilcoxon Rank paired test. Scale bars = 4μm.

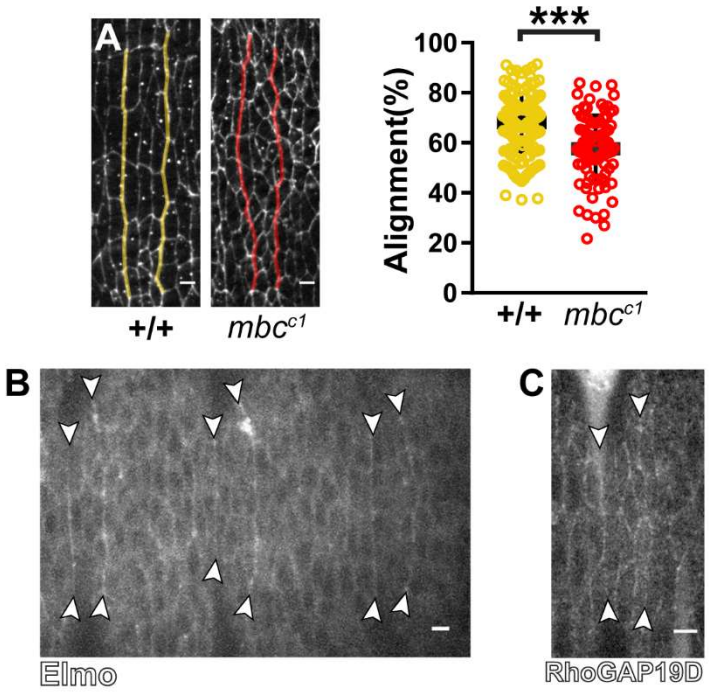

Figure 6.3: The Mbc/Elmo complex may function in alignment

(A) Mbc may be required for alignment. *mbc*^{c1} mutant embryos have significant alignment defects compared to wild type embryos. These sample groups are not sibling embryos. CTRL: 157 interfaces, 13 embryos; *mbc*^{c1}: 89 interfaces, 7 embryos

(B) Mbc binding partner, Elmo, is enriched along aligning junctions. Endogenously tagged Elmo::GFP was imaged.

(C) Endogenously tagged RhoGAP19D is cortically targeted during alignment.

***p<0.0001, Mann-Whitney U-test, Error bars = S.D. Scale bars = 4μm.

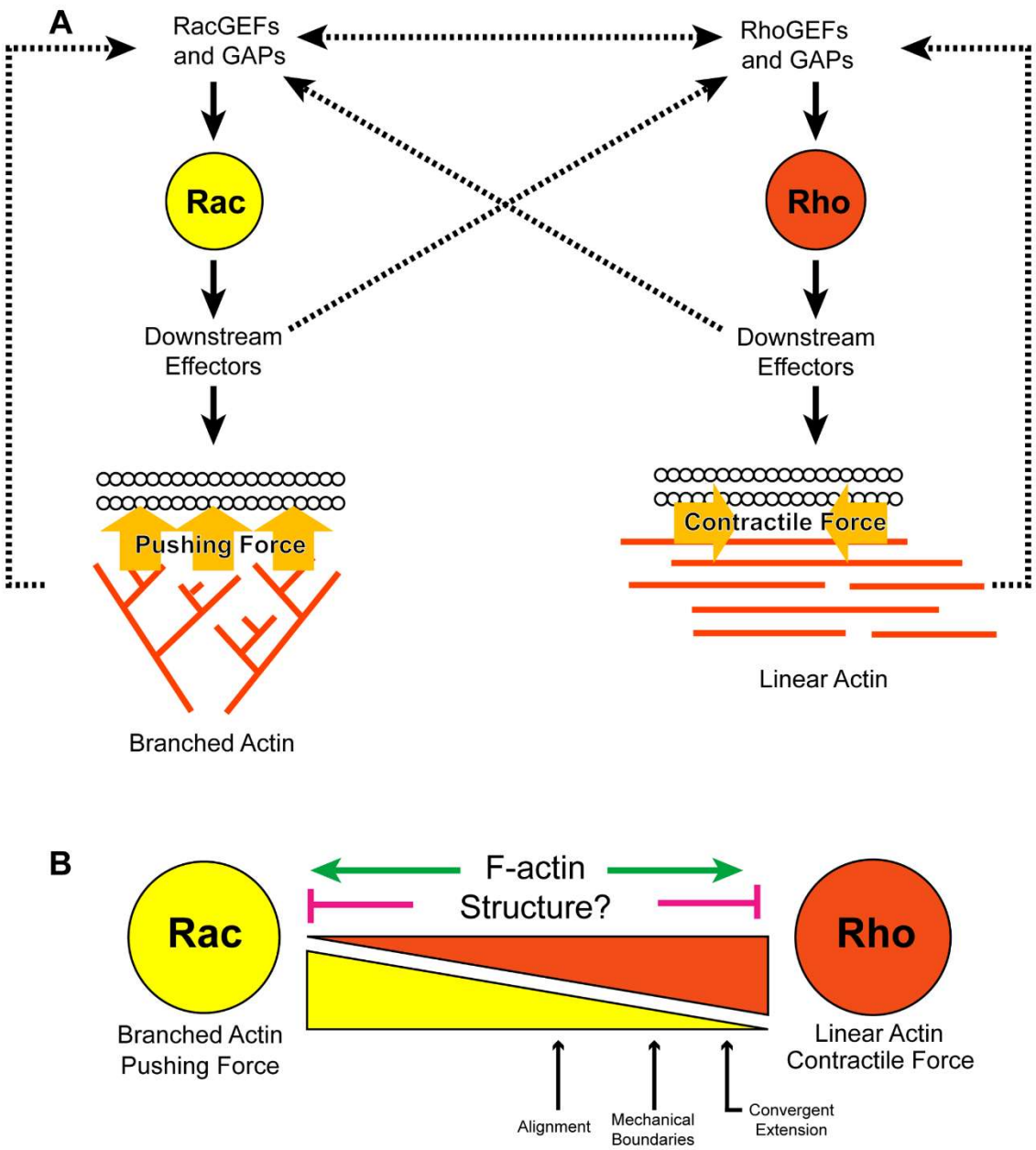

Figure 6.4: Crosstalk between small GTPase pathways may allow for modification of morphogenesis

(A) Schematic model of how F-actin remodeling may fit into the cross-talk between Rac and Rho, and how this would regulate F-actin architecture and actomyosin mechanical properties.

(B) Schematic of hypothesis that balance of Rho and Rac activities may influence morphogenetic outcomes. F-actin structure may mediate positive and negative crosstalk between Rho and Rac in order to strike the correct balance.

CHAPTER 7: Future Directions

Broader impacts on morphogenesis

The orchestration of complex morphological changes necessitates robust, adaptable and tightly-regulated signaling networks. Yet, investigations into morphogenesis in various contexts have identified the same pathways and players over and over again. The basic functions of these factors have been elucidated repeatedly in these different situations, but very little has been revealed in terms of how their activity is modulated to suit their function in each situation.

As described in the introduction, the activity of actomyosin cables contributes to diverse forms in tissues (Fig. 1.2). For example, their activity yields very different end morphologies during wound healing (Fig. 1.2A) vs. neural tube formation (1.2B) vs. tubulogenesis (Fig. 1.2C). Such disparate outcomes may reflect versatility in terms of the mechanical properties of these actomyosin cables. I have shown in Chapter 3 that the cables can produce contractile force during alignment but cease to do so at a later point in development. This suggests that cables can produce different forces tailored to the morphological context in which they function. The mechanical properties of these cables may change dynamically over the time course of a morphogenetic process or may be heterogeneous along the length of the cable, contributing to the intricacy of actomyosin cable function. My examination of the forces actomyosin cables produce during alignment provides significant insight into how such forces may apply to more complex morphogenetic movements as well as to mammalian tissue morphogenesis.

Underlying the mechanical versatility of these actomyosin structures are likely modifications in actin remodeling and upstream signals. My thesis work suggests a variety of mechanisms that could regulate these inputs. First, the amount of linear vs branched actin synthesis may be a determining factor for morphological outcomes (Fig. 6.4). Second, the deployment of different small GTPases may be key to properly balancing the activity of different actin polymerization factors (Fig. 6.4). Finally,

feedback within individual pathways as well as crosstalk between pathways may play a role in moderating GTPase signaling levels (Chapter 5 and 6). At its core, my thesis work provides a nascent understanding of mechanisms that could explain the diverse utility of small GTPase signaling and the actin cytoskeleton, molecular themes that are broadly conserved.

Different morphogenetic changes have important roles in human physiology. Even small errors in wound healing or in the development of tissue form can have dire consequences for human health. Ultimately, my work affords key insight into how fine-tuning at molecular and cellular scales can impact morphogenesis on the macro scale.

Achieving further insight into the cell mechanics of alignment

In Chapter 3, I found that bilateral contractile force is needed to produce the aligned geometry. It is unclear whether this is due to a minimum threshold of force that needs to be reached for alignment to occur, and that this threshold is high enough that two columns of cell must provide contractile force to reach it. Another possibility is that contractile forces along the interfaces must be precisely balanced in terms of the direction that they are applied to the junction. Indeed, shear forces can be applied to a junction from neighboring junctions within the same cell, and these forces have been shown to influence junction morphology and stability (Fig. 1.1C) [11]. There are two key limitations to further testing either of these hypotheses. First, there needs to be experimental approaches that allow for subcellular manipulation of actin, myosin and Rho pathway activity. Second, we need more informative methods of measuring forces in live tissues.

Light induced protein recruitment, or optogenetics, is an emerging technology that may provide more precise spatio-temporal control over activation or inhibition of

actomyosin. In brief, this technology uses protein domains that are photosensitive and activated by exposure to a specific wavelength of light. Once active, it can bind another domain that can be functionalized to a lipid group or other moiety that targets its location in the cell. RhoGEFs and phosphoinositide phosphatases have been fused to the photosensitive domain in order to optogenetically control Myo-II contractility[132–134]. An inhibitor of Myo-II activity or any other target could be theoretically attached to the photosensitive domain to optogenetically control inactivation of the target. At the moment, these methods work best when activating an area enclosing multiple cells[132,135]. Therefore, these methods require improvement in terms of spatial resolution before we are able to manipulate contractility along individual junctions.

Laser ablation has a number of limitations with respect to measuring forces within living cells. Among its limitations, ablation requires destruction of a junction, including the membrane and underlying cortical cytoskeleton. Therefore, measurements cannot be repeated over time for the same junction, as one would during a time course. Additionally, measurements of neighboring cells within the tissue are likely to be influenced by the creation of a wound within the epithelium. This prohibits us from seeing what the forces are along each junction within the same interface. The best I have been able to do is take measurements of individual junctions in separate embryos. This approach does not capture possible temporal and spatial variability that may be relevant to the mechanics of alignment. Furthermore, laser ablation only measures contractile forces along the axis of the cell-contact (Fig. 1.1C left). They cannot detect shear forces (Fig. 1.1C right).

FRET-based sensors for tensile force have started to emerge in the past decade[136,137]. These sensors have been inserted into E-cadherin for detection of forces across cell-cell junctional complexes[137,138]. However, the reproducibility of measurements made with these sensors in *Drosophila* has been challenged[139]. My

early attempts at using such a construct yielded very weak signals that were not able to be calibrated and quantified (data not shown).

Newer, vinculin-based sensors bypass the signal issues associated with FRET[11,140]. This sensor functions off of the principle that alpha-catenin undergoes conformational changes when the cadherin complex is under force, revealing the vinculin binding domain[140]. Vinculin binding and recruitment to the membrane is then used as a way to measure contractile and shear forces applied to the junction[11]. This approach has been shown to resolve the spatial distribution of force across even a single junction[11]. Also advantageous is the fact that Vinculin mostly is dispensable in *Drosophila*, meaning that the protein can be modified significantly to optimize sensor function[141].

This Vinculin-based approach primarily addresses contractile-based forces. It cannot directly measure potential compression forces produced by Arp2/3 activity, cellular rigidity and viscosity, or adhesive forces. All of these potential variables may be important for understanding the function of Arp2/3. Additionally, these other mechanical factors may play a role into how the aligned geometry is stabilized independently of actomyosin contractility. Acquiring these measurements of these properties in the embryo is difficult because it is enclosed in the vitelline membrane during imaging, which prevents the use of Atomic Force Microscopy. Advances have been made in inferring forces in cells with mathematical modeling. In brief, these approaches use assessments of cell shape and modeling to infer the mechanical forces acting upon those cells[142]. However, this approach depends on the assumptions that are tied into the model being correct. Regardless, it would be interesting to see whether such an approach could predict the depletion of contractile force observed in late vs early embryos based on cell geometry alone. Such a test would be insightful into whether this technology holds promise for investigating the mechanics of alignment further.

Higher order polarity signals of alignment

While I have identified a key role for Rho signaling in orienting actomyosin assemblies during alignment, we still have little insight into what is upstream of Rho that guides its polarity. Classic body segmentation determinants do have expression boundaries where aligning interfaces are positioned in the embryo. The anterior interface corresponds to the Patched/Engrailed boundary while the posterior interface marks the beginning of Serrate expression[49]. Given that the gene expression patterns at these two boundaries are quite different from one another, it seems unlikely that they would be able to direct the same downstream effectors to spatially guide alignment. We are also limited in our ability to test their functional significance as inhibition of one of these genes has severe, confounding effects on the embryonic body plan.

The observation that PIP3 is enriched along aligning interfaces may point us toward a candidate worth testing. PIP3 production can be promoted by PI3-Kinase recruitment to the membrane, which is commonly trigged by Receptor Tyrosine Kinase (RTK) activation[143]. Additionally, it has long been known that pTyr staining is enriched along aligning junctions, but the protein that this signal corresponds to is not known[49]. Enrichment of PIP3 and pTyr may be indicative of RTK signaling upregulation at aligning junctions. A screen of RTKs that are known to activate PI3-Kinase could be fruitful in identifying new polarity determinants in alignment.

Another foothold we have is the knowledge that preferential activation of Rho along aligning junctions is key to this morphogenetic process. Identification of the RhoGEF that is upstream of this could be another worthwhile step towards discovering new polarity factors for alignment. Once the RhoGEF that activates Rho in this context is isolated, Co-Immunoprecipitation, Mass Spectrometry and/or yeast two-hybrid could be used to identify its binding partners and, therefore, possible new polarity factors.

Given the unique cell geometry produced and the unique time and place in embryogenesis that this event occurs, the signaling mechanisms that underly alignment are likely to be novel and have a significant impact in the morphogenesis field. However, as I will describe more thoroughly below, there are significant technical obstacles to functionally screening for proteins that have a role in alignment. These will need to be overcome before RTKs and RhoGEFs can be further investigated rigorously.

The challenges of functional screens in the embryo

Alignment occurs during an experimentally challenging time in development. At mid-embryogenesis, zygotic depletion of proteins-of-interest is frequently rescued by maternally-contributed pools of protein. However, simultaneous inhibition of both zygotic and maternal sources of a protein will commonly cause significant defects in the earlier development of the embryo. This typically either causes death prior to reaching Stage 13 or extreme morphological defects that confound alignment measurements. These obstacles are what led me to rely on drug inhibitors and deGradFP, which allowed me to temporally control inhibition of proteins-of-interest. However, the number of targets that can be pharmacologically inhibited are limited, and many drugs are prone to the caveat of off-target effects. Additionally, I found that deGradFP, while able to robustly inhibit Myo-II activity, was not able to consistently degrade other targets efficiently enough to observe a functional consequence. I also found that RNAi was rarely effective at functionally depleting transcripts, even when driven by high-expression GAL4 lines. Again, this may be due to the presence of maternally-contributed protein. Unveiling additional molecular mechanism will require new, robust yet spatiotemporally incisive approaches to protein depletion.

A promising new technology that could address this problem is conditional use of CRISPR-Cas9[144,145]. In brief, Cas9 can be conditionally supplied by GAL4-UAS in

order to achieve spatio-temporal specificity over gene knockout. This has been demonstrated to work using a maternally-supplied GAL4 to deplete maternal deposition of protein in embryos[146]. Therefore, in principle, the expression of Cas9 can be conditionally controlled by GAL4 lines that express in the embryonic epithelium to zygotically create mutations in the developing embryo. Guide RNAs (gRNA) can be supplied conditionally with UAS/GAL4. They can also be expressed ubiquitously by plasmid injection or by crossing to gRNA transgenic lines generated by the *Drosophila* RNAi Screen Center. The efficacy of this approach will depend on a number of factors. First, the timing of expression will need to be optimized so that early developmental events are not affected by CRISPR/Cas9 mutations. However, even after mutations have been made, remaining transcripts and protein can still rescue. Therefore, the Cas9 needs to be expressed early enough so that there is enough developmental time for protein and RNA to be naturally degraded prior to alignment. It may also be necessary to partially deplete maternally-derived protein to reveal phenotypes. However, this technology shows promise for robustly knocking down candidates. Once candidates are identified, more precise manipulations such as optogenetics would allow for more rigorous and incisive tests of their function.

Amplification and robustness of signaling information

As previously discussed, feedback within the Rho pathway may be important for fine-tuning the level of Rho activity (Chapter 5) or balancing its activity with that of Rac and other small GTPases (Chapter 6). However, could there be other reasons for having so many apparent feedback mechanisms within the pathway?

In addition to negative feedback, I reported positive crosstalk between Myo-II and Actin as well as positive regulation of Dia planar polarity by Rho Kinase (Chapter 5). It possible that these interactions make for a robust system that is refractory to challenges.

For example, I did not observe significant disruption of planar polarity of either F-actin or Myo-II even with constitutive activation of the Rho pathway, despite this manipulation having other dramatic effects in the tissue. Additionally, I expressed other constructs that have been reported to alter actomyosin in other tissues. These include constitutively active Myosin Light Chain Kinase and constitutively active Myosin Phosphatase, which should up- and down-regulate Myo-II, respectively. However, neither of these had any effect on alignment (data not shown). Other similar experiments were attempted that did not disrupt the aligned geometry (data not shown). It is hard to conclude the presence of robustness from these data, as there is no positive control to show that the manipulation had any effect. However, they could be consistent with alignment being an extremely robust process, which may be a function of multiple feedback loops that buffer against aberrance in the system.

Additionally, I observed that there is an “amplification” of information from the top to the bottom of the Rho pathway. Rho-GTP accumulations at aligning interfaces are extremely subtle, averaging about 5% elevation relative to orthogonal junctions. ROK and Dia are enriched to a higher degree at about 45% and 9%, respectively. The most downstream effectors of the pathway, Myo-II and F-actin are enriched at 45% and 20%, respectively. This trend should be viewed with the caveat that very different visualization methods were used to quantify these enrichments. However, the data set supports the idea that polarities are more dramatic amongst the downstream effectors, suggesting there are mechanisms that amplify the recruitment of proteins within the lower tiers of the pathway. It is possible that positive feedback plays some role in this.

Finer manipulations of individual feedback loops would be needed to answer these questions, and this necessitates identifying the molecules that facilitate these feedbacks. However, alignment may be a promising system for exploring these

questions that are broadly applicable, as all forms of morphogenesis must have mechanisms to buffer against error.

Appendix

Below are Figure legends for the accompanying movie files.

Movie 1. The effect of LatB treatment on F-actin distribution (Related to Fig. 5.4A)

Time point 0 shows the epithelium before drug treatment. F-actin is visualized with Utr-ABD::GFP. Scale bar = 4 μm. Representative of 4 embryos.

Movie 2. The effect of LatB treatment on Rho activation (Related to Fig. 5.4B)

Time point 0 shows the epithelium before drug treatment. GTP-bound Rho is visualized with the Rho sensor (Ubi-Ani-RGB::GFP). Scale bar = 4 μm. Representative of 4 embryos.

Movie 3. The effect of LatB treatment on ROK distribution (Related to Fig. 5.4E)

Time point 0 shows the epithelium before drug treatment. ROK localization is visualized with GFP::ROK^{K116A}. Scale bar = 4 μm. Representative of 5 embryos.

Movie 4. The effect of LatB treatment on Dia distribution (Related to Fig. 5.4H)

Time point 0 shows the epithelium before drug treatment. ROK localization is visualized with Dia::GFP. Scale bar = 4 μm. Representative of 6 embryos.

Movie 5. The effect of CytoD treatment on F-actin distribution (Related to Fig. 5.5A)

Time point 0 shows the epithelium before drug treatment. F-actin is visualized with Utr-ABD::GFP. Scale bar = 4 μm. Representative of 5 embryos.

Movie 6. F-actin protrusion dynamics at aligning interfaces (Related to Fig. 6.1)

F-actin is visualized with Utr-ABD::GFP. Scale bar = 4 μm. Representative of 4 embryos.

Bibliography

1. Wallingford, J.B., Niswander, L.A., Shaw, G.M., and Finnell, R.H. (2013). The Continuing Challenge of Understanding, Preventing, and Treating Neural Tube Defects. Science *339*, 1222002.

2. Wang, Y. (2009). Wnt/Planar cell polarity signaling: A new paradigm for cancer therapy. Mol. Cancer Ther. *8*, 2103–2109.

3. Larson, D.E., Johnson, R.I., Swat, M., Cordero, J.B., Glazier, J.A., and Cagan, R.L. (2010). Computer Simulation of Cellular Patterning Within the Drosophila Pupal Eye. PLoS Comput Biol *6*, e1000841.

4. Hayashi, T., and Carthew, R.W. (2004). Surface mechanics mediate pattern formation in the developing retina. Nature *431*, 647–652.

5. Lecuit, T., and Lenne, P.-F. (2007). Cell surface mechanics and the control of cell shape, tissue patterns and morphogenesis. Nat. Rev. Mol. Cell Biol. *8*, 633–644.

6. Heisenberg, C.-P., and Bellaïche, Y. (2013). Forces in Tissue Morphogenesis and Patterning. Cell *153*, 948–962.

7. Martin, A.C., Gelbart, M., Fernandez-Gonzalez, R., Kaschube, M., and Wieschaus, E.F. (2010). Integration of contractile forces during tissue invagination. J. Cell Biol. *188*, 735–749.

8. Guillot, C., and Lecuit, T. (2013). Mechanics of Epithelial Tissue Homeostasis and Morphogenesis. Science *340*, 1185–1189.

9. Mao, Y., and Baum, B. (2015). Tug of war—The influence of opposing physical forces on epithelial cell morphology. Dev. Biol. *401*, 92–102.

10. Liu, Z., Tan, J.L., Cohen, D.M., Yang, M.T., Sniadecki, N.J., Ruiz, S.A., Nelson, C.M., and Chen, C.S. (2010). Mechanical tugging force regulates the size of cell-cell junctions. Proc. Natl. Acad. Sci. *107*, 9944–9949.

11. Kale, G.R., Yang, X., Philippe, J.-M., Mani, M., Lenne, P.-F., and Lecuit, T. (2018). Distinct contributions of tensile and shear stress on E-cadherin levels during morphogenesis. Nat. Commun. *9*. Available at: https://proxy.library.upenn.edu:2065/pmc/articles/PMC6258672/ [Accessed January 20, 2019].

12. Levayer, R., and Lecuit, T. (2012). Biomechanical regulation of contractility: spatial control and dynamics. Trends Cell Biol. *22*, 61–81.

13. Martin, A.C. (2010). Pulsation and stabilization: Contractile forces that underlie morphogenesis. Dev. Biol. *341*, 114–125.

14. Svitkina, T.M. (2018). Ultrastructure of the actin cytoskeleton. Curr. Opin. Cell Biol. *54*, 1–8.

15. Roper, K. (2013). Supracellular actomyosin assemblies during development. Bioarchitecture *3*, 45–49.

16. Aliee, M., Röper, J.-C., Landsberg, K.P., Pentzold, C., Widmann, T.J., Jülicher, F., and Dahmann, C. (2012). Physical Mechanisms Shaping the Drosophila Dorsoventral Compartment Boundary. Curr. Biol. *22*, 967–976.

17. Landsberg, K.P., Farhadifar, R., Ranft, J., Umetsu, D., Widmann, T.J., Bittig, T., Said, A., Jülicher, F., and Dahmann, C. (2009). Increased Cell Bond Tension Governs Cell Sorting at the Drosophila Anteroposterior Compartment Boundary. Curr. Biol. *19*, 1950–1955.

18. Rauzi, M., Verant, P., Lecuit, T., and Lenne, P.-F. (2008). Nature and anisotropy of cortical forces orienting Drosophila tissue morphogenesis. Nat. Cell Biol. *10*, 1401–1410.

19. Fernandez-Gonzalez, R., Simoes, S. de M., Röper, J.-C., Eaton, S., and Zallen, J.A. (2009). Myosin II Dynamics Are Regulated by Tension in Intercalating Cells. Dev. Cell *17*, 736–743.

20. Roper, K. (2012). Anisotropy of Crumbs and aPKC Drives Myosin Cable Assembly during Tube Formation. Dev. Cell *23*, 939–953.

21. Fernandez-Gonzalez, R., and Zallen, J.A. (2013). Wounded cells drive rapid epidermal repair in the early Drosophila embryo. Mol. Biol. Cell *24*, 3227–3237.

22. Belacortu, Y., and Paricio, N. (2011). Drosophila as a model of wound healing and tissue regeneration in vertebrates. Dev. Dyn. *240*, 2379–2404.

23. Davidson, L.A., Ezin, A.M., and Keller, R. (2002). Embryonic wound healing by apical contraction and ingression in Xenopus laevis. Cell Motil. *53*, 163–176.

24. al, W.W., et Wound healing recapitulates morphogenesis in Drosophila embryos. - PubMed - NCBI. Available at: https://proxy.library.upenn.edu:2065/pubmed/12402048 [Accessed January 22, 2019].

25. Lienkamp, S.S., Liu, K., Karner, C.M., Carroll, T.J., Ronneberger, O., Wallingford, J.B., and Walz, G. (2012). Vertebrate kidney tubules elongate using a planar cell polarity-dependent, rosette-based mechanism of convergent extension. Nat. Genet. *44*, 1382–1387.

26. Nishimura, T., Honda, H., and Takeichi, M. (2012). Planar Cell Polarity Links Axes of Spatial Dynamics in Neural-Tube Closure. Cell *149*, 1084–1097.

27. Sullivan-Brown, J., and Goldstein, B. (2012). Neural Tube Closure: The Curious Case of Shrinking Junctions. Curr. Biol. *22*, R574–R576.

28. Zallen, J.A., and Wieschaus, E. (2004). Patterned Gene Expression Directs Bipolar Planar Polarity in Drosophila. Dev. Cell *6*, 343–355.

29. Monier, B., Pélissier-Monier, A., and Sanson, B. (2011). Establishment and maintenance of compartmental boundaries: role of contractile actomyosin barriers. Cell. Mol. Life Sci. *68*, 1897–1910.

30. Bertet, C., Rauzi, M., and Lecuit, T. (2009). Repression of Wasp by JAK/STAT signalling inhibits medial actomyosin network assembly and apical cell constriction in intercalating epithelial cells. Development *136*, 4199–4212.

31. Bertet, C., Sulak, L., and Lecuit, T. (2004). Myosin-dependent junction remodelling controls planar cell intercalation and axis elongation. Nature *429*, 667–671.

32. Umetsu, D., Aigouy, B., Aliee, M., Sui, L., Eaton, S., Jülicher, F., and Dahmann, C. (2014). Local Increases in Mechanical Tension Shape Compartment Boundaries by Biasing Cell Intercalations. Curr. Biol. *24*, 1798–1805.

33. Ly, D., Resch, E., Ordiway, G., and DiNardo, S. (2017). Asymmetrically deployed actomyosin-based contractility generates a boundary between developing leg segments in Drosophila. Dev. Biol. *429*, 165–176.

34. Butler, M.T., and Wallingford, J.B. (2017). Planar cell polarity in development and disease. Nat. Rev. Mol. Cell Biol. *18*, 375.

35. Lawson, C.D., and Ridley, A.J. (2018). Rho GTPase signaling complexes in cell migration and invasion. J Cell Biol *217*, 447–457.

36. Parri, M., and Chiarugi, P. (2010). Rac and Rho GTPases in cancer cell motility control. Cell Commun. Signal. CCS *8*, 23.

37. Schwartz, M. (2004). Rho signalling at a glance. J. Cell Sci. *117*, 5457–5458.

38. Sasamura, T., Kobayashi, T., Kojima, S., Qadota, H., Ohya, Y., Masai, I., and Hotta, Y. (1997). Molecular cloning and characterization of Drosophila genes encoding small GTPases of the rab and rho families. Mol. Gen. Genet. MGG *254*, 486–494.

39. Amano, M., Nakayama, M., and Kaibuchi, K. (2010). Rho-kinase/ROCK: A key regulator of the cytoskeleton and cell polarity. Cytoskeleton *67*, 545–554.

40. Amano, M., Ito, M., Kimura, K., Fukata, Y., Chihara, K., Nakano, T., Matsuura, Y., and Kaibuchi, K. (1996). Phosphorylation and Activation of Myosin by Rho-associated Kinase (Rho-kinase). J. Biol. Chem. *271*, 20246–20249.

41. Breitsprecher, D., and Goode, B.L. (2013). Formins at a glance. J Cell Sci *126*, 1–7.

42. Kerridge, S., Munjal, A., Philippe, J.-M., Jha, A., de las Bayonas, A.G., Saurin, A.J., and Lecuit, T. (2016). Modular activation of Rho1 by GPCR signalling imparts polarized myosin II activation during morphogenesis. Nat. Cell Biol. *18*, 261–270.

43. Mason, F.M., Tworoger, M., and Martin, A.C. (2013). Apical domain polarization localizes actin–myosin activity to drive ratchet-like apical constriction. Nat. Cell Biol. *15*, 926–936.

44. Jacinto, A., Woolner, S., and Martin, P. (2002). Dynamic Analysis of Dorsal Closure in Drosophila: From Genetics to Cell Biology. Dev. Cell *3*, 9–19.

45. Munjal, A., Philippe, J.-M., Munro, E., and Lecuit, T. (2015). A self-organized biomechanical network drives shape changes during tissue morphogenesis. Nature *524*, 351–355.

46. Simoes, S. d. M., Mainieri, A., and Zallen, J.A. (2014). Rho GTPase and Shroom direct planar polarized actomyosin contractility during convergent extension. J. Cell Biol. *204*, 575–589.

47. Major, R.J., and Irvine, K.D. (2006). Localization and requirement for Myosin II at the dorsal-ventral compartment boundary of theDrosophila wing. Dev. Dyn. *235*, 3051–3058.

48. Major, R.J., and Irvine, K.D. (2005). Influence of Notch on dorsoventral compartmentalization and actin organization in the Drosophila wing. Development *132*, 3823–3833.

49. Simone, R.P., and DiNardo, S. (2010). Actomyosin contractility and Discs large contribute to junctional conversion in guiding cell alignment within the Drosophila embryonic epithelium. Development *137*, 1385–1394.

50. Price, M.H., Roberts, D.M., McCartney, B.M., Jezuit, E., and Peifer, M. (2006). Cytoskeletal dynamics and cell signaling during planar polarity establishment in the Drosophila embryonic denticle. J. Cell Sci. *119*, 403–415.

51. Marcinkevicius, E., and Zallen, J.A. (2013). Regulation of cytoskeletal organization and junctional remodeling by the atypical cadherin Fat. Development *140*, 433–443.

52. Gibson, M.C., Patel, A.B., Nagpal, R., and Perrimon, N. (2006). The emergence of geometric order in proliferating metazoan epithelia. Nature *442*, 1038–1041.

53. Classen, A.-K., Anderson, K.I., Marois, E., and Eaton, S. (2005). Hexagonal Packing of Drosophila Wing Epithelial Cells by the Planar Cell Polarity Pathway. Dev. Cell *9*, 805–817.

54. Donoughe, S., and DiNardo, S. (2011). dachsous and frizzled contribute separately to planar polarity in the Drosophila ventral epidermis. Dev. Camb. Engl. *138*, 2751–2759.

55. Farhadifar, R., Röper, J.-C., Aigouy, B., Eaton, S., and Jülicher, F. (2007). The Influence of Cell Mechanics, Cell-Cell Interactions, and Proliferation on Epithelial Packing. Curr. Biol. *17*, 2095–2104.

56. Goley, E.D., and Welch, M.D. (2006). The ARP2/3 complex: an actin nucleator comes of age. Nat. Rev. Mol. Cell Biol. *7*, 713–726.

57. Rotty, J.D., Wu, C., and Bear, J.E. (2013). New insights into the regulation and cellular functions of the ARP2/3 complex. Nat. Rev. Mol. Cell Biol. *14*, 7–12.

58. Mullins, R.D., Bieling, P., and Fletcher, D.A. (2018). From solution to surface to filament: actin flux into branched networks. Biophys. Rev. *10*, 1537.

59. Efimova, N., and Svitkina, T.M. (2018). Branched actin networks push against each other at adherens junctions to maintain cell-cell adhesion. J. Cell Biol. *217*, 1827–1845.

60. Del Signore, S.J., Cilla, R., and Hatini, V. (2018). The WAVE Regulatory Complex and Branched F-Actin Counterbalance Contractile Force to Control Cell Shape and Packing in the Drosophila Eye. Dev. Cell *44*, 471-483.e4.

61. Müller, H.A., and Wieschaus, E. (1996). armadillo, bazooka, and stardust are critical for early stages in formation of the zonula adherens and maintenance of the polarized blastoderm epithelium in Drosophila. J. Cell Biol. *134*, 149–163.

62. Theurkauf, W.E. (1992). Behavior of structurally divergent α-tubulin isotypes during Drosophila embryogenesis: Evidence for post-translational regulation of isotype abundance. Dev. Biol. *154*, 205–217.

63. Mitchison, T.J., and Sedat, J. (1983). Localization of antigenic determinants in whole Drosophila embryos. Dev. Biol. *99*, 261–264.

64. Goddette, D.W., and Frieden, C. (1986). Actin polymerization. The mechanism of action of cytochalasin D. J. Biol. Chem. *261*, 15974–15980.

65. Brenner, S.L., and Korn, E.D. (1979). Substoichiometric concentrations of cytochalasin D inhibit actin polymerization. Additional evidence for an F-actin treadmill. J. Biol. Chem. *254*, 9982–9985.

66. Casella, J.F., Flanagan, M.D., and Lin, S. (1981). Cytochalasin D inhibits actin polymerization and induces depolymerization of actin filaments formed during platelet shape change. Nature *293*, 302–305.

67. Morris, A., and Tannenbaum, J. (1980). Cytochalasin D does not produce net depolymerization of actin filaments in HEp-2 cells. Nature *287*, 637–639.

68. Yarmola, E.G., Somasundaram, T., Boring, T.A., Spector, I., and Bubb, M.R. (2000). Actin-Latrunculin A Structure and Function DIFFERENTIAL MODULATION OF ACTIN-BINDING PROTEIN FUNCTION BY LATRUNCULIN A. J. Biol. Chem. *275*, 28120–28127.

69. Caussinus, E., Kanca, O., and Affolter, M. (2012). Fluorescent fusion protein knockout mediated by anti-GFP nanobody. Nat. Struct. Mol. Biol. *19*, 117–121.

70. Simões, S. de M., Blankenship, J.T., Weitz, O., Farrell, D.L., Tamada, M., Fernandez-Gonzalez, R., and Zallen, J.A. (2010). Rho-Kinase Directs Bazooka/Par-3 Planar Polarity during Drosophila Axis Elongation. Dev. Cell *19*, 377–388.

71. Homem, C.C.F., and Peifer, M. (2008). Diaphanous regulates myosin and adherens junctions to control cell contractility and protrusive behavior during morphogenesis. Development *135*, 1005–1018.

72. Afshar, K., Stuart, B., and Wasserman, S.A. (2000). Functional analysis of the Drosophila diaphanous FH protein in early embryonic development. Development *127*, 1887–1897.

73. Bardet, P.-L., Guirao, B., Paoletti, C., Serman, F., Léopold, V., Bosveld, F., Goya, Y., Mirouse, V., Graner, F., and Bellaïche, Y. (2013). PTEN Controls Junction Lengthening and Stability during Cell Rearrangement in Epithelial Tissue. Dev. Cell *25*, 534–546.

74. Royou, A., Field, C., Sisson, J.C., Sullivan, W., and Karess, R. Reassessing the Role and Dynamics of Nonmuscle Myosin II during Furrow Formation in Early Drosophila Embryos. Available at: http://www.molbiolcell.org [Accessed November 16, 2017].

75. Huang, J., Zhou, W., Dong, W., Watson, A.M., and Hong, Y. (2009). Directed, efficient, and versatile modifications of the Drosophila genome by genomic engineering. Proc. Natl. Acad. Sci. *106*, 8284–8289.

76. Castrillon, D.H., and Wasserman, S.A. (1994). Diaphanous is required for cytokinesis in Drosophila and shares domains of similarity with the products of the limb deformity gene. Development *120*, 3367–3377.

77. Oda, H., and Tsukita, S. (2001). Real-time imaging of cell-cell adherens junctions reveals that Drosophila mesoderm invagination begins with two phases of apical constriction of cells. J. Cell Sci. *114*, 493–501.

78. Martin, A.C., Kaschube, M., and Wieschaus, E.F. (2009). Pulsed contractions of an actin–myosin network drive apical constriction. Nature *457*, 495–499.

79. Kasza, K.E., Farrell, D.L., and Zallen, J.A. (2014). Spatiotemporal control of epithelial remodeling by regulated myosin phosphorylation. Proc. Natl. Acad. Sci. U. S. A. *111*, 11732–11737.

80. Adams, R.R., Tavares, A.A.M., Salzberg, A., Bellen, H.J., and Glover, D.M. (1998). pavarotti encodes a kinesin-like protein required to organize the central spindle and contractile ring for cytokinesis. Genes Dev. *12*, 1483–1494.

81. Duda, M., Khalilgharibi, N., Carpi, N., Bove, A., Piel, M., Charras, G., Baum, B., and Mao, Y. (2017). Polarization of Myosin II refines tissue material properties to buffer mechanical stress. bioRxiv, 241497.

82. Schulte, J., Charish, K., Que, J., Ravn, S., MacKinnon, C., and Auld, V.J. (2006). Gliotactin and Discs large form a protein complex at the tricellular junction of polarized epithelial cells in Drosophila. J. Cell Sci. *119*, 4391–4401.

83. Schulte, J., Tepass, U., and Auld, V.J. (2003). Gliotactin, a novel marker of tricellular junctions, is necessary for septate junction development in Drosophila. J. Cell Biol. *161*, 991–1000.

84. Carvalho, L., Patricio, P., Ponte, S., Heisenberg, C.-P., Almeida, L., Nunes, A.S., Araújo, N.A.M., and Jacinto, A. (2018). Occluding junctions as novel regulators of tissue mechanics during wound repair. J Cell Biol *217*, 4267–4283.

85. Rizvi, S.A., Neidt, E.M., Cui, J., Feiger, Z., Skau, C.T., Gardel, M.L., Kozmin, S.A., and Kovar, D.R. (2009). Identification and characterization of a small molecule inhibitor of formin-mediated actin assembly. Chem. Biol. *16*, 1158–1168.

86. Hara, Y., Shagirov, M., and Toyama, Y. (2016). Cell Boundary Elongation by Non-autonomous Contractility in Cell Oscillation. Curr. Biol. *26*, 2388–2396.

87. Tornavaca, O., Chia, M., Dufton, N., Almagro, L.O., Conway, D.E., Randi, A.M., Schwartz, M.A., Matter, K., and Balda, M.S. (2015). ZO-1 controls endothelial adherens junctions, cell–cell tension, angiogenesis, and barrier formation. J. Cell Biol. *208*, 821–838.

88. Heissler, S.M., and Sellers, J.R. (2015). Four Things to Know about Myosin Light Chains as Reporters for Nonmuscle Myosin-2 Dynamics in Live Cells. Cytoskelet. Hoboken NJ *72*, 65–70.

89. Vasquez, C.G., Heissler, S.M., Billington, N., Sellers, J.R., and Martin, A.C. (2016). Drosophila non-muscle myosin II motor activity determines the rate of tissue folding. eLife *5*, e20828.

90. Campanale, J.P., Sun, T.Y., and Montell, D.J. (2017). Development and dynamics of cell polarity at a glance. J Cell Sci *130*, 1201–1207.

91. Chen, J., and Zhang, M. (2013). The Par3/Par6/aPKC complex and epithelial cell polarity. Exp. Cell Res. *319*, 1357–1364.

92. Krahn, M.P., Klopfenstein, D.R., Fischer, N., and Wodarz, A. (2010). Membrane Targeting of Bazooka/PAR-3 Is Mediated by Direct Binding to Phosphoinositide Lipids. Curr. Biol. *20*, 636–642.

93. Laevsky, G., and Knecht, D.A. (2003). Cross-linking of actin filaments by myosin II is a major contributor to cortical integrity and cell motility in restrictive environments. J. Cell Sci. *116*, 3761–3770.

94. Lawler, S. (1999). Regulation of actin dynamics: The LIM kinase connection. Curr. Biol. *9*, R800–R802.

95. Fehon, R.G., McClatchey, A.I., and Bretscher, A. (2010). Organizing the cell cortex: the role of ERM proteins. Nat. Rev. Mol. Cell Biol. *11*, 276–287.

96. McClatchey, A.I. (2014). ERM proteins at a glance. J Cell Sci *127*, 3199–3204.

97. Speck, O., Hughes, S.C., Noren, N.K., Kulikauskas, R.M., and Fehon, R.G. (2003). Moesin functions antagonistically to the Rho pathway to maintain epithelial integrity. Nature *421*, 83–87.

98. Monier, B., Pélissier-Monier, A., Brand, A.H., and Sanson, B. (2010). An actomyosin-based barrier inhibits cell mixing at compartmental boundaries in Drosophila embryos. Nat. Cell Biol. *12*, 60–65.

99. Urbano, J.M., Naylor, H.W., Scarpa, E., Muresan, L., and Sanson, B. (2018). Suppression of epithelial folding at actomyosin-enriched compartment boundaries downstream of Wingless signalling in Drosophila. Development *145*, dev155325.

100. Bement, W.M., Leda, M., Moe, A.M., Kita, A.M., Larson, M.E., Golding, A.E., Pfeuti, C., Su, K.-C., Miller, A.L., Goryachev, A.B., *et al.* (2015). Activator-inhibitor coupling between Rho signalling and actin assembly makes the cell cortex an excitable medium. Nat. Cell Biol. *17*, 1471–1483.

101. Segal, D., Zaritsky, A., Schejter, E.D., and Shilo, B.-Z. (2018). Feedback inhibition of actin on Rho mediates content release from large secretory vesicles. J. Cell Biol.

102. Graessl, M., Koch, J., Calderon, A., Kamps, D., Banerjee, S., Mazel, T., Schulze, N., Jungkurth, J.K., Patwardhan, R., Solouk, D., *et al.* (2017). An excitable Rho GTPase signaling network generates dynamic subcellular contraction patterns. J Cell Biol *216*, 4271–4285.

103. Priya, R., Gomez, G.A., Budnar, S., Verma, S., Cox, H.L., Hamilton, N.A., and Yap, A.S. (2015). Feedback regulation through myosin II confers robustness on RhoA signalling at E-cadherin junctions. Nat. Cell Biol. *17*, 1282–1293.

104. Priya, R., Liang, X., Teo, J.L., Duszyc, K., Yap, A.S., and Gomez, G.A. (2017). ROCK1 but not ROCK2 contributes to RhoA signaling and NMIIA-mediated contractility at the epithelial zonula adherens. Mol. Biol. Cell *28*, 12–20.

105. Amano, M., Nakayama, M., and Kaibuchi, K. (2010). Rho-kinase/ROCK: A key regulator of the cytoskeleton and cell polarity. Cytoskeleton *67*, 545–554.

106. Mulinari, S., Barmchi, M.P., and Hacker, U. (2008). DRhoGEF2 and Diaphanous Regulate Contractile Force during Segmental Groove Morphogenesis in the Drosophila Embryo. Mol. Biol. Cell *19*, 1883–1892.

107. West, J.J., Zulueta-Coarasa, T., Maier, J.A., Lee, D.M., Bruce, A.E.E., Fernandez-Gonzalez, R., and Harris, T.J.C. (2017). An Actomyosin-Arf-GEF Negative Feedback Loop for Tissue Elongation under Stress. Curr. Biol. CB *27*, 2260-2270.e5.

108. Robin, F.B., Michaux, J.B., McFadden, W.M., and Munro, E.M. (2016). Excitable RhoA dynamics drive pulsed contractions in the early C. elegans embryo.

109. Winkelman, J.D., Suarez, C., Hocky, G.M., Harker, A.J., Morganthaler, A.N., Christensen, J.R., Voth, G.A., Bartles, J.R., and Kovar, D.R. (2016). Fascin- and α-Actinin-Bundled Networks Contain Intrinsic Structural Features that Drive Protein Sorting. Curr. Biol. CB *26*, 2697–2706.

110. Hipfner, D.R., Keller, N., and Cohen, S.M. (2004). Slik Sterile-20 kinase regulates Moesin activity to promote epithelial integrity during tissue growth. Genes Dev. *18*, 2243–2248.

111. Neisch, A.L., Formstecher, E., and Fehon, R.G. (2013). Conundrum, an ARHGAP18 orthologue, regulates RhoA and proliferation through interactions with Moesin. Mol. Biol. Cell *24*, 1420–1433.

112. Guilluy, C., Garcia-Mata, R., and Burridge, K. (2011). Rho protein crosstalk: another social network? Trends Cell Biol. *21*, 718–726.

113. Staus, D.P., Taylor, J.M., and Mack, C.P. (2011). Enhancement of mDia2 activity by Rho-kinase-dependent phosphorylation of the diaphanous autoregulatory domain. Biochem. J. *439*, 57–65.

114. Priya, R., Gomez, G.A., Budnar, S., Acharya, B.R., Czirok, A., Yap, A.S., and Neufeld, Z. (2017). Bistable front dynamics in a contractile medium: Travelling wave fronts and cortical advection define stable zones of RhoA signaling at epithelial adherens junctions. PLOS Comput. Biol. *13*, e1005411.

115. Toret, C.P., Shivakumar, P.C., Lenne, P.-F., and Bivic, A.L. (2018). The ELMO-MBC complex and RhoGAP19D couple Rho family GTPases during mesenchymal-to-epithelial-like transitions. Development *145*, dev157495.

116. Svitkina, T. (2013). Ultrastructure of protrusive actin filament arrays. Curr. Opin. Cell Biol. *25*, 574–581.

117. Homem, C.C.F., and Peifer, M. (2009). Exploring the Roles of Diaphanous and Enabled Activity in Shaping the Balance between Filopodia and Lamellipodia. Mol. Biol. Cell *20*, 5138–5155.

118. Balakrishnan, S.S., Basu, U., and Raghu, P. (2015). Phosphoinositide signalling in Drosophila. Biochim. Biophys. Acta BBA - Mol. Cell Biol. Lipids *1851*, 770–784.

119. Janetopoulos, C., and Devreotes, P. (2006). Phosphoinositide signaling plays a key role in cytokinesis. J. Cell Biol. *174*, 485–490.

120. Britton, J.S., Lockwood, W.K., Li, L., Cohen, S.M., and Edgar, B.A. (2002). Drosophila's Insulin/PI3-Kinase Pathway Coordinates Cellular Metabolism with Nutritional Conditions. Dev. Cell *2*, 239–249.

121. Skau, C.T., Courson, D.S., Bestul, A.J., Winkelman, J.D., Rock, R.S., Sirotkin, V., and Kovar, D.R. (2011). Actin Filament Bundling by Fimbrin Is Important for Endocytosis, Cytokinesis, and Polarization in Fission Yeast. J. Biol. Chem. *286*, 26964–26977.

122. Bravo-Cordero, J.J., Magalhaes, M.A.O., Eddy, R.J., Hodgson, L., and Condeelis, J. (2013). Functions of cofilin in cell locomotion and invasion. Nat. Rev. Mol. Cell Biol. *14*. Available at: https://proxy.library.upenn.edu:2065/pmc/articles/PMC3878614/ [Accessed January 17, 2019].

123. Franke, J.D., Montague, R.A., and Kiehart, D.P. (2005). Nonmuscle Myosin II Generates Forces that Transmit Tension and Drive Contraction in Multiple Tissues during Dorsal Closure. Curr. Biol. *15*, 2208–2221.

124. Kim, J.H., Jin, P., Duan, R., and Chen, E.H. (2015). Mechanisms of myoblast fusion during muscle development. Curr. Opin. Genet. Dev. *32*, 162–170.

125. Haralalka, S., Shelton, C., Cartwright, H.N., Katzfey, E., Janzen, E., and Abmayr, S.M. (2011). Asymmetric Mbc, active Rac1 and F-actin foci in the fusion-competent myoblasts during myoblast fusion in Drosophila. Dev. Camb. Engl. *138*, 1551–1562.

126. Biersmith, B., Liu, Z., Bauman, K., and Geisbrecht, E.R. (2011). The DOCK Protein Sponge Binds to ELMO and Functions in Drosophila Embryonic CNS Development. PLOS ONE *6*, e16120.

127. Ishimaru, S., Ueda, R., Hinohara, Y., Ohtani, M., and Hanafusa, H. (2004). PVR plays a critical role via JNK activation in thorax closure during Drosophila metamorphosis. EMBO J. *23*, 3984–3994.

128. Schmidt, A., Lv, Z., and Großhans, J. (2018). ELMO and Sponge specify subapical restriction of Canoe and formation of the subapical domain in early Drosophila embryos. Development *145*, dev157909.

129. Mechanisms for spatiotemporal regulation of Rho-GTPase signaling at synapses (2015). Neurosci. Lett. *601*, 4–10.

130. Holmes William R., Golding Adriana E., Bement William M., and Edelstein-Keshet Leah (2016). A mathematical model of GTPase pattern formation during single-cell wound repair. Interface Focus *6*, 20160032.

131. Tsuji, T., Ishizaki, T., Okamoto, M., Higashida, C., Kimura, K., Furuyashiki, T., Arakawa, Y., Birge, R.B., Nakamoto, T., Hirai, H., *et al.* (2002). ROCK and mDia1 antagonize in Rho-dependent Rac activation in Swiss 3T3 fibroblasts. J. Cell Biol. *157*, 819–830.

132. Izquierdo, E., Quinkler, T., and Renzis, S.D. (2018). Guided morphogenesis through optogenetic activation of Rho signalling during early Drosophila embryogenesis. Nat. Commun. *9*. Available at: https://proxy.library.upenn.edu:2065/pmc/articles/PMC6006163/ [Accessed January 20, 2019].

133. Krueger, D., Tardivo, P., Nguyen, C., and Renzis, S.D. (2018). Downregulation of basal myosin-II is required for cell shape changes and tissue invagination. EMBO J. *37*, e100170.

134. Guglielmi, G., Barry, J.D., Huber, W., and De Renzis, S. (2015). An Optogenetic Method to Modulate Cell Contractility during Tissue Morphogenesis. Dev. Cell *35*, 646.

135. Optogenetic inhibition of apical constriction during Drosophila embryonic development (2017). Methods Cell Biol. *139*, 167–186.

136. Grashoff, C., Hoffman, B.D., Brenner, M.D., Zhou, R., Parsons, M., Yang, M.T., McLean, M.A., Sligar, S.G., Chen, C.S., Ha, T., *et al.* (2010). Measuring mechanical tension across vinculin reveals regulation of focal adhesion dynamics. Nature *466*, 263–266.

137. Cai, D., Chen, S.-C., Prasad, M., He, L., Wang, X., Choesmel-Cadamuro, V., Sawyer, J.K., Danuser, G., and Montell, D.J. (2014). Mechanical Feedback through E-Cadherin Promotes Direction Sensing during Collective Cell Migration. Cell *157*, 1146–1159.

138. Borghi, N., Sorokina, M., Shcherbakova, O.G., Weis, W.I., Pruitt, B.L., Nelson, W.J., and Dunn, A.R. (2012). E-cadherin is under constitutive actomyosin-generated tension that is increased at cell-cell contacts upon externally applied stretch. Proc. Natl. Acad. Sci. *109*, 12568–12573.

139. Eder, D., Basler, K., and Aegerter, C.M. (2017). Challenging FRET-based E-Cadherin force measurements in Drosophila. Sci. Rep. *7*, 13692.

140. Yonemura, S., Wada, Y., Watanabe, T., Nagafuchi, A., and Shibata, M. (2010). α-Catenin as a tension transducer that induces adherens junction development. Nat. Cell Biol. *12*, 533–542.

141. Alatortsev, V.E., Kramerova, I.A., Frolov, M.V., Lavrov, S.A., and Westphal, E.D. (1997). Vinculin gene is non-essential in Drosophila melanogaster. FEBS Lett. *413*, 197–201.

142. Brodland, G.W., Veldhuis, J.H., Kim, S., Perrone, M., Mashburn, D., and Hutson, M.S. (2014). CellFIT: A Cellular Force-Inference Toolkit Using Curvilinear Cell Boundaries. PLOS ONE *9*, e99116.

143. Lemmon, M.A., and Schlessinger, J. (2010). Cell signaling by receptor-tyrosine kinases. Cell *141*, 1117–1134.

144. Bier, E., Harrison, M.M., O'Connor-Giles, K.M., and Wildonger, J. (2018). Advances in Engineering the Fly Genome with the CRISPR-Cas System. Genetics *208*, 1–18.

145. Huynh, N., Zeng, J., Liu, W., and King-Jones, K. (2018). A Drosophila CRISPR/Cas9 Toolkit for Conditionally Manipulating Gene Expression in the Prothoracic Gland as a Test Case for Polytene Tissues. G3 GenesGenomesGenetics *8*, 3593–3605.

146. Port, F., Chen, H.-M., Lee, T., and Bullock, S.L. (2014). Optimized CRISPR/Cas tools for efficient germline and somatic genome engineering in Drosophila. Proc. Natl. Acad. Sci. *111*, E2967–E2976.